UNIVERSITÀ DEGLI STUDI
DI MODENA E REGGIO EMILIA

Dottorato di ricerca in ingegneria industriale e del territorio

Ciclo XXXII

CEREAL BY-PRODUCTS: A RENEWABLE AND SUSTAINABLE RESOURCE FOR BIO-BASED BUILDING MATERIALS

SCARTI CEREALICOLI: UNA RISORSA SOSTENIBILE E RINNOVABILE PER IL SETTORE EDILIZIO

Candidato **Virginia Barbieri**

Relatore (Tutor): **Prof. Tiziano Manfredini**

Eventuale Correlatore (Co-Tutor): **Prof.ssa Cristina Siligardi**

Coordinatore del Corso di Dottorato: Prof. Alberto Muscio

Extended abstract (English version)

Wheat is the most common type of cereal used worldwide and the production of wheat husk waste from the refinement process is estimated to ca. 10 million tons in 2020 only in the EU. Since now, no well-defined recycling strategy exists and natural decomposition with the consequent production of polluting greenhouse gases is often the final destination of these residues. Recycling of agricultural by-products, in particular in the building sector, has recently been in focus through many EU-funded project. Interest has been paid to a wide range of agricultural by-products which could potentially be used as locally available and renewable filler/aggregate source in composites. However, wheat husk has not yet been investigated.

Studies performed on several vegetable by-products (such as hemp hurd, sunflower pith, rice husk, corn cob, flax shiv etc.) outline that the high porosity, low thermal conductivity and high moisture buffer value which characterize these resources, make them particularly suitable for building insulation layers. Additionally, the development of these green materials, often named "*bio-based insulations*" or "*bio-insulations*", could perfectly match with necessity of recycling options for the rising amount of agricultural residue and the crucial need of lower carbon footprint and affordable materials for the building sector. Although current thermal insulation products have excellent performances, they are generally based on petroleum derived raw materials (e.g. extruded polystyrene, expanded polystyrene, polyurethane foam, etc.).

Agro-concretes fall in the category of bio-based insulation materials, as they are defined as: *"a mix between aggregates from lignocellular plant matter coming directly or indirectly from agriculture or forestry, which form the bulk of the volume, and a mineral binder".* Among these, the most common one available on the market is lime hemp concrete. This material contains hemp hurds as filler and hydrated and/or hydraulic lime as binder. The material has good thermal insulation properties (0.05-0.12 W/(m·K)) and excellent moisture buffering and acoustic performances. Moreover, it results in a carbon neutral oven negative material, as 1 kg of hemp hurds sequester about 1.6 to 1.8 kg of carbon dioxide and lime binder captures CO_2 during hardening through carbonation.

However, as the agro-concrete is only slightly compacted during placing, the

compressive strength of the hardened material does not exceed 0.5 MPa after 60 days. It seems clear that the mechanical properties of these agro concretes may be considered as the main weakness point. Indeed, hemp based concretes cannot be used as load-bearing materials. Additionally, the amount of hemp hurd annually available (currently 43000 t/yr in Europe) is limited compared to others agricultural by-products (e.g. cereal residues) which could be potentially used to design agro-concrete.

The present work was aimed to the design of wheat husk agro-concrete as potential alternative to hemp lime one. The fundamental idea was to develop new materials with the same environmental advantages and performances of lime hemp concrete but with higher availability and lower cost. Throughout this thesis work, hemp hurd was thus taken as a bench mark in terms of technological performances of the developed materials.

The first part of the study was focused on full characterization of wheat husk and hemp hurd agro-resources' by-products according to *RILEM Technical Committee 236-BBM 'Bio-aggregate based building Materials'*.

Shape and particle size distribution of the two type of aggregate are influenced by their origin. Indeed, it is known that the size of wheat husk is strongly dependent on wheat grains size. In contrast, hemp hurd come from an industrial grinding process of hemp stems which generate a more dispersed particle size distribution. Analyses highlight a lower elongation factor, defined as the length to width ratio (L/W), for hemp aggregates. Considering that the concrete placing includes uniaxial compaction, this parameter has a significant effect on how the aggregates orient themselves and pack under applied pressure. Moreover, the absolute density of wheat husk (1507 kg/m^3) was found to be slightly higher than that of hemp hurd (1450 kg/m^3) as a consequence of the different chemical composition of the two type of aggregate. Indeed, wheat husk contains less lignin (10.9 %) than hemp hurd (21 %) as well as a higher amount of ash (1.1 % in wheat husk vs 0.6 % in hemp hurd). One of the most important difference between the two vegetal particles are observed in the porosity network. In fact, wheat husk particle is characterized by a lower level of intra-particle porosity (78 % compared to 85 % of hemp hurd) with little vessels whose diameter (less than 30 μm) are smaller than vascular bundle structures observed in hemp particles. Nevertheless, wheat husk and hemp hurd have similar

thermal conductivity and hygric capacity and can both be classified as having excellent hygrothermal properties (dry thermal conductivity of 0.05 W/(m·K) and MBV equal to 2.06 g/(m^2·%RH)). This result is highly significant and supports the possibility of substituting hemp hurd for wheat husk in agro-concrete. Indeed, this biomass residue is not only a good thermal insular but also an excellent hygric regulator.

Subsequently, wheat husk aggregates were mixed with lime-based binder and thermal and mechanical properties of this concrete were compared with those of hemp concrete manufactured with the same process. The desired outcome of these experiments was to verify the possibility of directly substituting hemp hurd with wheat husk without modifying existing forming methods. The approach of this work is thus quite original, combining well-established technologies and know-how in bio based building materials for the development of new materials.

Despite the higher dry apparent density of wheat husk lime concrete, the total porosity (around 80 %) and dry thermal conductivity (ca. 0.09 W/(m·K)) were similar for both types of concrete. The somewhat lower mechanical performance of lime wheat concrete (~0.20 MPa) with respect to lime hemp concrete, although in line with those expected for infilling walls without load bearing requirements, was found to be due to lower adherence of wheat husk to the lime-based binder.

In order to obtain agro-concrete with improved mechanical performance, subsequent work was dedicated to investigate an alternative binder with better compatibility with the novel vegetal filler.

Magnesia based-binders not only have a potentially lower environmental impact and production costs compared to lime-based ones, but some authors also report greater compatibility with organic fillers in consequence to the lower alkalinity of MgO-cements (observed especially for magnesium oxysulfate (MOS), magnesium phosphate and magnesium oxychloride cement) which inhibit degradation of the vegetal particles inside the MgO-agro concrete.

In particular, the work was concentrated on magnesium oxysulfate (MOS) cement composed of reactive MgO and $MgSO_4$ aqueous solution with the addition of a vegetal protein-rich flour recently used by Sassoni *et al.* for the production of hemp-based composites [1,2]. Considering the promising technological properties obtained

for this bio based panel, the novel binder was further investigated in this thesis work. As no microstructural or compositional data was reported by Sassoni *et al.* [1,2], the first part was dedicated to this issue. In particular, in order to deduce important knowledge for designing lightweight concrete composition and choosing suitable processing routes for the manufacturing of insulation concrete, the effect of a vegetal flour (composed of proteins, carbohydrates and lipids) and $MgSO_4$ on the hydration kinetics of MgO was investigated together with the microstructural properties following completed reactions. The crystallization of $5Mg(OH)_2 \cdot MgSO_4 \cdot 7H_2O$, a desired needle-shaped cementitious phase, was favored at 20 °C by the presence of vegetal flour due to modifications of the MgO hydration kinetics. Higher temperatures (35 °C) invariably led to a product composed mainly of $Mg(OH)_2$ with sulfate ions not bond in crystalline lattices. The vegetal flour also resulted in a porous matrix through a templating effect, which should favor gas permeability and thus homogeneous post-setting carbonation of $Mg(OH)_2$ invariably present in the cement.

Based on the information acquired, new biocomposites were prepared using this binder and the two type of lightweight aggregates (wheat husk and hemp hurd). In contrast to the biocomposite processing route used by Sassoni *et al.* [1,2], cold forming was preferred in this work in order to promote the crystallization of desired MOS phases and avoid non-reacted $MgSO_4$. Both mechanical and thermal performances of the bio based composites were evaluated and compared to the corresponding lime-based materials previously investigated.

The dry thermal conductivity measured for MOS based concretes were somewhat higher than the values recorded for lime-based ones and a difference between the use of the two types of aggregates was noted (0.119 W/(m·K) for hemp hurd and 0.168 W/(m·K) for wheat husk). Compared to lime based concretes, higher compressive strengths were obtained for MOS-based ones. This observation was particularly evident when wheat husks were used. In fact, a compressive strength of 2.35 MPa was already observed at 30 days of curing. These results were explained by better compatibility between wheat husk aggregates and MOS-based cement, leading to improved particle-binder adhesion. In particular, crystallization of cementitious phases was observed not only in the cement matrix but also inside wheat husk aggregates. Hence, a dense connected network was created between aggregates and the surrounding binder which reinforced the skeletal structure for the highly porous

aggregate which represent the weakest link in concrete system, in term of mechanical performances.

As a consequence of the much higher mechanical strength of MOS-based concretes with wheat husk (2.35 MPa at 30 days), according to functional classification of lightweight concretes made by the RILEM Committee, it is suitable for the production of structural-insulating blocks (compressive strength >2 MPa, density <1400 kg/m^3, dry thermal conductivity <0.3 W/(m·K). Additionally, it should be noted that the compressive strength of both types of MOS based concrete is highly above the minimum threshold value for wall mixtures (i.e. 0.2 MPa) given by the French professional rules dictated for lime hemp concrete. However, only the lime-based concretes had a low enough dry thermal conductivity (<0.1 W/(m·K)). Nevertheless, the high mechanical strength of the magnesia-based ones provides a margin to further improve the thermal performance and eventually reach the requirements of the French Professional rules.

In summary, considering the results obtained during the course of this work, it can be concluded that wheat husk has a high potential for use in bio based insulating materials possibly also for structural purposes. MOS -based binder was shown to be particularly interesting due to good binder-aggregate compatibility. The results are of high importance from an environmental point of view, not only because a recycling solution is proposed for wheat husk but also because a valid alternative to lime hemp concrete is given. In fact, the high availability of wheat husk should facilitate future developments of bio based alternatives to traditional insulation materials.

Extended abstract (Italian version)

Il grano (o frumento) è il più comune cereale impiegato in tutto il mondo. In Unione Europea, la quantità di scarto (lolla o pula) ottenuto dalla sua lavorazione è stimata a circa 10 milioni di tonnellate nel 2020. Attualmente, non esiste una precisa strategia che preveda il recupero di questo sottoprodotto, il cui smaltimento, spesso incontrollato, provoca forti problemi ambientali. Recentemente, numerosi progetti finanziati dalla UE hanno evidenziato le potenzialità di impiego di scarti agricoli nel settore edilizio come filler/aggregati leggeri in compositi. Tuttavia, in tale contesto, la lolla di grano non è stata ancora presa in considerazione.

Studi condotti su diversi sottoprodotti/scarti vegetali (come canapulo, stelo di girasole, lolla di riso, tutolo di mais, residuo legnoso della pianta di lino, ecc.) hanno mostrato come alcune proprietà che caratterizzano queste risorse (quali elevata porosità, bassa conducibilità termica ed eccellente capacità di smorzare le variazioni di umidità ambiente (*Moisture Buffer Value* elevato)) li rendano particolarmente idonei per la produzione di materiali isolanti per l'involucro edilizio. Inoltre, lo sviluppo di materiali contenti questi scarti, spesso denominati in letteratura "*bio-based insulations*" o "*bio-insulations*", rappresenta un'importante opportunità per conciliare l'urgenza di valorizzare esose quantità di sottoprodotti agricoli ogni anno prodotti con la necessità di ridurre le emissioni di gas serra e gli elevati consumi di risorse non rinnovabili del settore edilizio. Infatti, sebbene i prodotti isolanti attualmente in commercio e tradizionalmente utilizzati abbiano prestazioni termiche eccellenti (ad es. Polistirene estruso, polistirene espanso, schiuma di poliuretano, ecc.), essi sono derivati dal petrolio.

Appartengono alla categoria dei *bio-based insulations* gli *agro-concrete* (calcestruzzi leggeri) definiti come *"miscela di legante inorganico (aereo o idraulico) e aggregati di origine vegetale proveniente direttamente o indirettamente dall'agricoltura o dalla silvicoltura"*. Tra questi il più comune, disponibile sul mercato e oggetto di numerose ricerche, è il composito (o calcestruzzo) canapulo-calce. Esso è ottenuto dalla combinazione della parte legnosa dello stelo di canapa, conosciuta anche come canapulo, ed un legante a base di calce idrauilca e/o aerea. Tale materiale possiede buone proprietà di isolamento termico (conducibilità termica: 0.05-0.12 W/(m·K)), eccellenti prestazioni acustiche e capacità di smorzare le variazioni di umidità

ambiente (*Moisture Buffer Value* > 2 g/(m^2·%RH). Inoltre, tale materiale è definito "*carbon neutral*" o "*carbon negative*", in quanto la valutazione delle emissioni di CO_2 durante il suo periodo di vita (dalla culla alla tomba) si traduce in un valore negativo o pari a zero. Ciò è da ricondurre al processo di carbonatazione della calce che sequestra CO_2 dall'atmosfera e al periodo di crescita della pianta di canapa (fotosintesi clorofilliana), infatti 1 kg di canapulo sottrae circa 1.6-1.8 kg di anidride carbonica all'atmosfera.
Tuttavia, considerando le attuali tecniche di posa in opera del calcestruzzo canapulo-calce, la resistenza a compressione del materiale indurito non supera 0.5 MPa a 60 giorni di maturazione. Si tratta dunque di un materiale poco performante sotto il profilo delle proprietà meccaniche che non può essere utilizzato per la realizzazione di elementi strutturali portanti. Inoltre, la quantità di canapulo disponibile annualmente (attualmente 43000 t/anno in Europa) è limitata rispetto ad altri sottoprodotti agricoli (ad esempio scarti cereali) che potrebbero essere potenzialmente utilizzati per realizzare *agro-concrete*.

Il presente lavoro è finalizzato allo sviluppo di calcestruzzi leggeri contenti lolla di grano come aggregato vegetale in alternativa al canapulo. Tenendo a riferimento il composito canapulo-calce per prestazioni termo-igrometriche e ambientali, si è valutata la possibilità di progettare un nuovo calcestruzzo con migliori proprietà meccaniche utilizzando uno scarto agricolo a più ampia disponibilità e costo inferiore.

In tale contesto, la prima parte dello studio è stata dedicata alla caratterizzazione della lolla di grano e del canapulo, assunto come riferimento. Le procedure messe in atto sono conformi a quanto riportato in *RILEM Technical Committee 236-BBM 'Bio-aggregate based building Materials'*.
I risultati ottenuti hanno evidenziato come sia distribuzione granulometrica che forma degli aggregati siano influenzata dalle fasi di trasformazione subite. In particolare, le dimensioni della lolla risultano strettamente correlate alle dimensioni della cariosside di cui costituisce l'involucro. Al contrario, il canapulo proviene da un processo di macinazione industriale della parte legnosa dello stelo della canapa che genera una maggiore variabilità dimensionale delle particelle. I risultati prodotti mostrano un fattore di forma (*elongation factor*, definito come rapporto lunghezza-

larghezza (L/W)) minore per il canapulo. Considerando la compattazione uni-assiale subita dalla miscela fresca all'atto della posa nel cassero, il parametro valutato ha un effetto significativo sull'orientazione e impacchettamento degli aggregati sotto la pressione applicata. Inoltre, in conseguenza della diversa composizione chimica dei due aggregati, è stata riscontrata una densità assoluta leggermente più alta per la lolla di grano (1507 kg/m^3) rispetto al canapulo (1450 kg/m^3). Infatti, l'analisi chimica effettuata ha messo in evidenza una minore quantità di lignina nella lolla (10.9 %) rispetto al canapulo (21 %) e una maggiore quantità di cenere (1.1 % nella lolla di grano contro 0.6 % nel canapulo). Una delle differenze più marcate tra i due aggregati si osserva nella porosità che contraddistingue le particelle. La lolla di grano, infatti, risulta meno porosa (porosità intra-particellare 78 % rispetto a 85 % del canapulo) e caratterizzata da vasi di piccole dimensioni (diametro inferiore a 30 μm) rispetto al canapulo (diametro dei vasi compreso tra 50 e 90 μm).

Nonostante le differenze riscontrate, entrambi gli aggregati mostrano eccellenti proprietà igrotermiche (conducibilità termica secca di 0.05 W / (m·K) e MBV pari a 2.06 g/(m^2·%RH)). Questo risultato è estremamente significativo e supporta la possibilità di sostituire il canapulo con la lolla di grano nella realizzazione di *agro-concrete*. Infatti, i risultati hanno evidenziato come la lolla di grano non sia solo un buon isolante termico, ma anche un eccellente regolatore igrico.

A seguire, la lolla di grano è stata miscelata con un legante a base di calce (tradizionalmente utilizzato nel calcestruzzo canapulo-calce) e le proprietà termiche e meccaniche del composito ottenuto sono state confrontate con quelle del calcestruzzo canapulo-calce prodotto con lo stesso processo. In questo contesto, si è verificata la possibilità di sostituire direttamente il canapulo con la lolla di grano senza modificare i metodi di formatura esistenti. L'approccio di questo lavoro è quindi originale, in quanto sono state combinate tecnologie consolidate e know-how degli ultimi 20 anni sui calcestruzzi leggeri ottenuti con aggregati vegetali (di cui il canapulo-calce rappresenta un esempio) per lo sviluppo di nuovi materiali.
Nonostante la maggiore densità apparente secca del calcestruzzo lolla-calce, la porosità totale (circa 80 %) e la conduttività termica secca (circa 0.09 W/(m·K)) sono risultati simili per entrambi i tipi di calcestruzzo. Le prestazioni meccaniche leggermente inferiori per il calcestruzzo lolla-calce (~ 0.20 MPa) rispetto al

calcestruzzo canapulo-calce, sebbene in linea con i valori previsti dalla normativa francese per tamponamenti verticali senza requisiti di carico, sono da attribuire alla peggior adesione riscontrata tra matrice e superficie dell'aggregato lolla di grano.

Al fine di ottenere *agro-concretes* con migliori prestazioni meccaniche, le attività riportate di seguito sono state dedicate allo studio di un legante alternativo alla calce a base di MgO, caratterizzato da una migliore compatibilità con il nuovo *filler* vegetale. Nel dettaglio, diversi studi hanno riscontrato una maggiore compatibilità dei cementi a base MgO con *filler* organici. Infatti in conseguenza della loro bassa alcalinità (specialmente osservata per ossisolfato di magnesio, magnesio fosfato e ossicloruro di magnesio) il degrado delle particelle vegetali all'interno del calcestruzzo risulta inibita. Inoltre, un ulteriore vantaggio derivante dal loro impiego riguarda impatto ambientale e costi di produzione potenzialmente inferiori rispetto alla calce.
In questa fase, il lavoro è stato focalizzato sulla formulazione proposta da Sassoni *et al.* di un cemento ossisolfato di magnesio composto da soluzione acquosa reattiva di MgO e $MgSO_4$ con l'aggiunta di una farina ricca di proteine vegetali. Considerando le promettenti proprietà tecnologiche ottenute nel suo lavoro per pannelli in canapulo realizzati con questo legante, esso è stato ulteriormente studiato in questa tesi. Poiché nessun dato microstrutturale e composizionale è stato riportato da Sassoni *et al.*, la prima parte dell'attività è stata dedicata a questa indagine. In particolare, al fine di dedurre importanti conoscenze per lo sviluppo composizionale di *agro-concretes* e la scelta di percorsi di lavorazione adeguati per la loro produzione, è stato studiato l'effetto della farina vegetale (composta da proteine, carboidrati e lipidi) e $MgSO_4$ sulla cinetica di idratazione di MgO insieme alle proprietà microstrutturali a reazioni completate. I risultati hanno mostrato un effetto ritardante sull'idratazione del MgO sia degli ioni solfato che della farina vegetale, probabilmente attraverso interazioni elettrostatiche con la superficie reattiva. La cristallizzazione della fase $5Mg(OH)_2 \cdot MgSO_4 \cdot 7H_2O$, è stata favorita a 20 °C dalla presenza di farina vegetale a causa di modifiche della cinetica di idratazione di MgO. Temperature più elevate (35 °C) hanno inevitabilmente portato a una matrice composta principalmente da $Mg(OH)_2$ con ioni solfato non legati in reticoli cristallini. La farina vegetale ha evidenziato anche un effetto templante sulla matrice, producendo un elevata porosità. Quest'ultima dovrebbe favorire la permeabilità ai gas e quindi una carbonatazione

post-presa omogenea di $Mg(OH)_2$ presente nel cemento.

Sulla base delle informazioni acquisite, sono stati preparati nuovi *agro-concretes* utilizzando questo legante (*MOS cement* addittivato con farina vegetale) e i due tipi di aggregati vegetali precedentemente selezionati (lolla di grano e canapulo). Contrariamente a quanto sviluppato da Sassoni *et al.*, in questo lavoro è stata preferita una formatura a freddo. I risultati delle prestazioni meccaniche e termiche dei compositi ottenuti sono state confrontate con i precedenti dati raccolti per *agro-concretes* preparati con la matrice a base di calce.

La conduttività termica secca misurata per i calcestruzzi a base di cemento MOS è risultata leggermente superiore ai valori riscontrati per quelli a base di calce. Nel dettaglio, è stata notata una differenza dovuta all'uso dei due tipi di aggregati (0.119 W/(m·K) per il canapulo e 0.168 W/(m·K) per la lolla di grano). In aggiunta, maggiori resistenze a compressione sono state riscontrate per i calcestruzzi a base di cemento MOS. Questa osservazione è particolarmente evidente considerando i calcestruzzi contenenti la lolla di grano, per i quali è stata evidenziata una resistenza a compressione di 2.35 MPa già a 30 giorni di maturazione. Questi risultati possono essere motivati considerando la migliore compatibilità di cemento MOS, con la lolla di grano che ha portato a una migliore adesione legante-aggregato. In particolare, è stata osservata la cristallizzazione delle fasi cementizie non solo nella matrice ma anche all'interno dell'aggregato lolla di grano. La presenza di una fitta rete interconnessa di cristalli aciculari non soltanto all'interfaccia aggregato-legante, ma anche all'interno della struttura porosa dell'aggregato (a formare uno scheletro solido) ha portato ad un notevole incremento della resistenza a compressione del calcestruzzo.

In accordo con la classificazione stabilita da ACI Committee 213 *("Guide for structural lightweight aggregate concrete"*, American Concrete Institute, Committee 213 Report) inerente ai calcestruzzi leggeri, il calcestruzzo ottenuto dalla combinazione di cemento MOS e lolla di grano per i valori di resistenza a compressione riscontrati (2.35 MPa a 30 giorni di maturazione) può essere ritenuto idoneo per la realizzazione di blocchi isolanti che contribuiscono alla funzione strutturale svolta dagli elementi portanti nella struttura (resistenza a compressione >2 MPa, densità <1400 kg/m^3, conducibilità termica secca <0.3 W/(m·K). Inoltre, va notato che la resistenza a compressione di entrambi i tipi di calcestruzzo a base di cemento MOS è molto superiore al limite minimo (pari a 0.2 MPa) stabilito dalle

normative francesi (*French professional rules*) per la realizzazione di pareti di tamponamento verticale in canapulo-calce. Seguendo i requisiti dettati da queste normative soltanto i calcestruzzi a base di calce posseggono conducibilità termiche sufficientemente basse (<0.1 W/(m·K)) per poter essere idonei isolanti. Tuttavia, l'elevata resistenza meccanica dei calcestruzzi a base di cemento MOS fornisce un margine per migliorarne ulteriormente le prestazioni termiche e raggiungere i requisiti richiesti.

In sintesi, considerando i risultati ottenuti nel corso di questo lavoro, si può concludere che la lolla di grano ha un elevato potenziale di utilizzo come aggregato leggero/filler per la realizzazione di compositi o calcestruzzi isolanti, in alcuni casi con interessanti proprietà meccaniche. I risultati ottenuti sono di grande importanza, non solo perché viene proposta una soluzione per la valorizzazione e riciclo della lolla di grano, ma anche perché viene data una valida alternativa al calcestruzzo canapulo-calce. Infatti, l'elevata disponibilità di lolla di grano potrebbe incentivare ulteriori sviluppi di *bio-based insulations* in alternativa agli isolanti termici tradizionali.

Acknowledgments / Ringraziamenti

Vorrei ringraziare i Prof Cristina Siligardi e Tiziano Manfredini, che mi hanno dato la possibilità di lavorare a questo nuovo e interessante progetto, insieme alle risorse e strumenti necessari per poter svolgere questo lavoro. Grazie per aver creduto in me.

Un grazie di cuore va sicuramente alla Dott. Magdalena Gualtieri. Nutro una grande stima per questa persona e le sono veramente grata per tutto il tempo e le attenzioni che mi ha dedicato durante tutto il percorso del Dottorato. Molte delle conoscenze acquisite le devo a lei che con pazienza mi ha supportato e consigliato.

Spero di aver reso queste persone fiere del lavoro svolto e vorrei augurar loro il meglio per tutti i progetti futuri.

Ringrazio anche le Dott. Paola Miselli, Miriam Hanuskova, Fernanda Andreola e tutto lo staff tecnico di laboratorio per avermi aiutato e consigliato per alcune delle caratterizzazioni condotte.

Un ringraziamento speciale va anche ai Prof Florance Collet and. Christophe Lanos del Département Génie Civil - Construction Durable (IUT Rennes). Presso di loro ho trascorso i tre mesi più belli e stimolanti del Dottorato. Li ringrazio di cuore per avermi accolta nel loro gruppo di ricerca e avermi coinvolto in tutte le loro attività. Spero di poter proseguire anche in futuro questa interessantissima collaborazione.

Ringrazio anche le mie compagne di ufficio e le mie care amiche (Elly, Ele, Chiara, Consu) per avermi sempre ascoltato ed aiutato ad affrontare i momenti di difficoltà con un sorriso, sdrammatizzando situazioni a volte un po' pesanti.

Per concludere, un ringraziamento speciale va al mio compagno Enrico e tutta la mia famiglia per avermi supportato e sopportato. Sono stati per me un grande riferimento a cui affidarmi nei momenti di debolezza e senza i quali probabilmente non sarei riuscita a raggiungere quest'ambita meta.

Virginia

Contents

1 Introduction

1.1 Thermal insulations

According to the International Energy Agency (IEA), the building sector accounts for one-third of the total energy consumption and global carbon emissions in the world [3]. This includes not only consumptions and emission during construction of buildings but also during their service life. In particular, with the increasing demand of indoor thermal comfort, more and more energy (about 45 % of all the energy consumed in the planet) is used for heating, ventilation and air conditioning services [4]. In this context, the building envelope plays an important role since it strongly affects the surrounding microclimate [5]. Being the border between the internal and the external environment, it influences the thermal comfort of the inhabitants [6] [7] and the energy exchange during the building operating phase [8] [9]. Strategies and regulations for improving insulation performances of building envelopes have been implemented by several European countries [10] [11]. The progressive adoption of the EU legislation on energy-efficient buildings has boosted the use of thermal insulation in the overall building stock and has also increased the amount of insulation needed per building. In particular, as shown in Figure 1-1, the global market size of thermal insulation materials for building applications was estimated to about USD 22.73 billion in 2015 and was projected to increase, reaching USD 38.69 billion by 2027 [12]. The increasing demand for thermal insulation materials in building applications will be driven by measures for greenhouse gas emissions reduction, cost efficiency and government regulations on energy efficient buildings.

As pointed out by Jelle *et al.* [13], contributions to overall thermal behavior of the building envelop is not the only parameter that should be addressed when selecting insulating material. The choice must also consider non-thermal features such as sound insulation, resistance to fire, water vapor permeability and impact on the environment and on human health.

Liu *et al.* [14] classified the most common insulations into four categories on the basis of the raw materials used for their production: (1) from rocks and slags, such as rock-wool, glass-wool, expanded perlite, glass beads, vermiculite, cinder, ceramic products, etc.; (2) from petrochemical and coal chemical intermediate products, such

as polystyrene, polyurethane, polyethylene, etc.; (3) from metals, such as metal reflection film, hard metal visor, radiation plate, etc., the applications of which are still limited because they are much more expensive than other thermal insulation materials; (4) from plants, including agricultural waste, forestry waste and industrial plants fiber waste, such as straws, rice husk, wood shavings, cotton, corn crops, etc.

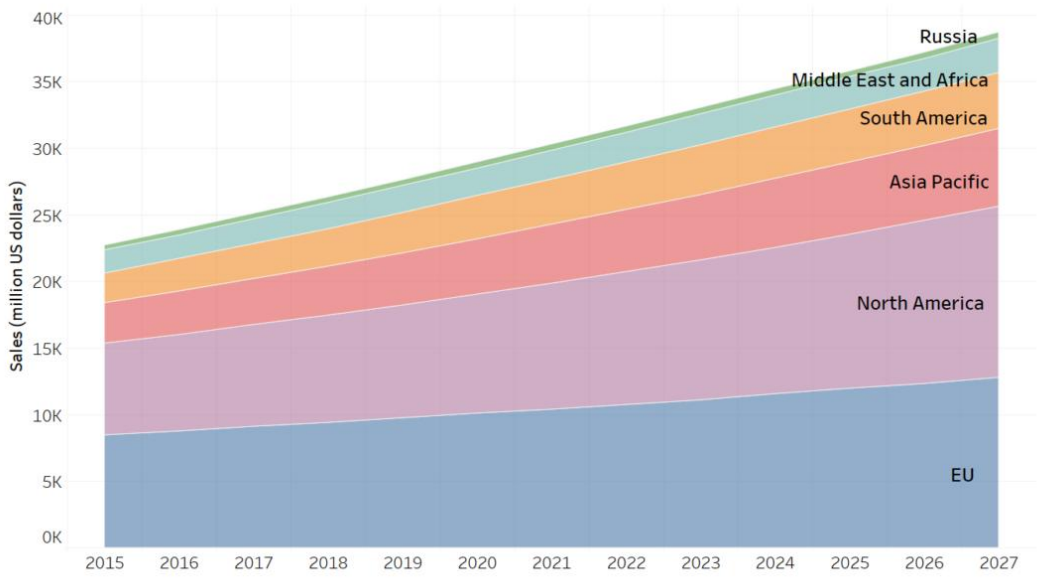

Figure 1-1: Global market forecast for building thermal insulation, by region [15].

As for thermal insulations made of rocks (e.g., rock wool, perlite, vermiculite, etc.), they generally do not have a satisfying environmental performance because various pollutants (CO_x, NO_x, SO_x, volatile organic compounds and particulate matters) are emitted during their energy intensive production process [14]. Moreover, most of the existing insulating materials are not renewable (e.g., those derived from petrochemical products) [13] [16]. Thus, renewable, environment-friendly, low cost, and high thermal resistance insulation materials are highly demanded. Thermal insulation materials from bio-composites, containing bio waste as filler/aggregate is promising to this aim [17]. Many EU-funded projects have been focused on the development of eco-friendly building materials containing locally available vegetable resources (see e.g. [18]) and several studies have been carried out on the use of these residue as filler/aggregate for the production of bio-based insulations with low embodied energy, low carbon footprint and high hygro-thermal efficiency [14].

1.1.1 Bio-based insulations

The growing interest in sustainable building materials is mirrored in increasing market shares of a insulation materials derived from biomasses, often named "*bio-based insulations*" or "*bio-insulations*" [19] [20] [21] [22] [23]. Interest has been paid to a wide range of agricultural by-products (such as hemp, flax, corn sunflower and cotton stalk, rice straw and husk, corn cob etc.) which could potentially be used as a renewable source. More precisely, the high porosity, low thermal conductivity and high moisture buffer value which characterize these by-products [24], make them particularly suitable for the production of insulation boards [17]. Moreover, they are easy and locally available and annually renewable since they come from fast-growing plantations.

Hence, bio insulations have not only the potential to become a valid alternative/substitute for less environmental-friendly traditional insulation materials but they also are highly interesting options for recycling of agricultural residue, whose management is an important issue considering their environmental hazard. In fact, the traditional ways of dealing with agricultural by-products/waste are firing and natural decomposition which are both highly polluting. More specifically, open air firing causes severe air pollution whereas natural organic decomposition favors methane emission [25]. This last process has a potent environmental effect in terms of greenhouse gas emission, as the global warming potential of methane is much higher than that of CO_2: 25-times more for a 100-year horizon and 72-times more for 20-year horizon [26]. Moreover, in many developing countries (like China, India, Brazil, Russia) the rapid growth of agricultural production combined with the decreasing consumption of biomass for housing heating (where biomass has often been substituted by natural gas or liquefied petroleum gas) has produced large amounts of biomass available [27], which need to find a proper valorization. Thus, the utilization of biomass as insulation material becomes a very interesting option both to avoid *in situ* burning and to save energy that would otherwise be wasted [28].

Research and development on bio-insulations for buildings with advanced technology has a very short history. According to the authors' investigation on this topic, most of the research was carried out after 1998 and has developed very fast in the last 15 years having attracted the interest of researchers from various countries [14]. There may be several reasons to the lack of interest in bio-insulations before

1998. In the authors' opinion, one reason is that the function of the buildings has changed with time. Before the 21st century, no attention was paid to the energy and environmental performances of building due to the lack of knowledge and awareness concerning environmental problems. Thus, not only bio-insulations but also other thermal insulations made of traditional materials have attracted little interest. Moreover, biomasses were used as primary fuel for domestic cooking in the past, especially in many developing countries where these utilization methods still persist. With the social progress, people's demand on indoor comfort became higher and higher, which led to a rapid increase of energy consumption. In this context, the development of thermal insulation in building sector was also supported by economic reasons as an effective way to reduce the energy consumption and, especially when taking the environmental-friendly features into account, bio-insulations began to draw increasing attention.

Some kinds of biomasses, such as straw, can be used in their natural form directly [29] [30]. However, most of them need to be treated before use in building materials. In general, the dry biomass is mechanically processed (e.g. cutting, smashing or crushing, etc.) or chemically treated. Subsequently, the product is mixed with other materials (e.g. other biomasses, foaming agents, binders, etc.) and processed into the final bio-insulation by a molding technique.

According to the literature [14], "*bonding molding*" is the most common manufacturing method to produce bio-insulations, followed by "pressing molding" or "hot-pressing molding".

In particular, bonding molding is a promising manufacturing approach because of the relative high mechanical performances, good thermal properties and acceptable density that can be obtained. The method foresees the use of one or more binders (organic or inorganic ones) [1] [31] [32] [33] [34]. The materials that are manufactured using this technique with inorganic binders are known as agro-concretes, cellulose aggregate concretes [35], bio-aggregates based building materials [36] or vegetal concretes [37].

1.1.1.1 Agro-concretes

A concrete in the conventional sense of the word consists of a heterogeneous mix between a mineral binder and aggregates (also mineral in origin) of graduated dimensions [38]. Similarly, agro-concrete is defined as follows:

> *"A mix between aggregates from lignocellular plant matter coming directly or indirectly from agriculture or forestry, which form the bulk of the volume, and a mineral binder"* [36]

As underlined in literature, this definition do not cover mixtures including:
– a low proportion of lignocellular aggregates (binder on aggregate mass ratio lower than 5);
– lignocellular plant fibers to reinforce conventional concrete (e.g. [39]).

Over the last years, a significant increase of various research activities about agro-concrete using vegetable resources as lightweight aggregate has been reported. Examples of studied materials are reported in Table 1-1. The table only includes studies performed on lightweight aggregates obtained from agricultural by-products/co-products, which yield concretes with a dry density lower than 1000 kg/m^3.

In Table 1-1 the geo-graphical distribution by country of the research works on agro-concrete topic is reported. As confirmed by other researches [14] [40], France is the world's leading investor in research activities/projects concerning environmental friendly, efficient multifunctional insulation systems as agro-concrete.

Table 1-1: Overview of research into agro-concrete: mixing mineral binders and lignocellular sources.

Plant	Vegetal source	Binder	Countries*	Ref.
Flax	Flax shives (agricultural co-product)	Portland cement (CEM I 52.5)	France	[41] [42] [43] [44]
Hemp	Hemp shives/hurds (agricultural co-product)	Portland cement (CEM II/B 32.5 R)	France	[45]
		(CEM I 42.5 R)	France	[51]
		Hydraulic lime (NHL3.5Z, NHL2)	France	[52]
		Lime based binder (hydrated lime+hydraulic lime)	France UK Italy	[46] [53] [54] [48] [50]
		(Tradical ® PF 70 - 75 % hydrated lime, 15 % hydraulic lime, 10 % pozzolana)	France Belgium Letvia	[46] [49] [51] [52] [53] [55] [54] [56] [57] [58]
		Mix of: hydrated lime (CL90s), hydraulic lime (NHL3.5), Portland cement (CEM I) and pozzolans	Ireland	[47]
		Clay	Romania France Spain UK	[59] [60] [61] [62] [63]
		Magnesia based binder (magnesium oxide+silica sand+sodium hydrogen carbonate)	Slovakia	[64]
		(magnesium phosphate cement)	Spain Letvia	[65] [58] [66]
		(magnesium oxychloride cement)	Letvia	[66] [58]
		(magnesium oxide + magnesium sulfate solution + vegetable flour)	Italy	[1] [2]
Rice	Rice husk (agricultural by-product)	Lime based binder (hydrated lime (CL90s), hydraulic lime (NHL3.5))	France	[67] [68] [69] [70] [71]

		(Magnesium oxysulfate cement + foam bubbles)	China	[34]
Sunflower	Sunflower stem (agricultural by-product)	Portland cement (CEM II/A-LL 42.5R)	Romania	[72]
		Lime based binder (fast setting hydraulic lime)	France	[73]
		(Tradical ® PF 70 - 75 % hydrated lime, 15 % hydraulic lime, 10 % pozzolana)	France	[73]
		(80 % of hydrated lime and 20 % of hydraulic binder)	France	[33]
		(CL90+pumice sand)	France	[74] [75]
		Metakaolin-based pozzolanic binder	France	[33]
Corn	Corn cob (agricultural by-product)	Portland cement	Portugal	[76]
		Soil	France	[77]
Rape	Rape straw (agricultural by-product)	Lime based binder (Tradical ® PF 70 - 75 % hydrated lime, 15 % hydraulic lime, 10 % pozzolana)	France	[78] [79]
Wheat	Wheat straw (agricultural co-product)	Lime	Romania	[80]
		Geopolymer	China	[81]
		Soil	Egypt	[82]

*location of the first author's Institution is taken into account.

1.1.1.2 Lime hemp concrete-a common agro-concrete

Lime hemp concrete is one of the most studied agro-concretes developed for buildings (see Table 1-1), nowadays a relevant alternative to traditional building envelopes. This material, obtained from the mix of hemp hurd (or shiv which is the woody inner part of the hemp stalk), water and a lime mineral binder, is used for several applications depending on the mix proportion [46]. The techniques for implementing hempcrete used today correspond to traditional techniques (casting in a formwork, as is done with cast concrete or traditional rammed earth) or techniques based on the adaptation of more modern procedures (vibro-compacting to make a building block, *in situ* spraying, etc.).

As shown in Figure 1-2 and Table 1-2, professional rules for the construction of hemp concrete structures [83] report the main characteristics and the implementation of the material depending on the specific application (wall, roof insulation or floor slabs).

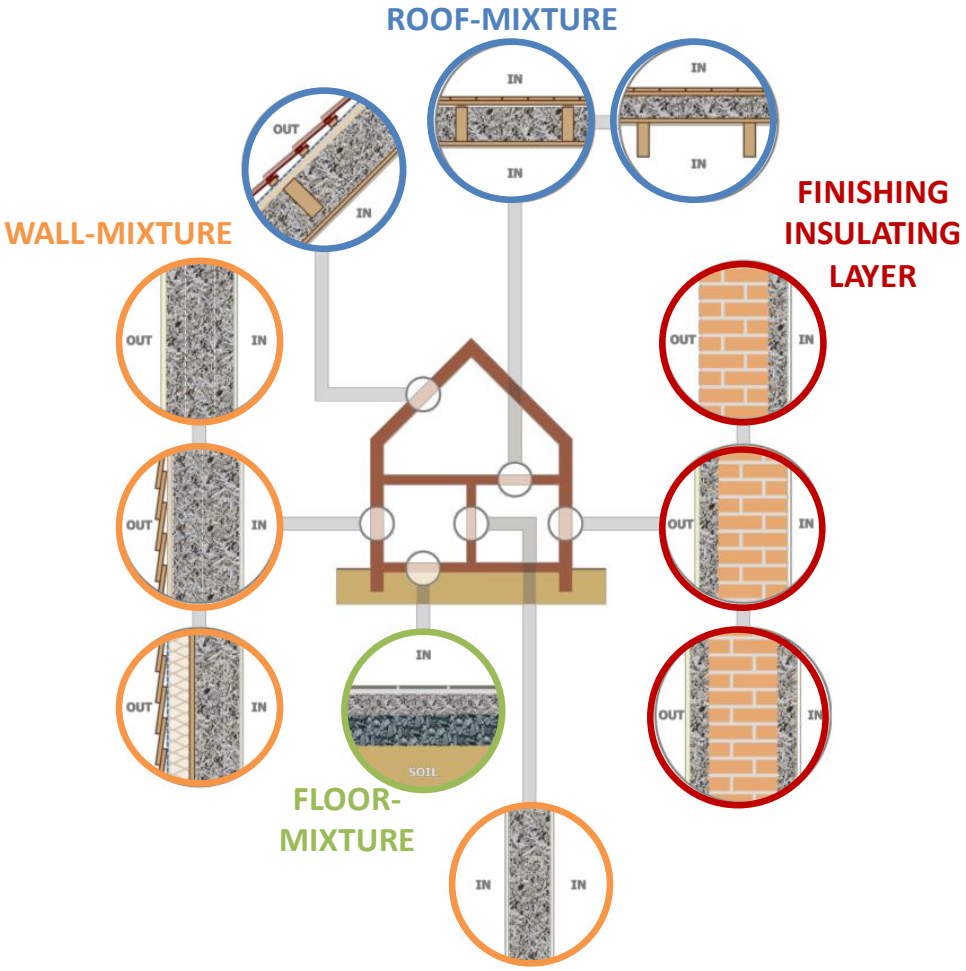

Figure 1-2: Applications of hemp concrete in housing [84]: wall mixture (orange circles), roof mixture (blue circles), floor mixture (green circles), finishing insulating layer (red circles).

Table 1-2: Main characteristics and minimum required mechanical performances of hemp concrete on samples cured at 20 °C and 50 %RH (French professional rules) [83] [84].

Application	**Wall**	**Roof**	**Floor**
Binder : shiv proportion (by mass)	2 : 1	1 : 1	1 : 3
Bulk density (kg/m^3)	350-440	200-250	500-600
Dry thermal conductivity (W/(m·K))	0.09-0.115	around 0.06	0.13-0.14
Minimum compressive strength (MPa)*	0.2	0.05	0.3
Minimum elastic modulus (MPa)*	15	3	15

*after 60 days of curing at 20 °C and 50 %RH.

Currently, lime-hemp concrete is common in France and has already been used in hundreds of new buildings. In Britain, both private and academic research have recently been carried out to test the claimed benefits of lime-hemp. As a consequence of the excellent results obtained in a few pilot projects, the new construction material is now available on the British market [85].

Thermal conductivity of lime- hemp concrete ranges from 0.06 to 0.18 W/(m·K) (in standard conditions: 50 %RH and 20 °C) depending on its density and formulation (see Table 1-2). In particular, wall mixture (dry density around 400 kg/m^3 and a binder to aggregates mass ratio of 2, see Table 1-2) should have a dry thermal conductivity around 0.9 W/(m·K), rising to 0.11 W/(m·K) at 50 %RH. Compared to other materials, the thermal insulation properties of lime-hemp concrete are located between cellular concrete (dry thermal conductivity of 0.12 W/(m·K) [86]), and mineral wool or expanded polystyrene (0.03-0.04 W/(m·K) [13]). Thus, it appears that thermal insulation properties of lime hemp concrete are good but not excellent as traditional insulation materials (EPS, XPS, mineral wall etc.). However, other benefits have to be taken into consideration while using this material. During its growth, hemp has taken up CO_2 through photosynthesis [87] while as the lime binder has sequestered CO_2 during hardening through carbonation. The final material thus results as carbon neutral or even negative, having sequestered from 6.67 to 136.65 kg CO_2 eq./m^3 [88] [89] [90]. Additionally, it also shows exceptional moisture buffering [91] [92] and acoustic insulation properties [93] [94]. Moreover, its low environmental impact compared to traditionally used building materials [89], makes them particularly suitable for requirements becoming increasingly demanding.

In addition to these aspects, there are minimum mechanical performances which must be respected so as to limit any structural problems. In particular, the minimum compressive strength and rigidity are proposed on the basis of the final use of the material (see Table 1-2 and Figure 1-2) [83].

When molding is used for manufacturing, lime hemp concrete is manually tamped into a wooden framework and usually cast on the building site. As the material is only slightly compacted during placing, the compressive strength of the hardened material does not exceed 0.5 MPa after 60 days [95]. It seems clear that the mechanical properties of these plant-based concretes may be considered as the main weakness point. Indeed, hemp based concretes cannot be used as load-bearing materials.

Several research projects have been conducted with a view to improving the mechanical properties of hemp concrete and also studying the parameters influencing its strength such as type of binder [33] [95] [96], binder content [93] [95], water content [97], physic-chemical properties of hemp aggregate [70] [95], manufacturing method [52], curing condition [95] and concrete's age [95]. In works carried out by Nguyen *et al.* [52] [56], authors highlighted a significant increase of compressive strength when hemp concrete specimens are placed with a high compaction load. However, this manufacture process can be detrimental to the concrete hygrothermal properties.

Many authors have studied aggregate surface treatments in order to reduce retardant effect of the soluble polysaccharides in binder hydration reactions. This method is fairly effective when Portland cement is used [42] [98]. However, when agro-concretes are designed with a lime-based binder, results are more controversial [74] [99] [100]. For instance, a degradation of surface wettability was observed which had a negative impact on the mechanical properties [74]. Moreover, the process is often pollutant, costly and thus not suitable for eco-friendly building materials development.

Diverging views exists on the role of hydraulic binders in hemp concrete and their contribution to the final strength. The presence of calcium silicate phases can promote early age strength as long as hydration is not hindered. However, according to some authors, using a binder with a high hydraulicity like Portland cement leads to an important powdering effect due to hydration disrupting prompted by the retardant effect of soluble polysaccharides as discussed above [101] [102]. In contrast, setting and hardening of hydrated lime binders (i.e. non hydraulic cement) are not significantly affected by soluble hemp constituents [96]. However, it must be pointed that for hydrated lime-based binders, carbonation contributes towards strength as the concrete ages [47]. Arnaud and Gourlay [95] have reported the evolution of lime hemp concrete compressive strength with time using a pre-formulated lime-based binder made up of air lime (75 wt.%). In particular, it was found that the increased compressive strength from 0.35 MPa to 0.85 MPa between 21 days and 24 months of curing was mainly attributed to slow binder carbonation.

1.1.1.3 Wheat husk: a potential renewable resource for agro-concrete

Wheat is the most common type of cereal used worldwide, and one of the most important raw materials for the food industry. According to the Food and agricultural Organization of the United Nations (FAO), its global production reached 770 million tons in 2017, of which 150 million tons were harvested in Europe [103]. It is the world's second most consumed grain because of its high production rate, its easy growth and versatility of use. After the industrial process for separating the grain kernel from the inedible hull, large quantities of wheat husk are generated as a waste material. According to the estimation done by Searle *et al.* for EU, the available wheat residue in 2020 will be 51 million tons [27] of which ca. 20 wt.% is wheat husk (i.e. ca. 10 million tons).

The traditional use of wheat husks includes bedding for animals and livestock feeding. Under particular conditions they can also be incinerated to produce green electricity or heat [104] [105].

However, energy-consuming pre-treatments of raw materials are often needed in order to optimize the conversion of biomass to energy [105]. In addition, incineration results in the production of volatile ashes that need to be disposed [106]. Recent work was focused on the valorisation of these ashes for the production of silica-based compound [107] [108]. However, in terms of carbon footprint, burning wheat residue is not a valid alternative. Just a few scientific investigations dealing with the direct use of wheat husk have been published and only as filler/reinforcement in organic matrix composites [109] [110]. In particular, Bledzki *et al.* fabricated polypropylene composites by injection molding with a fiber load of 40 wt.% [109]. Instead, Tran *et al.* prepared biocomposites using a polyactic acid matrix loaded with surface-modified husks [110].

As far as the author is aware of, wheat husk has not yet been investigated as filler/aggregate in bio-based composites. In addition, the large volume generated each year without any precise utilization still remains a relevant problem.

For the last 15 years, hemp has been considered as the reference agricultural resource for application in bio-based concrete. Although Europe is estimated to produce close to 1/4 of the world's hemp (about 46700 ha of hemp was cultivated in 2017 [111]), hemp hurds have never been amongst the most widely available agricultural by-products in Europe. Hence, it has become necessary to consider other possible sources of bio-aggregate available locally in greater quantities. From this aspect,

wheat husk is an excellent candidate with an availability being ca. 250 times higher that hemp hurd. Of course, this inevitably affects the price of resources and renders this vegetal residue highly interesting also from this aspect.

Considering a country like Italy where hemp is not widely produced (only about 4000 ha of hemp was cultivated in 2018 [112]) and where large quantities of hemp hurd destined to the building sector are imported from abroad (e.g. France), locally available alternatives are particularly desirable. In fact, shorter transport distances lead to lower carbon emissions and costs.

1.1.1.4 Lime: common inorganic binders for the production of agro-concretes

Lime is the main ingredient in the binder used in the hemp–lime wall construction. It is a processed material widely used in the building industry and is produced by heating calcium carbonate (limestone, chalk, seashells or coral rock) in a kiln to a temperature of approximately 900 °C. At this temperature, calcium carbonate is decomposed into calcium oxide (quicklime) and carbon dioxide. Approximately 1.7 tonnes of limestone is required to produce 1 tonne of quicklime and around 0.7 tonnes of CO_2 are given off [88]. Water and quicklime are combined to produce hydrated lime (calcium hydroxide) which is used in the building construction. During the life of a building, the embedded lime (calcium hydroxide) slowly carbonates by absorbing CO_2 from the atmosphere and change back to calcium carbonate, which contribute to the hardening and final strength of the material. It is possible to take up about 90 % of the CO_2 emitted from the calcination for pure lime [113]. In hemp concrete, hydrated lime also has strong antifungal and antibacterial effects (high pH), destroying sprout of fungi and bacteria in hemp after mixing [57].

The main drawback of agro-concretes containing lime as binder is the long time they require for complete carbonation. Thus, weak mechanical performances at early age is a major problem. Some studies focused on improving hardened properties of aerial lime-based hemp concrete with adequate proportions of pozzolanic additives (e.g. metakaolin, pulverized fuel ash, ground granulated blast furnace slag, microsilica, rice husk ash) [96]. These studies showed that low siliceous pozzolans (e.g. metakaolin with SiO_2/Al_2O_3 ratio of 1.13) should be preferred as the soluble fractions of hemp delayed the formation of silica hydrates whereas the formation of alumina hydrates was less affected [96]. Additionally, Lagouin *et al.* [33] obtained better water vapor storage and permeability performances for metakaolin based agro-

concrete than for lime based agro-concrete (80 % of slaked lime and 20 % of hydraulic lime). The authors thus demonstrated that a pozzolanic binder could be preferable not only due to improved mechanical properties and durability, but also for better hygric performances. In all studies cited above, the beneficial effects of pozzolan on agro-concrete compressive strength were only observed at medium/long age.

The current preferred strategy to obtain faster setting and improved early strength of aerial lime binder is to add hydraulic lime (e.g. NHL 2, NHL3.5) with C_2S as the main hydraulic constituent [67][113]. The contribution of hydraulic lime to the overall hardening process of the binder mixture is thus mainly C_2S hydration (i.e. formation of calcium–silicate–hydrates (CSH) and portlandite) [114].

Considering the published research discussed in the previous paragraphs, it is not surprising that the most common commercial binder formulation used in hemp concrete research (see Table 1-1) and products is *Tradical PF70*® which consists of 75 % hydrated lime, 15 % hydraulic lime and 10 % pozzolan [115].

1.1.1.5 Magnesia based binder for agro-concrete production

Recently, Walling and Provis [116] published a comprehensive review article on magnesium-based inorganic cements, focusing on scientific and patent literature. The authors categorized the various magnesia cements in five different classes: reactive magnesia; magnesium oxysulfate (MOS); magnesium oxychloride (Sorel); magnesium phosphate and magnesium silicate hydrate. The central constituent in all these cements is, by definition, MgO.

The use of MgO-binders in combination with various bio-based fillers such as wood [117] [118] [119], rape stalk [120], other agricultural residues [121], wood pulp [122], and also hemp [65] is not new. An important advantage of MgO-binders over lime-based ones is better compatibility with organic fillers [123] [124]. As underlined in the literature [66] [117] [125], the lower alkalinity of MgO-binders (observed especially for magnesium oxysulfate, magnesium phosphate and magnesium oxychloride cement) inhibits degradation of the vegetal particles inside the MgO-agro concrete. Additionally, concerning the environmental standpoint, the lower temperatures required for the production of reactive MgO through the calcination of magnesite ($MgCO_3$) (600-750°C) [126] compared to the conversion of

$CaCO_3$ to CaO (around 900°C) surely is a good motivation for using the former. In fact, the energy savings associated with this reduced temperature have led many to envision MgO-based cements as the future of ecofriendly cement production. Analogous to lime based binders, the hydration of MgO leads to the formation of brucite ($Mg(OH)_2$) which absorb CO_2 from the atmosphere producing hydrated carbonates and hydroxycarbonates (such as nesquehonite ($MgCO_3 \cdot 3H_2O$), dypingite ($Mg_5(CO_3)_4$ $(OH)_2 \cdot 5H_2O$), hydromagnesite ($Mg_5(CO_3)_2 \cdot 4H_2O$)), thus having the potential of being "carbon-neutral". These two interconnected aspects have led to a recent explosion in interest, both academic and commercial, in the area of MgO-based cements.

The main critical point connected to large scale use of MgO-based cement is connected to magnesite availability. Indeed, since now, calcination of magnesite ($MgCO_3$) is the principal route by which MgO is obtained for cement applications, but reserves of magnesite are geographically limited. In Europe, this mineral is sufficiently scarce (361 million tonnes) to be inserted in the 2014 EU *"Critical Raw Materials"* list [127]. China, North Korea, and Russia account for >65 % of global declared reserves [128], with China being the largest magnesite producer. Nevertheless, the production of reactive MgO from alternative sources such as industrial waste, seawater or brine has been reported and is still under development [126,129–133].

In this thesis work, a MOS cement was used as inorganic binder for the production of agro-concrete. Generally speaking, these binders are obtained by mixing reactive MgO with an aqueous solution of $MgSO_4$. The obtained cementitious phases are magnesium hydroxide sulfate hydrates with the general chemical formula $xMg(OH)_2 \cdot yMgSO_4 \cdot zH_2O$. The stoichiometry (x, y, z) depends on the reaction conditions [116].

As recently reviewed by Zheng *et al.* [134], the most studied $MgO\text{-}MgSO_4\text{-}H_2O$ system in recent years is based on the reaction between reactive MgO and $MgSO_4$ solution in the presence of citric acid, yielding needle-shaped $5Mg(OH)_2 \cdot MgSO_4 \cdot 7H_2O$ (so-called 517 phase) together with $Mg(OH)_2$ and residual MgO (e.g. [135] [136]). The 517 phase is particularly interesting due to its needle-like shape and low water solubility [135].

In this reaction scheme, the deprotonated citrate ligand prevent hydration of MgO particles through the formation of stable surface complexes, leading to longer setting

times that favors 517 phase crystallization. An important drawback is the increased amount of unreacted MgO particles in the hardened cement [136]. The presence of unreacted MgO can have detrimental effects on the mechanical properties of the cement due to post-hardening hydration in contact with water and consequent volume expansion [137].

In addition to citric acid [34] [136], other chemical modifiers for the crystallization of the 517 phase have also been investigated in literature, such as waste sulfuric acid [138], tartaric acid [139], weak boric acid, trisodium citrate [140]. All studies reported an increased water resistance and compressive strength in addition to a decreased drying shrinkage. These observations were explained by the formation of interlocking crystals of the 517 phase which filled up pores and micro-cracks, thus improving strength and volume stability of the MOS cement.

The 517-based cements, distinguished from traditional MOS cements through the use of chemical additives in the MgO-$MgSO_4$-H_2O system, have been called basic magnesium sulfate cement (BMS) [134]. The advantages of quick setting, low alkalinity, high mechanical strength (similar to Portland cement), good water resistance [134] [135] and low density (around 1600-1800 kg/m^3 compared to 2200-2500 kg/m^3 of lime) [135] underline the great potential of this emerging cementitious material in the manufacturing of agro-concrete.

Since now, only few articles reported in literature show the combination of hemp hurd with MOS cement. In this context, Sassoni *et al.* revealed interesting technological performances for hemp composites obtained by pre-heating and hot pressing at 80 °C of the fresh mixture [1] [2]. The binder used in their work was based on magnesium oxide and magnesium sulfate solution with the addition of a reactive vegetable protein in a flour-like form (organic modifier). Using a binder to aggregate mass ratio of 1 and a compression ratio of 1:1.7, they obtained light weight composite panels (bulk density of 330 kg/m^3) characterized by low thermal conductivity (0.078 W/(m·K) and extremely good mechanical performances (compressive strength of 1.15 MPa). Additionally, the fire resistance performances of the panels were better than many commercially available thermal insulating products based on natural fibers.

2 Aim of the work

Considering the need of increased sustainability in the building sector, novel eco-friendly materials are sought. Moreover, nowadays the rising amount of some type of agricultural residue is a global problem. Bio based materials using agricultural residues are highly interesting from both of these aspects and have therefore received much attention in recent years both in academia and industry. Many locally available vegetable by-products (e.g. sunflower pith, rice husk, corn cob, flax shiv etc) have been investigated as lightweight filler/aggregate in insulating agro-concrete. Among these, hemp hurd is the most popular ligno-cellulosic by-product used in the building sector. In particular, lime hemp concrete is nowadays a well-established insulating material, perfectly matching the crucial need for energy-efficient and affordable insulation layers with lower carbon footprint.

Among agricultural by-products, wheat husk residues represent an environmental hazard due to its huge annual production (10 million tons in Europe) and air pollution through conventional disposal methods (burning, natural decomposition). Hence, recycling options of this by-product is sought. This agro-cultural residue is low cost, renewable, local and easily available which surely are characteristics that form a good starting point for the development of sustainable building materials. Until now, wheat husk has not been investigated as filler/aggregate in bio composites despite its huge availability (250 times higher than hemp hurd).

In this thesis work, the fundamental idea was to combine: i) the need of the building sector for new materials with the same environmental advantages and better performances of lime hemp concrete but with higher availability and ii) the necessity of finding valid recycling alternative for wheat husk. To this aim, wheat husk bio-concretes were developed using two different inorganic binders, i.e. a traditional lime-based one as well as a magnesia binder.

Native wheat husk, i.e. without any energy-consuming pre-treatments, were used in the research. The desired outcome of these experiments was to verify the possibility of directly substituting hemp hurd with wheat husk without modifying existing forming methods. The approach of this work is thus quite original, combining well-established technologies and know-how in bio based building materials for the development of new materials.

The final goal was to develop alternative to lime-hemp concrete and eventually further improve the technological properties, mostly mechanical strength, by using an alternative inorganic binder.

In a recent work, Sassoni *et al.* proposed a MOS cement modified by a protein-rich vegetal flour for the production of hemp-based composites [1,2]. Considering the promising technological properties obtained for this bio based composite, the novel binder was further investigated in this thesis work. As no microstructural or compositional data was reported by Sassoni *et al.* [1,2], the first part was dedicated to this issue. Additionally, the effects of this type of organic additive (from renewable resources) in contrast to the chemical ones (reported above and usually used in literature) on binder hydration was full investigated. The results allowed to individuate the best manufacturing/curing conditions of the cement which were used for the production of agro-concretes in the final part of this thesis work.

3 Materials

In this chapter all raw materials used in the preparation of cements and bio based composite formulations are reported.

3.1 Lignocellular aggregates

As shown in Figure 3-1, two different crop by-products were used in this work: a) Commercial hemp hurd, which was taken as reference as it is already used in marketed bio-based composites; b) Locally available wheat husk coming from a cereal dehulling process operated by farmers' cooperative in San Felice sul Panaro (MO), Italy.

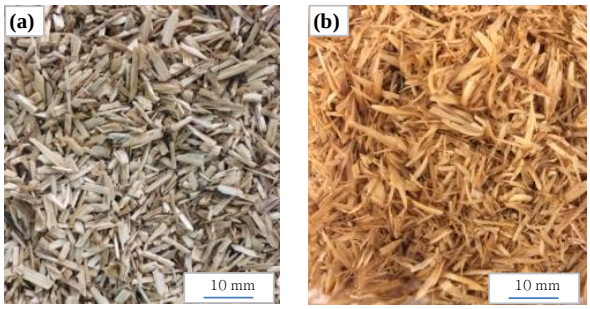

Figure 3-1: Crop by-products used in this work: commercial hemp hurd (a) and wheat husk (b).

3.2 Binders

Two types of binder were selected in order to produce bio-based composites with the lignocellular aggregates described in previous paragraph. In the first part of this thesis work, a traditional calcium lime based binder was used (see section 5.4.8.1) whereas later work was directed towards the use of a modified magnesium oxysulfate cement (see section 5.3). The reagents used for cement preparation are described here.

3.2.1 Calcium lime based binder

The calcium lime based binder was a 50/50 wt.% mixture of a lime putty (CL90S PL according to EN459-1:2010) from "La Banca Della Calce srl" and natural hydraulic lime (NHL3.5 according to EN459-1:2010) produced in Italy by "T.C.S. srl". Details concerning the chemical/mineralogical composition and results of physical characterizations are presented in section 5.2.1 and 5.2.2. This type of binder is

traditionally used for the production of lime hemp concrete in several industrial applications and it is also fully explored in literature.

Lime putty is an aqueous suspension of $Ca(OH)_2$. The binding capacity stems from slow carbonation ($Ca(OH)_2 + CO_2 \rightarrow CaCO_3 + H_2O$), leading to the formation of interlocking calcium carbonate crystals [141][142]. In order to obtain faster setting and higher strength at early ages, lime putty is often used in combination with natural hydraulic lime [143]. The technological properties of the latter product mainly depend on the phase composition, in particular the amount of C_2S which upon hydration forms calcium–silicate–hydrates (CSH) and calcium hydroxide [114].

3.2.2 Magnesia based binder

The second binder used in this work for the manufacturing of bio based composite is a inorganic binder, composed of magnesium oxide and an aqueous magnesium sulphate solution with the addition of reactive vegetal flour. Based on patent data [144], the molar composition was set to $12.1MgO{:}1MgSO_4{:}18H_2O$ and vegetal flour was added in an amount that corresponded to 25 wt.% of the MgO powder. The hydration kinetics and microstructure development of this binder was also investigated more thoroughly in separate experiments. This study included additional formulations in which some of the ingredients were emitted from the original composition (section 5.3.7).

The reagents used in the binder formulation were the following: Soft burned MgO (Balco, Italy); aqueous solution of $MgSO_4$ (25 wt.%) prepared by dissolving $MgSO_4 \cdot 7H_2O$ (technical grade, K+S KALI GmbH, Germany) in water; a vegetal flour (LAMERI S.p.A.). Full chemical and physical characterization of these components are reported in section 5.2.3 and 5.2.4, respectively.

4 Experimental procedures

This chapter reports a detailed description of the experimental procedures and characterizations employed in this thesis work for lignocellular aggregates (hemp hurd and wheat husk), binders and bio based concretes.

Unfortunately, no standards have yet been defined for biomass residue used as lightweight aggregates nor bio- based concretes (e.g. lime hemp concrete). Additionally, bio based aggregates exhibit specific properties in terms of shape/morphology, water absorption, bulk density etc. which are very different from traditional mineral aggregates typically used in the production of concrete. Hence, existing standards developed for traditional aggregates and concretes cannot be applied to lightweight organic aggregates and concretes thereof without modifications.

With the aim to define a characterization protocol derived from those used by the different laboratories and propose recommendations which are able to reduce the discrepancies resulting from the limitations and lack of adaptation of protocols for bio based aggregate and concretes, *RILEM Technical Recommendations* have been developed by a working group within the RILEM Technical Committee 236-BBM 'Bio-aggregate based building Materials'. Up to now, these recommendations only refer to aggregates whereas those for concretes are still under development. In this work, all characterizations performed on both hemp hurd and wheat husk follow the RILEM protocol [145]. Instead, testing procedures for biobased concretes were taken from previously published studies on this type of materials to ease comparison.

4.1 Characterization of the lignocellular aggregates

4.1.1 Scanning Electron Microscopy (SEM)

In order to evaluate the microstructure and surface morphology of lignocellular aggregates, SEM analyses were performed using an environmental SEM (ESEM Quanta-200, FEI company, UK) equipped with an INCA-350 (Oxford Instruments, UK) energy-dispersive X-ray spectroscopy analysis system. Samples were mounted on aluminium stub using silver glue and covered with a thin layer of gold in order to render the samples electrically conductive.

4.1.2 Chemical characterizations

4.1.2.1 Attenuated total reflectance Fourier transform infrared spectroscopy

FT-IR spectra were collected using a Vertex70v (Bruker Optics, Milan, Italy) coupled to an ATR accessory (Specac Inc., Woodstock, Georgia, USA) and a diamond cell. Absorbance spectra were obtained in the wavenumber range from 4000 to 600 cm^{-1}, acquiring 32 scans per sample at a resolution of 4 cm^{-1}. Following each scan, a new reference air background spectrum was taken. The system was operated using the OPUS software version 5.0 provided by Bruker Optics. Samples were dried at 60 °C until constant weight and subsequently stored in a desiccator until analysed.

4.1.2.2 Van Soest method

The compositions of vegetal aggregates were determined by the *Van Soest method* consisting in successive extractions of the various components of biomass, see Figure 4-1.

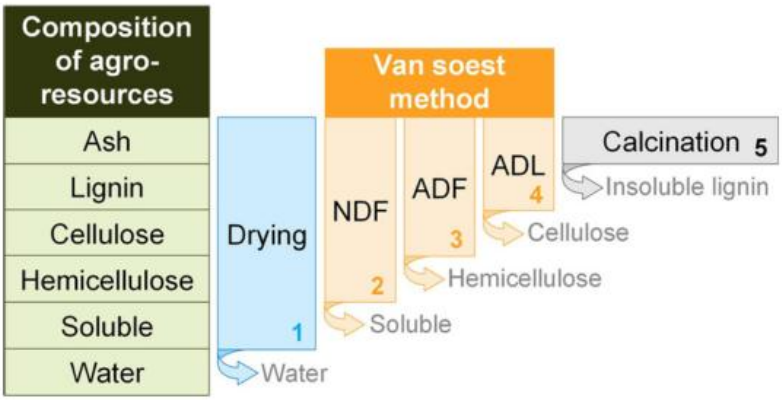

Figure 4-1: Simplified sketch of the Van Soest Method which is used for the accessment of biomass composition (see text for details).

The Van Soest soluble fraction was obtained using the standardized method [146] derived from the classic Van Soest procedure [147] as modified by [148]. About 500 mg of ground and sieved (1 mm mesh size) raw material were dried at 100 °C until constant weight in order to determine the percentage of dry matter (% DM). The three-step extraction procedure included an initial extraction in *Neutral Detergent Fiber* (NDF) solution at 100 °C for 1 h, using an ANKOM 2000 Automated Fiber Analyzer. This first step removes soluble cell contents like fat, wax, pectin, proteins and polysaccharides. The second extraction, necessary for hemicelluloses

solubilization, was performed at 100 °C for 1 h in *Acid Detergent Fiber* (ADF) solution. In order to remove cellulose, the third extraction was performed in *Acid Detergent Lignin* (ADL) solution for 4 h, using a Daisy incubator (Ankom). At the end of the extraction process, the residue fraction was composed of lignin and recalcitrant materials. In the last step, the ash content of the residue was determined by calcination at 550 °C for 3 h.

For each aggregate, this procedure was performed in three replicates. The content of ash, lignin, cellulose, hemicellulose and soluble matter were estimated with the following equations:

$$\%_{ASH} = \frac{M_{550}}{M_{sample} \cdot \%DM} \quad (4.\ 1)$$

$$\%_{LIGNIN} = \%_{ADL} = \frac{M_{ADL} - M_{550}}{M_{sample} \cdot \%DM} \quad (4.\ 2)$$

$$\%_{CELLULOSE} = \%_{ADF} - \%_{ADL} = \frac{M_{ADF} - M_{550}}{M_{sample} \cdot \%DM} - \%_{ADL} \quad (4.\ 3)$$

$$\%_{HEMICELLULOSE} = \%_{NDF} - \%_{ADF} = \frac{M_{NDF} - M_{550}}{M_{sample} \cdot \%DM} - \%_{ADF} \quad (4.\ 4)$$

$$\%_{SOLUBLE} = \frac{M_{sample} \cdot \%DM - M_{NDF} - M_{550}}{M_{sample} \cdot \%DM} \quad (4.\ 5)$$

With:

- M_{sample}: sample mass (mg);
- *%DM*: mass percentage of dry matter;
- M_{NDF}, M_{ADF} and M_{ADL}: mass (mg) of the sample after the first, second and last extraction;
- M_{550}: mass (mg) of calcined residue (550 °C for 3 h).

4.1.3 Physical characterizations

Sampling procedure.

In order to have a representative sample of lignocellular aggregates for each characterization, a quartering procedure of the starting batch was applied as illustrated in Figure 4-2 [145]. The importance of this operation is connected to the particles segregation induced by vibrations during transportation. Additionally, all samples were sieved and a nominal sieve aperture of 0.5 mm was set in order to evaluate the dust content [145]. Only the retained mass fraction between 0.5 and 5 mm was characterized and used in subsequent experiments.

Figure 4-2: quarting procedure of the lignocellular aggregates.

4.1.3.1 Particle size distribution.

Particle size distribution by sieving was performed in accordance with EN 933-2. Mechanical sieving was performed on 20 g of as-received samples (stabilized under laboratory conditions) using a Vibratory Sieve Shaker AS 200 (0.80 mm/g amplitude for 20 min).

Both particle size distribution and morphology was determined by an *image analysis method*, previously verified as suitable for hemp hurd aggregates [40]. Compared to sieving, this approach allows to obtain a more complete physical characterization of complex particle morphologies and heterogeneities. Electronical images of ca. 6000 particles were recorded by a high resolution camera (Canon EOS 5DS R) and the images were analyzed using the software imageJ. The operating instruction exposed by Amziane *et al.* [145] was followed. The 2D images of the particles were fitted with an ellipse [24] [149] and the resulting width and length (corresponding to the maximum and minimum axis) were used as particle descriptors together with the equivalent area diameter [67]. Figure 4-3 summarizes the image processing performed using imageJ.

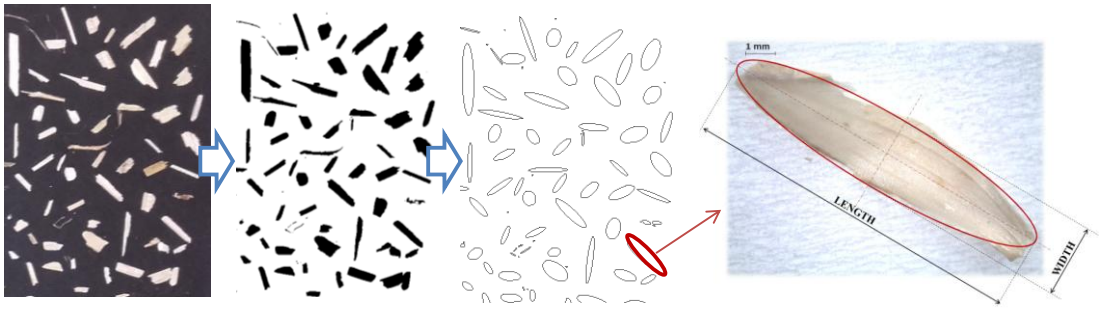

(a) (b) (c) (d)

Figure 4-3: Image processing performed using imageJ: Electronical image recorded by an high resolution camera (a), binarized image (b), ellipses fitting (c), length and width parameters (d).

4.1.3.2 Densities and porosities

Loose bulk density (ρ_b) was determined on lignocellular aggregates stabilized at laboratory condition (about 20 °C and 45 %RH). Tests were performed following the procedure outlined in Rilem TC BBM [145]. As illustrated in Figure 4-4, the procedure consists in filling about half the volume of a cylinder (100 mm in diameter and 200 mm in height) with lignocellular aggregates. In order to ensure a random distribution of particles, the cylinder was upended ten times (Figure 4-4a) and the horizontal level of lignocellular aggregates was marked (Figure 4-4b). Finally, bulk density was determined as the ratio of aggregate mass used in the test and the corresponding volume occupied by water (Figure 4-4c). For each type of natural particle (i.e. wheat husks and hemp hurds), three aliquots were analysed.

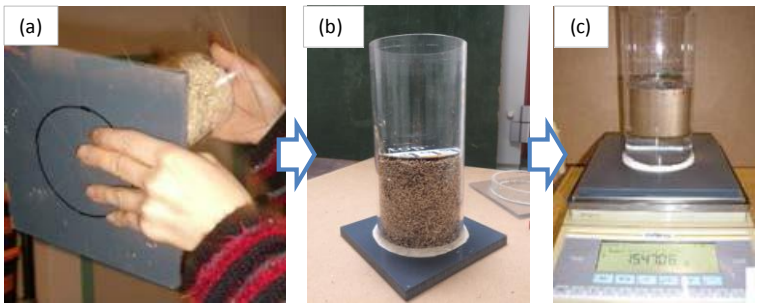

Figure 4-4: Procedure used for loose bulk density determination: upend of the cilinder in order to obtain a random distribution of lignocellular aggregates (a), mark the lignocellular aggregates level (b), determine the mass, and thus the volume (1g=1mL), of water needed for fill the cylinder until the level of the mark (c).

Absolute density was determined using a gas displacement pycnometer (AccuPyc 1330, Micromeritics Inc., USA). Analyses were done on as-received samples (ρ_{ar}) as well as on fine powders obtained by grinding (ρ_{ag}). In both cases, samples were dried at 60 °C until constant weight (ca. 24 h) and subsequently kept in a desiccator until analyzed.

Apparent particle density (ρ_p), was calculated according the following Eq. (4. 6) [67];

$$\rho_p = (1 - \eta_O) \cdot \rho_{ar} \tag{4. 6}$$

in which ρ_{ar} is the particles absolute density and η_O is the open porosity in the particle obtained with the expression (Eq. (4. 7)):

$$\eta_O = \frac{W_{max} \cdot \rho_{ar}}{\rho_w + (W_{max} \cdot \rho_{ar})} \quad (4.\ 7)$$

in which ρ_{ar} is the known absolute density, ρ_w is the density of water and W_{max} is the water sorption capacity of particles at saturation (see section 5.1.3.3).

Porosity estimations of the bulk, namely total porosity as well as inter- and intra-granular porosity, were calculated by the equations that are summarized in Table 4-1.

Table 4-1 Porosities of lignocellular aggregates (ρ_b=loose bulk density, ρ_{ag}=absolute density of as received particles, ρ_p=apparent particle density).

Porosity	**Equation**
Total porosity [η_T, %]	$\left(1 - \frac{\rho_b}{\rho_{ag}}\right) \cdot 100$
Inter-granular porosity [η_{inter}, %]	$\left(1 - \frac{\rho_b}{\rho_p}\right) \cdot 100$
Intra-granular porosity [η_{intra}, %]	$\eta_T - \eta_{inter}$

4.1.3.3 Water sorption

Water sorption was determined on lignocellular aggregates previously conditioned at 60 °C. The experimental protocol followed the recommendations of the Rilem TC BBM [145]. The amount of sorbed water was determined by sequential weighting after 1, 5, 15, 240, 1440 and 2880 min of immersion. At each time, the water content of the sample was calculated with the following equation (Eq. (4. 8));

$$w(t) = \frac{m(t) - m_0}{m_0} \quad (4.\ 8)$$

in which $m(t)$ is the mass of the wet sample at time t and m_0 is the mass of the dry sample.

For each aggregate, the measurement was performed on three samples.

4.1.3.4 Thermal conductivity

The thermal conductivity λ (W/(m·K)) was measured at 23 °C on bulk aggregate previously conditioned at 60 °C (dry state). As shown in Figure 4-5, a commercial CT-meter device equipped with a five-centimeter-long hot wire (Figure 4-5a) was used.

The measurement is based on measuring the temperature rise as a function of heating time. For cylindrical geometry, Blackwell [150] and Carslaw and Jaeger [151] solve the equation of heat conduction for a two media system including (i) the probe, assumed as an ideal infinitely thin and long line heating source, and (ii) the studied material, that constitutes an infinite surrounding and is supposed to be homogeneous and isotropic. For a sufficiently long time, there is a proportional relationship between temperature rise ΔT and logarithmic heating time ($ln(t)$) (Figure 4-5b) (Eq. 4. 9):

$$\Delta T = \frac{q}{4\pi\lambda} \cdot (\ln t + K) \qquad (4.\ 9)$$

in which q is the heat flow per metre (W/m) and K is a constant including the thermal diffusivity of the material.

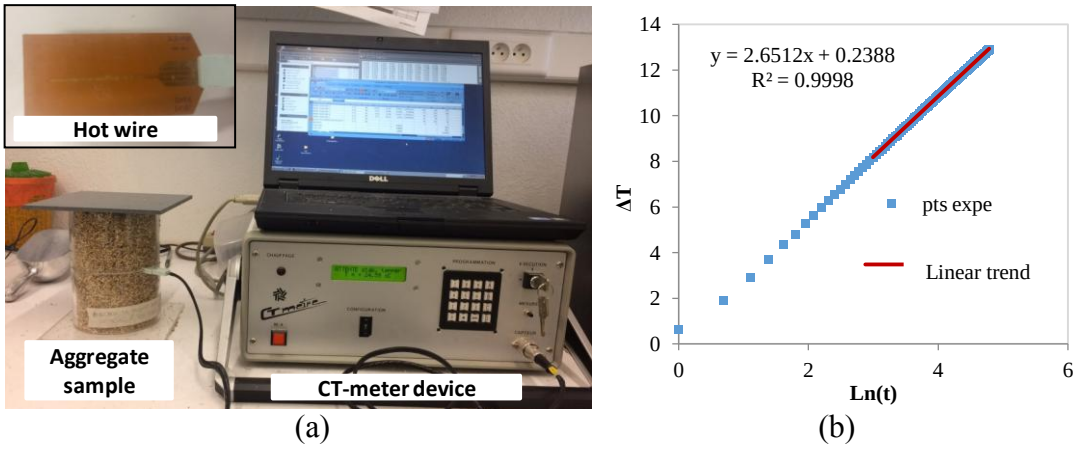

(a) (b)

Figure 4-5: Measurement of thermal conductivity on bulk aggregate: CT meter, hot wire and aggregate sample (a), experimental thermogram (b).

The heat flow and heating time were chosen in order guarantee a temperature rise high enough to obtain good correlation between experimental and calculated data (eq. 4. 9). In this study, the heat flow and the heating time were set at 0.147 W/m and 60 s, respectively. According to the manufacturer, the hot wire chosen for measurements is well adapted for values of thermal conductivities ranging from 0.02 to 5 W/(m·K) and the expected accuracy is 5 %.

As shown in Figure 4-6, when the aggregate samples were prepared, their bulk density were checked to ensure representativeness of the material. The upper side of the container is covered with a plate to prevent any moisture exchange during measurement. For each aggregate, the measurement was performed on five samples.

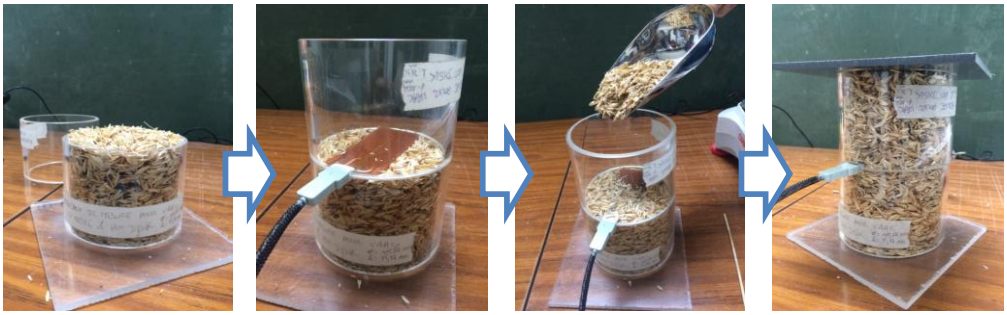

Figure 4-6: The bulk density must be measured: aggregate is placed in a known volume and weighed before and after the measurement.

4.1.3.5 Moisture buffer value

The moisture buffer value (*MBV*) quantifies the moisture buffering ability of a material. It is measured under dynamic conditions according to the method defined in the NORDTEST project [152]. This value relates the amount of moisture uptake (and release) per exposed surface area under daily cyclic variations of relative humidity according to Eq. (4. 10):

$$MBV = \frac{\Delta m}{A \cdot (RH_{high} - RH_{low})} \quad (4.\ 10)$$

in which *MBV* (kg/(m^2·%RH)) is the moisture buffer value, Δm (kg) is moisture uptake/release during the period, A (m^2) is open surface area, $RH_{high/low}$ (%) is high/low relative humidity level.

In this study, the aggregates were put in cylinders with a diameter of ca. 12 cm. The sample volume was about 1000–1200 cm^3. After stabilization at specific ambient conditions (23 °C; 50 %RH), samples were exposed to the following daily cyclic variations: 8 h at high relative humidity (75 %) followed by 16 h at low relative humidity (33 %).

Within the NORDTEST project, a round robin test was held on nine representative building materials. The obtained results led to a classification of moisture buffer values, as outlined in Figure 4-7.

The device used for MBV tests consists of a climatic chamber (Vötsch VC4060) that allows careful control of both temperature and RH in the ranges 10-95 °C and 10-98 %, respectively. The temperature was held constant at 23 °C whereas the relative humidity was adjusted manually according to the measurement protocol described above (75 % for 8 h followed by 33 % for 16 h). Temperature and relative humidity

were measured continuously with Sensirion SHT75 sensors in addition to the sensors of the climatic chamber.

The air velocity was measured in the surroundings of the exchange surface: the average horizontal value was in the range 0.07–0.14 m/s. The specimens were taken out of the climatic chamber and weighed, five times during the absorption period and two times during the desorption period. Considering the balance accuracy of 0.01 g, the accuracy of the moisture buffer value was estimated to be about 5 %. According to the NORDTEST project, stability is reached when the change in mass is the same between the last three cycles with a discrepancy of less than 5 %.

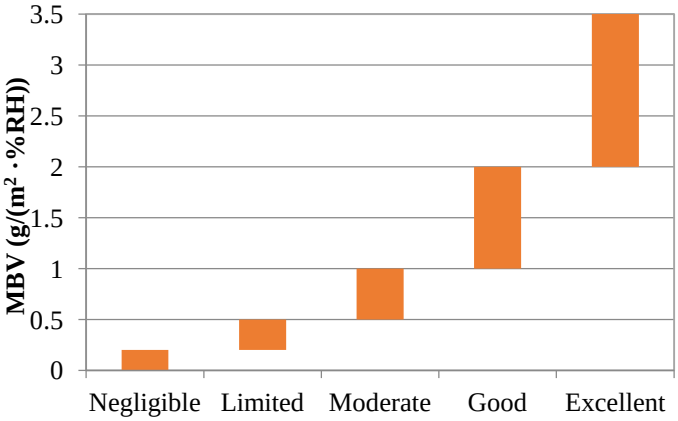

Figure 4-7: Ranges for practical moisture buffer value classes [152].

4.2 Characterization techniques used for powder reagents (raw binding materials)

The particle-size distribution of the MgO powder and the vegetal flour as well as anhydrous natural hydraulic lime powder (NHL 3.5) was determined using laser diffraction (Mastersizer 2000, Malvern, USA). Measurements were performed by quickly dispersing the powders in the carrier fluid (distilled water) followed by fast data collection. Stable readings were immediately obtained. Fast operation was motivated by the reactivity of the powders in water.

The amount of water absorbed by the vegetal flour was determined as follows: 180.0 mL of distilled water was poured in a graduated cylinder. In the next step, a known amount (ca. 25 g) of vegetal flour, weighted using an analytical balance, was slowly mixed with the water in the cylinder and the new volume was registered. The volume of the dry powder, calculated from the real density and the weight, plus the water used for the experiment was much bigger than the actual measured volume. This

difference was assigned to water absorbed by the particles. Assuming a water density of 1g/cm^3, the absorbed mass could be determined.

Attenuated total reflectance Fourier transform infrared (ATR-FT-IR) spectroscopy was also applied for the structural analysis of the vegetal flour included in some cement compositions (sample S1 and S2). The spectra were acquired in the range 4000-650 cm^{-1} with 32 scans at a resolution of 4 cm^{-1} using a FT-IR Vertex70v instrument equipped with a diamond crystal. Data were elaborated using the software OPUS 5.

Representative micrographs of vegetal flour and MgO powder were collected using a ESEM Quanta-200 instrument (FEI company, UK) equipped with an EDS INCA 350 system (Oxford Instruments, UK). Samples were mounted on aluminum stubs using carbon glue and subsequently gold-coated (Gold Sputter Coater, Emitech K550, UK). For MgO powder an accelerating voltage of 20 kV was used. Instead, imaging of vegetal flour was performed using a considerably lower voltage (1kV).

Chemical analyses by X-ray fluorescence were conducted on MgO powder and anhydrous NHL powder using a PhilipsPW1480 spectrometer. Compositional information was obtained by means of X-ray Powder Diffraction (XRPD) analyses. Data were collected using a conventional θ-θ laboratory instrument (X'Pert PRO, Panalytical, UK) equipped with a real-time multiple strip detector (X'Celerator, Panalytical, UK). Fine powders were mounted on glass sample holders by side-loading. Diffractograms were collected at ambient conditions with Cu $K_{\acute{a}}$ radiation, in the range 5-80 °2θ.

Thermogravimetric analyses (TG) in inert atmosphere (N_2 flux, Pt crucible, 10 °C/min heating rate up to 1000 °C) were performed on lime putty and natural hydraulic lime using a STA 429 CD, Netzsch, Geraetebau GmbH, Germany. The analyses were performed in order to estimate the quantity of $Ca(OH)_2$ and $CaCO_3$, calculated from the weight losses from the TG curves using stoichiometric formulas [71]. More precisely, the following weight losses were recorded: i) 400-550 °C: dehydroxylation of $Ca(OH)_2$, ii) 600-850 °C: decarbonation of $CaCO_3$.

Real density (ρ_{pr}) of dry powders (MgO, anhydrous NHL, dry solid lime putty and vegetal flour), was determined using helium picnometry (AccuPyc 1340, Micromeritics). The same powders were also analyzed by gas adsorption (N_2) and the well-known BET equation in order to determine the specific surface area (SSA, m^2/g).

Analyses were performed using a Gemini 2360 instrument (Micromeritics). The inorganic powders were conditioned under an N_2 flux at 110 °C prior to analyses whereas the conditioning temperature for the vegetal flour was 60 °C. The results from these analyses, together with the real densities (ρ_{pr}), were used to calculate the SSA particle diameter (µm) of the powder reagents (Eq. (4. 11)):

$$d_{SSA} = \frac{6}{\rho_{pr} \cdot SSA} \quad (4.\ 11)$$

Only a few additional physical characterizations (real density and SSA) were performed on the commercial lime putty used in the present work, since it was full characterized (with sample's name: S-5) in Gualtieri *et al.* [153]. Main information/results will be reported in section 5.2, together with to the other powder reagents.

4.3 Study of the magnesium oxysulfate cement modified by macromolecules

In this chapter, techniques and methods used to investigate the influence of vegetal flour on the hydration reactions of MgO is reported together with those applied for microstructural characterization of the hardened cement. The hydration kinetics were studied by isothermal and semi-adiabatic experiments whereas microstructural investigations were performed by electron microscopy techniques (SEM, TEM) as well as X-ray powder diffraction and quantitative phase analyses by Rietveld refinements.

The study contributes to the full understanding of parameters affecting the final phase composition of magnesium oxysulphate cements prepared using macromolecules of vegetal origin as chemical modifier, having important implications on the utility in lightweight concrete.

4.3.1 Magnesia binders composition

Table 4-2 shows the compositions of the four types of investigated cement pastes. The MgO was hydrated in the presence of i) an aqueous solution of $MgSO_4$ and vegetal flour (sample S1); water and vegetal flour (sample S2); only an aqueous

solution of $MgSO_4$ (sample S3); only water (sample S4). Composition S1 is similar to the cement studied by Sassoni *et al.* [1] whereas composition S2 is comparable to the cement studied by Jang and Li [154]. The different compositions were prepared in order to understand the influence of $MgSO_4$ and vegetal flour on setting/hardening and microstructure of the cements.

The binders were prepared as follows: the two solid reagents were weighted in separate polypropylene containers whereas the liquids (i.e. water and $MgSO_4$ solution) were mixed. In a subsequent step, the MgO powder was slowly added to the liquid under vigorous stirring.

A homogeneous paste was obtained following ca. 3 min of mixing. The vegetal flour (if envisaged) was slowly added to the paste during mixing for ca. 2 min. Cement samples for microstructural characterizations were prepared following, as closely as possible, the procedure previously used by Sassoni *et al.* [1] but without the addition of aggregate.

Table 4-2: Composition of reagents in fresh binders.

	Composition (wt.%)			
Sample	**MgO**	**$MgSO_4$ solution**	**H_2O**	**vegetal flour**
S1	36	33	22	9
S2	39	0	51	10
S3	52	48	0	0
S4	59	0	41	0

4.3.2 Hydration kinetics of MgO

4.3.2.1 Semi-adiabatic tests

In order to investigate the temperature development of the cement during setting, semi-adiabatic tests were performed. The tests consisted in measuring the temperature of the fresh cement paste as a function of time in a thermally insulated system. The freshly prepared binder (200.0 g) was placed in a polypropylene reactor and directly inserted in a Deware equipped with an insulating lid containing a small hole for hosting the thermometer (computerized, high-precision) in the centre of the paste. The placing temperature was 27 ± 0.4 °C. The experiment continued until the

sample started to cool down from maximum temperature. The repeatability was verified by multiple experiments.

4.3.2.2 Isothermal tests

Cement hydration tests were performed at 35 °C in small polypropylene reactors (2 mL) inserted in a stirred water bath (Thermo Haake K10 circulating chiller, ±0.02 °C in the range -10 °C to 100 °C). The temperature was chosen based on the results from semi-adiabatic experiments (see section 5.3.1.2), being slightly higher than the temperature at which accelerated hydration was observed (see section 5.3.1.2). The reactors were filled (2/3 of total volume) with fresh paste and placed in the controlled temperature environment. At regular time intervals, reactors were extracted from the water bath and directly placed in liquid nitrogen in order to stop the hydration reactions. The samples were freeze-dried (Lio 5P, CinquePascal, Milan, Italy), and the resulting dry powders were kept in a desiccator until analyzed by X-ray powder diffraction (see section 4.3.3). Using this technique, the evolution of the relative concentrations of the crystalline phases was followed as a function of time.

In one series, 7 aliquots (15 g) of fresh paste of sample S1 were placed in polyethylene bags (5 x 10 cm^2). The air was removed and the paste was smeared into a thin layer inside the airtight bag. In the next step, the bags were placed in a water bath holding a temperature of 20 °C. At pre-determined curing times (within 1 week), a bag was removed from the water bath and crushed. A representative portion (ca. 3 g) was extracted and left in 20 mL of isopropanol for at least 1 h in order to remove remaining water. Following filtration, the material was left to dry under ambient condition. XRPD analyses were preformed directly following drying. For comparison, exactly the same preparation procedure and curing conditions were also performed for one aliquot of paste with composition S3 cured for 7 days prior to analyses.

4.3.3 Characterization techniques

Microstructural analyses of hardened cements were performed using a ESEM Quanta-200 instrument (FEI company) in conjunction with energy dispersive Xray spectroscopy (EDS, INCA 350 system, Oxford Instruments). Samples were mounted on aluminum stubs using carbon glue and subsequently gold-coated (Gold Sputter Coater, Emitech K550).

Transmission electron microscopy (TEM) and scanning transmission electron microscopy (STEM) in the high angle annular dark field (HAADF) mode were performed using a Talos F200s G2 instrument (Thermo Fisher Scientific) equipped with a Schottky field emitter (S-FEG). These analyses were performed on hardened cements (S3 and S4) with the main scope to elucidate the effect of $MgSO_4$ on the crystal morphology of the hydration product. Elemental analyses and mapping were obtained through the use of a silicon drift detector. Samples for these analyses were prepared as follows: a small piece (ca. 10g) was extracted from the centre of the hardened cement (sample S3) and gently crushed in an agate mortar. The resulting powder was quartered and ca 0.1 g was dispersed in isopropanol and exposed to ultrasonification for 3 h. In the next step, the sample was left to sediment overnight after which the liquid was extracted and further diluted (isopropanol). Opposed to sample S3, composition S4 (MgO hydration in water only) did not result in a consolidated material but a suspension. Hence, the sample dispersed in isopropanol was obtained by mixing some drops of the suspension with the solvent and subsequently follow the procedure described above for sample S3. Copper grids with carbon film were used as sample holders. Particles were deposited on the grid by dipping in the sol (visible effect of Tyndall scattering).

Compositional data were obtained by means of X-ray Powder Diffraction (XRPD) analyses using Bragg-Brentano geometry and Cu Kα radiation. Data were collected using a conventional θ-θ laboratory instrument (X'Pert PRO, Panalytical) equipped with a real-time multiple strip detector (X'Celerator, Panalytical). Fine powders were mounted on glass sample holders by side-loading. Rietveld refinements were applied for quantitative determinations using the GSAS-EXPGUI software [155,156].

As done in previous work [153], data collected from standard powder (NIST 676a) using the same experimental setup as the one used for samples were applied for calibration of the Kα1/Kα2 ratio, the polarization as well as the profile terms GW, LY and Asym in the "type2" profile shape model [156]. These parameters were fixed in all refinements and only the profile parameter LX was refined in sample analyzes. $Mg(OH)_2$ showed anisotropic peak broadening, wherefore the parameters *stec* ("type 2" profile shape model in GSAS) was refined. The background (shifted Chebyshev function with 12-15 terms), the zero shift and scale factors were refined. If needed, the preferred orientation of the (002) peak of 517 MOS was refined using the March–Dollase model implemented in GSAS [156].

The applied structure models of the major phases were the following: α-alumina [157]; 517 MOS [135]; $Ca(OH)_2$ [158]; MgO [159]; $Mg(OH)_2$ [160]; $CaSO_4 \cdot 2H_2O$ [161].

The amorphous fraction was determined by adding an internal standard (10 wt.% α-alumina, NIST 676a) and rescaling the refined quantities with respect to the standard following previously described procedures [162]. Reported errors for the amorphous and crystalline phase fractions were calculated according to the procedure described by Madsen and Scarlett which reflects the uncertainty of the mathematical fitting associated with the Rietveld refinement process [163]. The X'Pert HighScore Plus software was used for qualitative analyses and profile fitting. The conversion factor for crystallization of $Mg(OH)_2$ ($\alpha_{Mg(OH)2}$) and dissolution of MgO (α_{MgO}) were calculated according to the following corresponding equations;

$$\propto^{t}_{Mg(OH)2} = \frac{I^{t}_{Mg(OH)2}}{I^{max}_{Mg(OH2}} \quad (4.\ 12)$$

$$\propto^{t}_{MgO} = 1 - \frac{I^{t}_{MgO}}{I^{max}_{MgO}} \quad (4.\ 13)$$

where $I^{t}_{Mg(OH)2}$ and I^{t}_{MgO} is the area of the (101) peak (brucite structure) and the (102) peak (periclase), respectively, following *t* min of hydration. Likewise, $I^{max}_{Mg(OH)2}$ and I^{max}_{MgO} are the maximum peak areas coinciding with time zero for MgO and completion of hydration reaction for $Mg(OH)_2$.

The instrument used for ζ-potential measurements at 25 °C was a Zetasizer Nano Series from Malvern. For these experiments, MgO was hydrated in distilled water using the same solid/liquid ratio as used for sample S4. The hydrated product (i.e. $Mg(OH)_2$) was diluted with distilled water and left to equilibrate for ca. 3 h prior to measurements. In order to observe the effect of sulfate ions on the surface properties of $Mg(OH)_2$, measurements were repeated following the addition of a 0.1 M $MgSO_4$ solution (25 vol.%) and re-equilibrating.

Real density, measured on both fine powders (ρ_{rp}) and consolidated binder samples (ρ_{rc}, g/cm^3), were determined using helium picnometry (AccuPyc 1340, Micromeritics). The apparent density (ρ_{app}, g/cm^3) of dry binder specimens were determined using a GeoPyc 1360 instrument (Envelope and T.A.P Density Analyzer,

Micromeritics). The total porosity (TP, %) and the open porosity (CP, %) was calculated from eq. 4. 14 and eq. 4.15, respectively:

$$TP(\%) = 100 \times \left(1 - \frac{\rho_{app}}{\rho_{rp}}\right) \quad (4.\ 14)$$

$$CP(\%) = 100 \times \left(1 - \frac{\rho_{app}}{\rho_{rc}}\right) \quad (4.\ 15)$$

4.4 Concrete design

In Table 4-3 are presented the four types of concretes prepared combining the two types of lignocellular aggregates selected for this work (i.e. wheat husk and hemp hurd) and two binders. The first one is a 50/50 wt.% mixture of a lime putty (CL90S PL) and natural hydraulic lime (NHL3.5), fully explored in literature and also used in industrial applications [48,49,55,56,88,164]. The second one is a magnesium sulfate binder (prepared using reagents described in section 3.2.2) that could be an interesting alternative or even better to the previous. Based on patent data [144], the molar composition of the inorganic portion of the binder was 12.2MgO: 1$MgSO_4$: 18H_2O whereas the amount of added vegetal flour was 25 wt.% based on the weight of MgO.

For all concretes, a binder to aggregates mass ratio (B/A) of 2 was chosen as this is common practice in the manufacturing of lime hemp concrete.

Table 4-3: Mixtures notations.

Concrete	Notation	B/A mass ratio	Application*	Aggregate	Binder
Lime Hemp Concrete	LHC	2	Wall mixture	Hemp hurd	lime-based binder
Lime wheat concrete	LWC			Wheat husk	lime-based binder
Magnesia Hemp Concrete	MHC			Hemp hurd	magnesia-based binder
Magnesia wheat concrete	MWC			Wheat husk	magnesia-based binder

*Professional rules for the construction of hemp concrete structures [83] report the main characteristics and the implementation of the material depending on the specific application. Hemp concrete is used for walls (filling of outer walls, doubling of load-bearing walls, etc.), roof insulation or even floor slabs [84].

The mix proportions and the fresh density of all concrete are reported in Table 4-4.

Table 4-4: Mix proportions and fresh density of lime based concretes (LHC and LWC) and magnesia based comcretes (MHC and MWC).

Mixture	W/B[a]	Binder [kg/m^3]	Aggregate [kg/m^3]	Wb[b] [kg/m^3]	Wp[c] [kg/m^3]	Fresh density [kg/m^3]
LHC	2.1	232	116	139	348	835 ± 21
LWC	1.6	306	153	184	306	950 ± 19
MHC	2.3	215	105	185	316	822 ± 31
MWC	1.8	355	174	306	349	1184 ± 23

[a] W/B is the water(W=Wm+Wp) to binder (B) mass ratio.
[b] Wb is the water used in binder preparation.
[c] Wp is the prewetting water of lignocellular aggregates (see section 5.1.3.3 for experimental procedure).

As a consequence of the different physical properties of the two type of aggregates (full characterized in section 5.1.3), it was difficult to reach the same fresh density of concretes made with same binder, using same B/A and compaction pressure. Moreover, the high discrepancy between the fresh density observed for MWC and other concretes suggests particular interaction between wheat husk aggregate and magnesia binder that could affects the packing behavior of the fresh concrete mixture under compaction.

The weight ratio between the mixing water (W_b) and the binder was 0.6 for lime based concretes (LHC and LWC) and 0.8 for magnesia based concrete (MWC and MHC). Additionally, the prewetting water (W_p), corresponding to the amount of water uptake by lignocellular aggregates after 1 min of water immersion, was determined experimentally (see section 5.1.3.3).

The fresh concretes were prepared as follows: the lignocellular aggregates were homogenized in a mixing drum with the prewetting water for about 2 min. At the same time, the binder was prepared in a separate concrete mixer.

In case of magnesia cement, the two solid reagents (i.e. MgO powder and vegetal flour) were weighted in separate polypropylene containers whereas the liquids (i.e. water and $MgSO_4$ solution) were mixed. In a subsequent step, the MgO powder was slowly added to the liquid under vigorous stirring by hand. A homogeneous paste

was obtained following ca. 3 min of mixing. In the next step, the vegetal flour was slowly added to during mixing for ca. 2 min. Regarding the lime based binder, hydrated lime (CL90S PL) and hydraulic lime (NHL 3.5) were carefully homogenized together with the mixing water W_m (ca. 4 min).

In the last step, the prewetted lignocellular aggregates were mixed with the cement until a homogeneous concrete was obtained. The total mixing time did not exceed 15 min.

Samples for thermal conductivity measurements were prepared as follows: the fresh concrete was placed in 100 x 50 x 150 mm^3 molds and compacted in 3 layers using a steel manual device. Each layer was subjected to a slight pressure (ca. 6 kPa). Three pilot pins were inserted in the freshly prepared sample and removed following curing, thus leaving holes that were used to host the sensor for thermal conductivity tests. The pilot pins were positioned with a minimum distance of 25 mm following the recommendations of the instrument manufacturer. Samples for mechanical tests were prepared using the same procedure as the one described above (i.e. compaction with slight pressure), with the exception of the number of compacted layers (1 instead of 3) and the use of smaller molds (50 x 50 x 50 mm^3).

Sample dimensions and details regarding the compaction process for samples subjected to compressive and thermal tests are summarized in Figure 4-8.

All samples were demolded after 48 h and stored in laboratory at 18±2 °C and 55±5 %RH prior to characterization.

Based on the results obtained in the previous study performed on magnesium oxysulfate cement modified by macromolecules (see section 5.3) a cold forming processes was chosen for magnesia concrete (MHC and MWC) made with this type of binder.

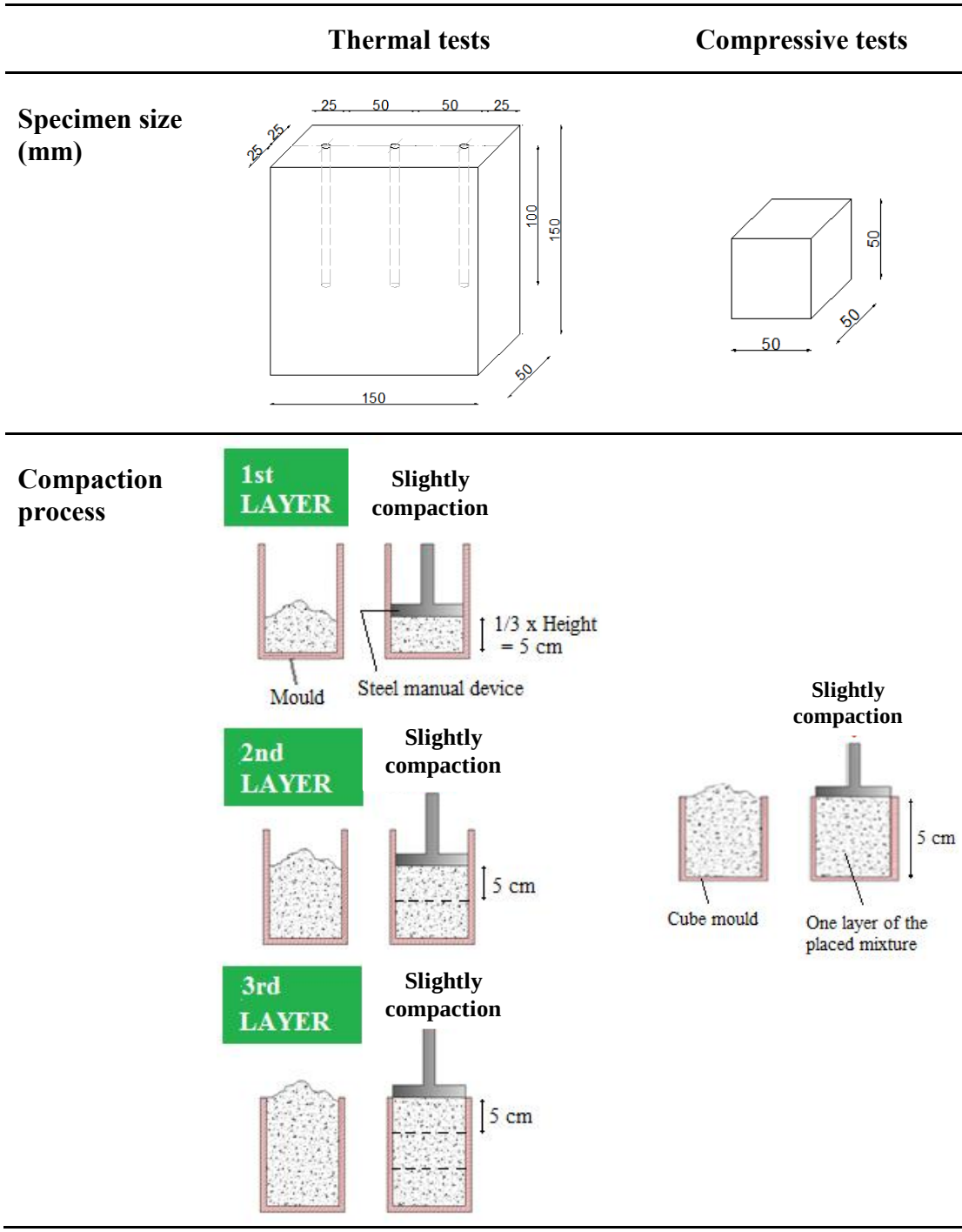

Figure 4-8: Bio-based concrete specimen size and compaction process for thermal tests and compressive tests.

4.5 Characterization of bio-based concrete materials

4.5.1 Kinetic of hydric stabilization

The hydric stabilization of the concrete samples was investigated by recording the weight at regular time intervals during the curing period. The mass loss (Δm) at each

investigated curing time was calculated according to the following equation (Eq. (4. 16));

$$\Delta m\ (\%) = \frac{m_0 - m_t}{m_0} \cdot 100 \quad (4.\ 16)$$

in which m_0 is the mass of the fresh mixture placed in the mold and m_t is the mass measured at curing time *t*.

4.5.2 Densities and porosity

Apparent density at hydric stabilization (ρ_{hs}) was calculated from the weight and volume of the concrete sample that reached hydric stabilization. The weight was determined with a balance (0.01 g) whereas the three dimensions were measured with an electronic calliper (0.1 mm). Each dimension was the average of four values. This method follows the recommendations of the standard NF EN ISO 12570 describing the determination of apparent density of composites (i.e. mass and volume accuracy of ca. 0.1 % and 1 %, respectively).

Dry apparent density (ρ_{dry}) was determined in the same way as ρ_{hs}, but using concrete samples (stored for 30 days at 18±2 °C and 55±5 %RH). Prior to analyses, all concrete samples were dried. The temperatures were chosen based on the thermal stability of the magnesia-based binder [140] and common practice for lime-based biocomposites [36].

Absolute density (ρ_{abs}) was determined using a gas displacement pycnometer (AccuPyc 1330, Micromeritics Inc., USA) on dry concrete powders obtained by grinding samples previous used for ρ_{dry} determinations.

The total porosity (η_{tot}, %) of dry concretes was determined based on the following equation;

$$\eta_{tot}(\%) = \left(1 - \frac{\rho_{dry}}{\rho_{abs}}\right) \cdot 100 \quad (4.\ 17)$$

in which ρ_{dry} and ρ_{abs} are the dry apparent density and the absolute density, respectively.

4.5.3 Thermal conductivity measurements

Thermal conductivity was measured using the instrument KD2 Pro from Decagon Devices on concrete samples (LHC, LWC, MHC and MWC) cured for 30 days. Prior to measurements, magnesia based concrete samples (MHC and MWC) were conditioned at 50 °C until constant weight, whereas the corresponding temperature for LHC and LWC samples was 60 °C. Following drying, the samples were stored in sealed plastic bags until analyzed. Thermal conductivity measurements were performed in a conditioned room holding a temperature of 20 ± 1 °C. The operation of the KD2 Pro instrument relies on the infinite line heat source theory and calculates the thermal conductivity by monitoring the dissipation of heat from the needle probe. Heat is applied to the needle for a specific heating time, t_h, and temperature is monitored in the needle during heating and for an additional time equal to t_h after heating [165]. The TR-1 probe (2.4 mm in diameter and 100 mm in length) was used for measurements. The read time, during which data are taken to compute thermal properties, was set at 10 min in order to prevent errors caused by effects from the large diameter needle and contact resistance between sensor and sample. Thermal grease was used to guarantee a good contact between the needle and the concrete. The sensor needle was placed perpendicular to the direction of compaction applied during sample preparation (see section 4.4), as this corresponds to the main heat flow direction through the wall in a real application. In fact, as described in the introduction, the concrete is manually tamped perpendicular to the wall thickness into a wooden framework on the building site.

As described in section 4.4 (see Figure 4-8), the concrete samples for these measurements contained three holes allowing measurements in different parts of the concrete samples. Reported values are means of these three values, accompanied by standard deviations.

4.5.3.1 Modelling thermal conductivity of bio-based concrete: self consistente scheme

The theoretical thermal conductivity for the solid phase of agro-materials was evaluated at 20 °C using the *self-consistent scheme.*

As proposed by Collet *et al.* [46] and Rahim *et al.* [166] and presented in Figure 4-9, the agro-material geometry was assumed to be an assembly of spherical composite spheres of various sizes (Figure 4-9 a). For a two-phase medium, a sphere of radius

Ra (phase *a*) is embedded in a concentric spherical shell of external radius *Rb* (phase *b*). This composite sphere is embedded in a homogeneous and isotropic equivalent medium (Figure 4-9 b).

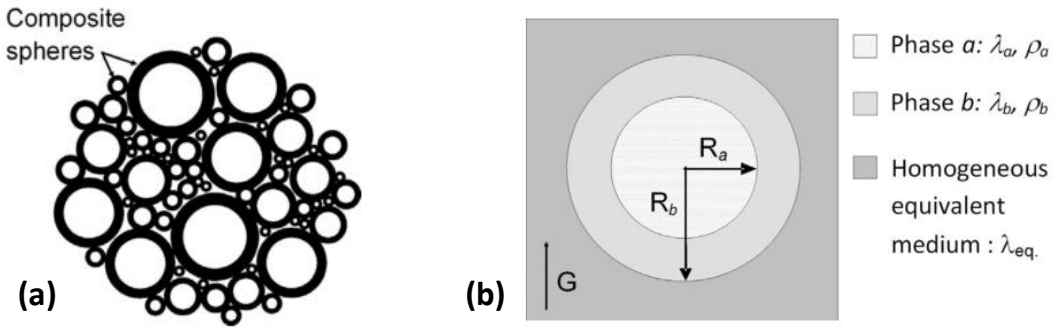

Figure 4-9: SELF CONSISTENTE SCHEME: two-phase model [46][166]. The agro-material geometry was assumed to be an assembly of spherical composite spheres of various sizes (a); a sphere of radius *Ra* (phase *a*) is embedded in a concentric spherical shell of external radius *Rb* (phase *b*). This composite sphere is embedded in a homogeneous and isotropic equivalent medium (b).

The approximation of the effective conductivity is based on the assumption that the energy embedded in the heterogeneous medium is equivalent to that of the equivalent homogeneous medium under the same boundary conditions. The effective conductivity is thus linked to the volume ratio *n* of the inner to the outer radius according to (Eq. 4. 18);

$$\lambda_{eq} = \lambda_b \cdot \left(1 + \frac{n}{\left(\frac{1-n}{3} + \frac{1}{\frac{\lambda_a}{\lambda_b} - 1} \right)} \right); n = \left(\frac{R_a}{R_b} \right)^3 \quad (4.\ 18)$$

in which $\lambda_{a\ (resp.b)}$ is the thermal conductivity of phase *a* (resp. *b*).
In this study, the two phase model is used for dry material considering air as phase *a* and solid matrix (including aggregate and binder) as phase *b*, *n* is thus the porosity of the material. The thermal conductivity of the solid phase (λ_b) is calculated by fitting the experimental data with the self consistent scheme using the least square method.

4.5.4 Thermogravimetric analysis (TGA) on hardened lime binder

The hardened lime binders were characterized by means of thermogravimetric analyses (TG) using a STA 429 CD, Netzsch, Geraetebau GmbH, Germany.

Analyses were conducted in inert atmosphere (N_2 flux) in the temperature range from 20 °C to 1100 °C using a heating rate of 10 °C min^{-1}.

Powdered binder specimens were collected from the bulk of the samples as well as from the surface following 10, 30, 150 days of curing. The powders were sieved (80 μm mesh size) before being analyzed in order to remove plant particles.

A quantitative estimation of the hydrated phases and the carbonates, i.e. hydrated lime and $CaCO_3$, were calculated from the weight losses determined from the TG curves using stoichiometric formulas [71].

More precisely, the following weight losses were recorded:

- 100-400 °C: loss of water from C–S–H hydrates [167]
- 400-550 °C: dehydroxylation of $Ca(OH)_2$
- 600-850 °C: decarbonation of $CaCO_3$

Additionally, the amount of the newly formed $CaCO_3$ was calculated considering the difference between the initial content of $CaCO_3$ in unhydrated lime and the $CaCO_3$ content in hardened binder determined from the TG curves.

4.5.5 X-ray Powder Diffraction on hardened magnesia binder

Compositional data on hardened binder were obtained by means of X-ray Powder Diffraction (XRPD) analyses. Data were collected using a conventional θ-θ laboratory instrument (X'Pert PRO, Panalytical, CuKα radiation) equipped with a real-time multiple strip detector (X'Celerator, Panalytical). The instrumental broadening was limited through the use of suitable slits (see section 4.3.3 for details). Samples cured for 10 and 30 days were crushed and small pieces were collected from the bulk and grinded into fine powders. The powders were sieved (80 μm mesh size) before being analyzed in order to remove lignocellular aggregates. Fine powders were mounted on glass sample holders by side-loading to avoid preferred orientation effects [162]. Semi-quantitative phase analyses were accomplished by Rietveld refinements (General Structure Analysis System [156] and its graphical interface EXPGUI [155].

Details regarding these analyses were given in our previous section 4.3.3.

4.5.6 Scanning electron microscopy of hardened concretes

After 30 days of curing, microstructural analyses by means of scanning electron microscopy (ESEM Quanta-200 instrument, FEI company) were performed on concrete samples as well as lignocellular aggregates collected from these latter. For analysis, they were mounted on aluminum stubs using carbon glue and subsequently gold-coated (Gold Sputter Coater, Emitech K550). For analysis, an accelerating voltage of 20 kV was used.

4.5.7 Compressive tests

Compressive strength (σ_{max}) was determined on 5 samples ($50 \times 50 \times 50$ mm^3) for each concrete according to European standard EN 826. In particular, tests were performed at 10, 30 and 150 days of curing for LHC and LWC concrete, while 10 and 30 days was chosen for MHC and MWC. Considering the stress-strain behavior of hemp concrete, the point at which the mechanical behavior departs from a linear stress/strain curve is considered as the ultimate strength [47] [55].

Tests were carried out by subjecting specimens to axial compressive strength in the compaction direction using an Instron 5567 electromechanical testing machine (maximum load 10 kN) at a constant displacement rate of 5 mm/min.

5 Results and discussion

5.1 Characterization of the lignocellular aggregates

5.1.1 SEM analyses

The byproducts of agro-resources have different microstructure due to the following reasons:

- Depending on the plant part used as aggregates, the structure differs. The two types of lignocellular aggregates selected for this study not only come from different plants but also from different parts of the plant (husk and stem).
- Depending on the plant growth, the cell size as well as composition differ. Additionally, the plant growth is influenced by the geographical location, climate, soil conditions and harvesting time.
- Depending on the aggregate processing, some cellular layers can be removed. For example, considering the industrial process for hemp hurd production, the defibering machine allows the separation of the shiv from the fiber. Following processing, the epidermis is usually not present on the shiv.

Figure 5-1 reports representative scanning electron microscopy (SEM) images of single aggregate particles. Both cross-sectional images as well as images taken directly on the aggregate surface (i.e. longitudinal sectional) are shown.

Figure 5-1a and Figure 5-1c highlight the highly porous network of the xylem tissue of hemp hurds. The water transportation function relies on two types of macro-pore channels of different sizes: vessel (Ve) and tracheids (Tr) [168]. The first type results from the vascular pitted bundles and is characterized by round-shaped or elliptic large pore channels with a diameter in the range 50–90 μm. The second type, having a honeycomb structure, derives from the ground tissues and surrounds the larger pores. These pore channels are polygonal or round-shaped with a diameter in the range 20–30 μm. Both types of channels are parallel and oriented along the major axis of the particle, whose thickness is about 200 μm. In addition, the presence of small pits on the inner walls of the vessel (Figure 5-1c and Figure 5-1d) leads to the formation of a connected, hierarchical pore structure. These observations are in

agreement with earlier descriptions in the literature [24] [168].

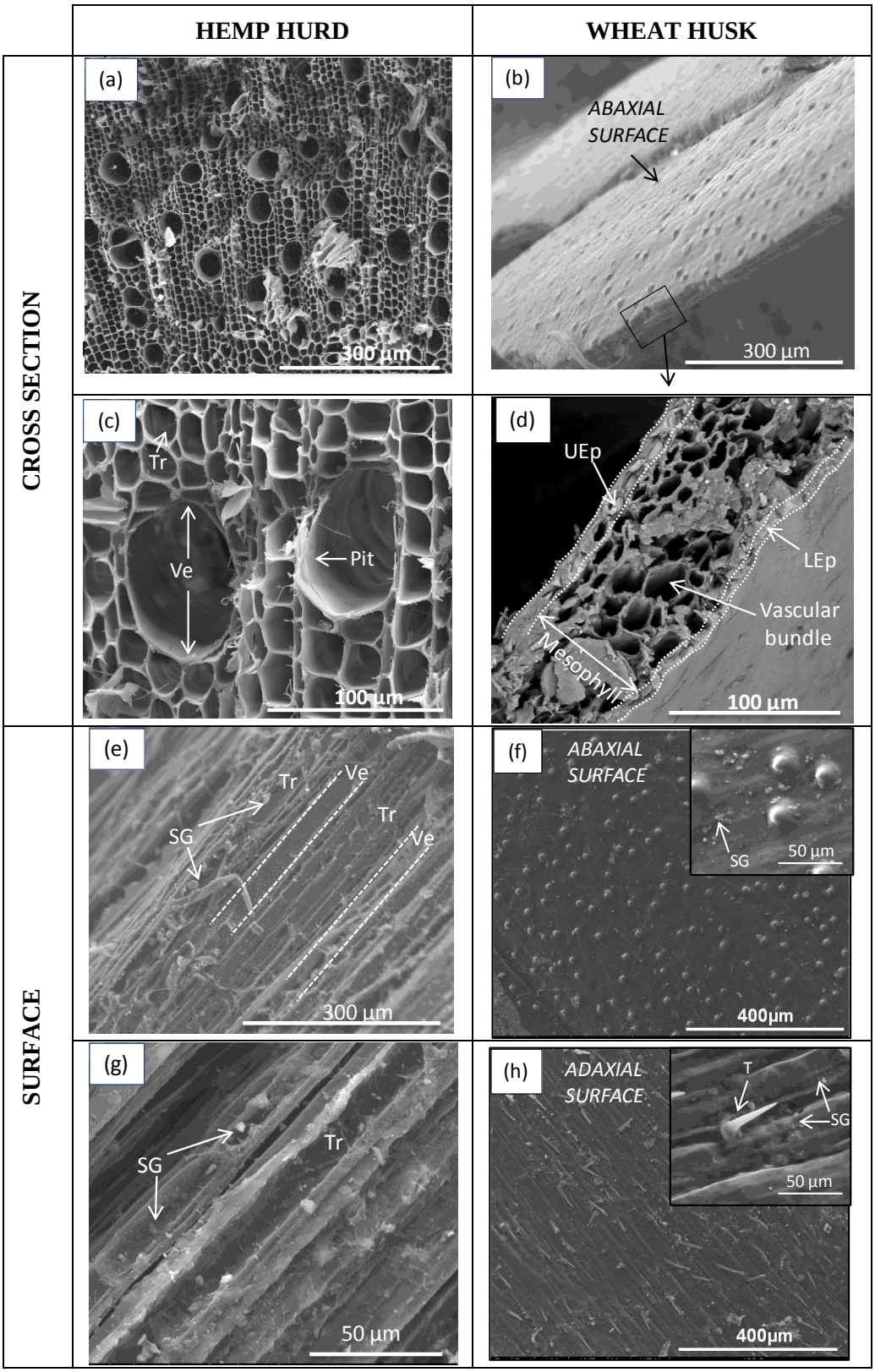

* Tr: tracheid, Ve: vessel, SG: starch granule, T: trichome, UEp: upper epidermis, LEp: lower epidermis.

Figure 5-1: SEM micrographs of: (a, c) cross section of hemp hurd, (b, d) cross section of wheat husk, (e, g) surface of hemp hurd, (f, h) surface of wheat husk.

Figure 5-1d shows a SEM micrograph of wheat husk taken with the same magnification as the one reported for hemp hurd (Figure 5-1c). The structure of a wheat husk is rather different, starting with the particles thickness which is about 90 μm for wheat husk. The internal porous structure is composed of small channels with a diameter of less than 30 μm. The porosity seems to be anisotropically distributed along the cross section of the husk. Indeed, the inner part (closed to the UEp) of the tissue shows smaller porosity compared to the area closed to the lower epidermis (LEp) where vascular bundles can be detected.

The aggregate surface morphology, especially its roughness, is an important factor which could have a great influence on aggregate-matrix adhesion. Figure 5-1e and Figure 5-1g report the longitudinal section view of a hemp hurd particle. It is characterized by channels (Tr and Ve) parallel to each other and to the growth direction of the hemp stem. Instead, the wheat husk surfaces are characterized by peculiar morphologies considering abaxial surface (outer/convex face - Figure 5-1f) and adaxial surface (inner/concave face - Figure 5-1h) of the husk. The adaxial surface has higher roughness with respect to the abaxial one and it presents a specific type of epidermis cells (aerial surface hairs) rich in silica, called trichomes (Figure 5-1h). They perform several functions, such as retaining moisture during sunny days and protecting the plant and the wheat grain from leaf-consuming vermin. The abaxial surface of wheat husk is smoother than the inner one, but it is rich in protuberances (Figure 5-1f) where silica is usually found.

5.1.2 Chemical characterization

5.1.2.1 Fourier Transform Infrared Spectroscopy (FT-IR)

The chemical composition of a plant-derived by-product is an important aspect to consider when designing bio-based concretes. Indeed, chemical interactions between lignocellulosic particles and mineral binders involve complex mechanisms which could affect performances of concretes at different stages [169]. In this study, ATR-FT-IR has been used to analyse the surface chemistry of hemp hurd and wheat husk (abaxial surface and adaxial surface). A qualitative comparison of the spectra is shown in Figure 5-2.

The review by Xu *et al.* [170], summarizes the major bands observed in the FT-IR spectra and assignments to chemical group vibrations and molecules (Table 5-1).

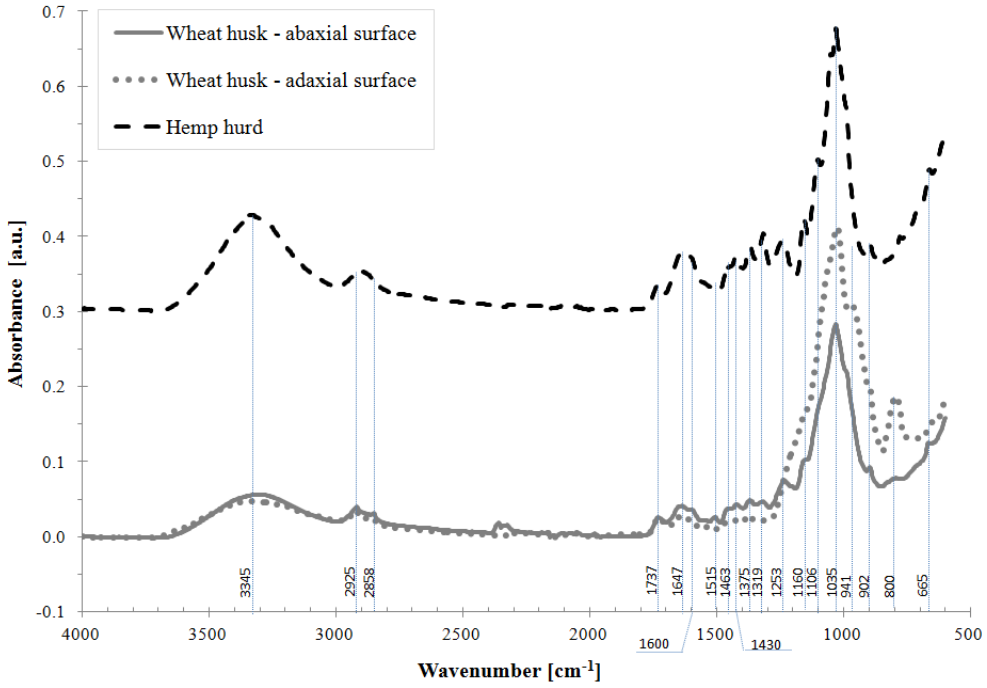

Figure 5-2: FT-IR spectra of lignocellular aggregates.

Table 5-1: Vibrations of functional groups highlighted in FT-IR spectra of wheat husk and hemp hurd.

Wavenumber (cm^{-1})	**Vibration**	**Source**
3000-3600	OH stretching	Polysaccharides
2925-2850	CH, CH_2 symmetrical stretching	Polysaccharides, waxes, fats
1730	C=O unconjugated	Hemicelluloses
1630-1650	OH bending of adsorbed water C=O stretch in conjugated ketone	Water Lignin
1600	C=C aromatic skeletal vibration	Lignin
1505-1515	C=C stretching	Lignin
1463	C=C aromatic symmetrical stretching	Lignin
1430	CH_2 symmetrical bending	Hemicellulose, lignin, pectin
1370	CH in plane bending	Cellulose, hemicellulose, lignin
1320	C-O stretching	Cellulose
1250	C-O stretching (aryl group)	Lignin, hemicelluloses
1160	C-O-C asymmetrical stretching	Cellulose, hemicellulose, lignin
1100	Si-O-Si stretching Aromatic C-H in plane deformation	Silica, lignin
1030	C-C, C-OH, C-H rings	Cellulose, hemicelluloses, lignin and pectin
941	Glycosidic bonding	Cellulose, hemicellulose
902	Glycosidic bonds symmetrical ring-stretching mode	Polysaccharides,
800	Si-C stretching	Silica, lignin
665	OH out of plane bending	Polysaccaridese

As expected, the lignocellular aggregates are characterized by the same chemical components (cellulose, hemicelluloses, lignin, pectin and waxes), but in different proportions.

In all spectra shown in Figure 5-2, the presence of polysaccharides such as hemicelluloses, cellulose, pectin and waxes are evidenced by absorption bands around 3345 cm^{-1}, 2925 cm^{-1}, 2850 cm^{-1} and 1730 cm^{-1}. In particular, the hemp hurd surface appears extremely rich in polysaccharides, with OH group stretching gives rise to an intense band in the range 3000 and 3600 cm^{-1}. The hydrophilic tendency of lignocellular aggregates is reflected in this broad absorption band since hydroxyl groups are able to form hydrogen bonds with water. Compared to hemp hurd, lower intensities were observed for the stretching vibrations of the OH group as well as the CH and CH_2 (2925 and 2850 cm^{-1}, respectively) in the spectra collected from wheat husk. Lignin shows characteristic bands around 1600 cm^{-1}, 1515 cm^{-1} and 1463 cm^{-1}. Compared to the FT-IR spectra of wheat husk, hemp hurd shows stronger intensity of these peaks which could be connected to higher amount of lignin on their surface. This observation is in good agreement with literature findings reported in Table 5-2.

Table 5-2: Chemical composition (cellulose, hemicelluloses, lignin, extractives, ash) of hemp hurd and wheat husk based on scientific literature.

Agro-resources	**Cellulose (%)**	**Hemicellulose (%)**	**Lignin (%)**	**Extractives * (%)**	**Ash (%)**	**Ref.**
Hemp hurd						
Dispersion for 12 ref.	34.5-52	9-34.5	18-28	4-10	2-4	[36]
Wheat husk						
Wheat husk, Pakistan	39	30	16	9	6	[171]
Triticum spelta hull, Germany	36	18	16	20	10	[109]
Triticum spelta husk, Germany	37.2	26	10.8	16.9	9.1	[172]
Triticum spelta hull, Germany	32.6	38.3	6.2	16.4	6.6	[173]

* The column "Extractives" refers to the water-soluble content, the sum of pectin, wax, fat and protein, or the content obtained with Soxhlet extraction.

The broad band at around 1100 cm^{-1} is assigned to aromatic C-H in plane deformation of lignin in hemp hurd in addition to Si-O-Si stretching vibration in wheat husk. In fact, wheat husk also contains silica, as confirmed by the band at 800 cm^{-1} which corresponds to stretching vibrations of Si-C bonds particularly evident on the adaxial surface (see Figure 5-2).

5.1.2.2 Van Soest method

The Van Soest method allows to quantify cellulose, hemicellulose, lignin, soluble matter (whose presence was also confirmed by FT-IR analysis, section 5.1.2.1) and ash in agro-resources' by-products. Generally, agricultural lignocellulosic biomass is comprised of about 10–25 % lignin, 20–30 % hemicellulose, and 40–50 % cellulose [174–176]. The results obtained for hemp hurd and wheat husk used in the present study are shown in Table 5-3.

According to literature, cellulose is the most abundant component in the plant cell walls, being 53 % in hemp hurd and 45 % in wheat husk. These molecules in native state are held together by intermolecular hydrogen bonds and exist as bundles of micro-fibrils composed of both crystalline and amorphous regions [174–176]. The rigid structure given by cellulose microfibrils is responsible for the mechanical strength of agro-resources. Hemicellulose, whose amount is similar in both lignocellular aggregates used in this work (around 19 %, see Table 5-3), is highly hydrophilic, easily hydrolyzed by acids and soluble in dilute alkali solutions. Hence, this component could not only influence the water absorption of the plant particle but also affect its durability as well particle-matrix bonding in composite materials based on an alkaline binder phase [177].

Lignin is a long-chain, heterogeneous polymer which acts like a glue by filling the gap between and around the cellulose and hemicellulose complexion with the polymers. As underlined by some author [178], this component protect the stem of the plant from chemical or physical aggressions, notably from most microbial attacks. The nature and the amount of lignin thus affect the durability and the biodegradability of the distinct vegetal materials. Compared to wheat husk, the higher amount of lignin in hemp hurd observed by FT-IR analysis (Figure 5-2) and confirmed by literature (see Table 5-2), was quantified by Van Soest method. In this study, as a consequence of the 2 times higher amount of lignin found in hemp hurd

instead of wheat husk, different durability of the two type of aggregates could be expected.

Additionally, particular attention have to be paid to the high amount of soluble fraction found in wheat husk (21.9 %, see Table 5-3) since, as reported in section 1.1.1.2 for lime hemp concrete, it is known from literature [179] the retardant mechanism based on Ca^{2+} fixation by pectin in high alkaline media [179]. The consequent decrease in the Ca^{2+} concentration in the binder induces a delay in the nucleation process of $Ca(OH)_2$ and C–S–H.

Table 5-3: Chemical composition of agro-resources by the Van Soest method.

Chemical composition (wt.%)	**HEMP HURD**	**WHEAT HUSK**
Cellulose	53 ± 1	45 ± 2
Hemicellulose	18 ± 1	20 ± 2
Lignin	21 ± 1	10.9 ± 0.8
Soluble fraction*	6.01 ± 0.06	21.9 ± 0.1
Ash	0.60 ± 0.03	1.11 ± 0.05

* Soluble fraction is mainly composed of pectin, protein and lipid (fat and wax) [24].

Chemical composition evaluated for hemp hurd and wheat husk in the present work (see Table 5-3), is in good agreement with literature data summarized in Table 5-2.

According to Picandet [180], who found generally higher amount of ash content in plants with high silica (SiO_2) content such as rice or wheat, the results in this study outline 2 times higher amount of ash content in wheat husk instead of hemp hurd.

5.1.3 Physical characterizations

5.1.3.1 Shape and Particle Size Distribution

Important factors to consider when designing insulating bio-based composites are the physical properties of the lignocellular aggregates. Considering that the concrete placing includes uniaxial compaction (section 4.4), the particle size distribution and shape of vegetable aggregates have a significant effect on the product characteristics in terms of granular stacking. In fact, these properties determine how the particles orient themselves and pack under applied pressure [181].

Hence, both particle size and shape was investigated for both types of lignocellular aggregates (i.e. hemp hurd and wheat husk) used in this work. Figure 5-3 outlines particle size distributions obtained by mechanical sieving.

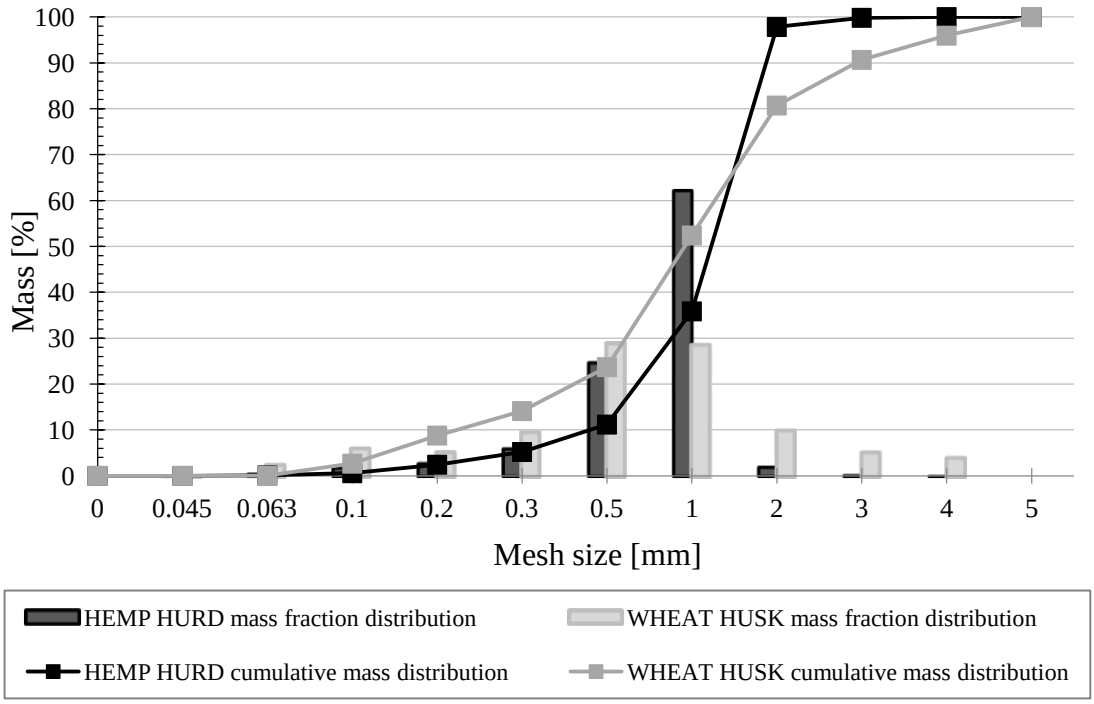

HEMP HURD FRACTIONS SELECTED

Scale: 1mm

WHEAT HUSK FRACTIONS SELECTED

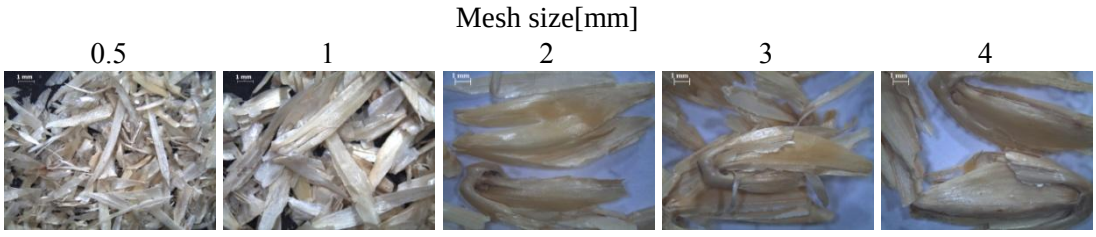

Scale: 1mm

Figure 5-3: Particle size distribution of wheat husk and hemp hurd obtained by mechanical sieving and optical microscope images of all fractions selected for this study.

As shown in the cumulative mass distribution in Figure 5-3, wheat husks are characterized by a higher amount of fine particles (less than 0.5 mm) than hemp

hurd. Only the fraction ≥ 0.5 mm was used in this study. Hence, 11 wt.% of hemp hurd particles and 24 wt.% of wheat husk particles were discarded. Many studies have shown that during mechanical sieving of hemp hurd particles (e.g. [40]), the majority of the particles orient themselves along the diagonal of the opening when they pass through the sieves, leading to separation based on their width. Indeed, these results were confirmed when examining the material retained on the sieves as the cross sectional dimensions of particles were close to the mesh size.

Considering only particles in the mesh size range 0.5 mm - 5 mm, hemp hurd has about 62 wt.% of particles retained on sieve size 1mm. If the particles are ellipsoidal, elongated or flaky-shaped, they may pass lengthways through the sieves with their width oriented along the diagonals of the square holes [40]. In this case, only particles whose width is greater than $2^{1/2}$d are retained by a sieve whose mesh size measures *d*. Taking this into consideration, 62 wt.% of the hemp hurds ranges from 1.4 mm to 2.8 mm. Differently from hemp hurd, wheat husk particles show a more homogeneous mass distribution through the mesh size from 0.5 mm to 4 mm.

As a complementary technique to mechanical sieving, image analyses were performed in order to describe in more detail the shape of the particles (see section 4.1.3.1 for experimental details). Figure 5-4 shows the size distribution of the two types of aggregates obtained from these analyses.

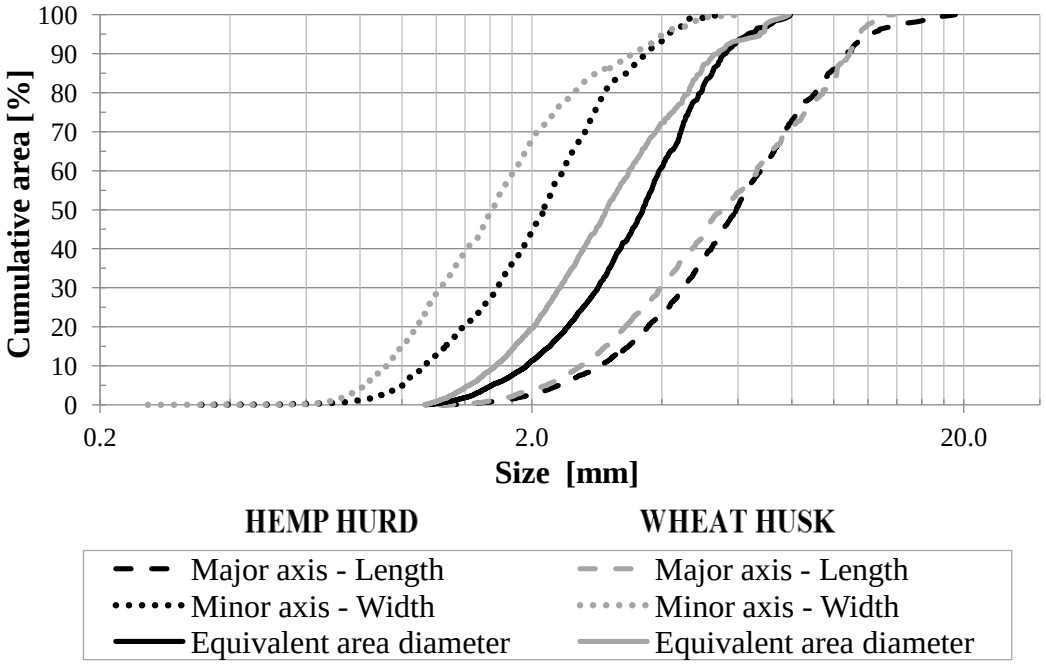

Figure 5-4: Cumulative granulometric distribution of wheat husk (grey line) and hemp hurd (black line) obtained by image analysis.

Wheat husk width ranges from 0.3 to 6.1 mm and the maximum length is about 13.8 mm. In the case of hemp hurd, the width distribution ranges from 0.3 mm to 5.6 mm and the length can reach up to 19.1 mm. Even though their similar width size ranges, considering the same cumulative area (Y axis), wheat husk particles width is smaller than hemp hurd. In addition, the length size distribution is really similar for these two types of natural particles and only about 3 % of the hemp hurd cumulative area has a length size between 13.8 mm and 19.1mm.

The higher size range of the hemp hurd length distribution (see Figure 5-3) could be justified considering particles origin. Indeed, it is known that the size of wheat husk is strongly dependent on wheat grains size. In contrast, hemp hurd aggregates come from an industrial grinding process of hemp stems which generate a more dispersed distribution.

Table 5-4 shows the geometrical characteristics for a cumulative distribution of 50 %.

Table 5-4: Geometrical characteristics for a cumulative distribution of 50 %. Median width (W_{50}), equivalent area diameter ($\Phi_{s\text{-}50}$), length (L_{50}), and elongation factor (EF_{50}).

Geometrical parameters	**Hemp hurd**	**Wheat husk**
W_{50} **(mm)**	2.13	1.62
L_{50} **(mm)**	5.94	5.50
$\Phi_{s\text{-}50}$ **(mm)**	3.61	2.98
EF_{50}	2.71	3.31

As a consequence of the granulometric distribution obtained by image analysis, the elongation factor (EF), defined here as the length to width ratio (L/W) is generally higher for wheat husk aggregates (Table 5-4, Figure 5-5).

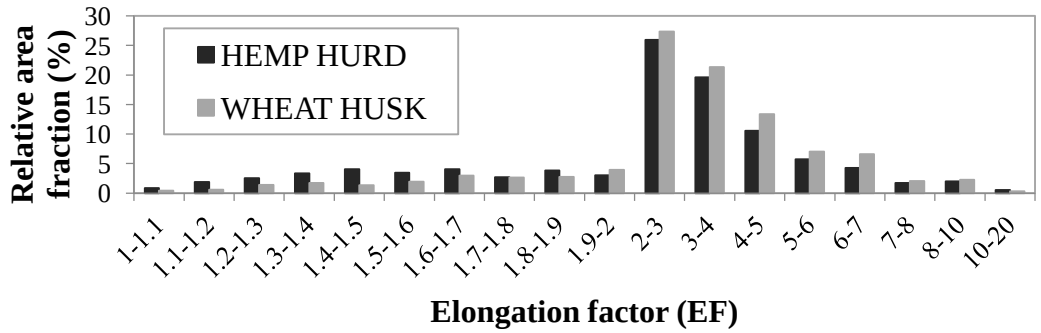

Figure 5-5: Relative area distribution as a function of Elongation factor (EF) for wheat husk (grey line) and hemp hurd (black line).

5.1.3.2 Densities and porosities

The densities of the two types of lignocellular aggregates are summarized in Table 5-5.

Table 5-5: Densities of lignocellular aggregates.

	Volumes included in definition				Density (kg/m^3)	
Density	**Solid phase**	**Open pore**	**Closed pore**	**Inter-particle voids**	**Hemp hurd**	**Wheat husk**
Loose bulk density [ρ_b]	✓	✓	✓	✓	127±1	146±2
Absolute density						
As received [ρ_{ar}]	✓		✓		1432±1	1442±2
Fine grinded [ρ_{ag}]	✓				1450±1	1507±2
Apparent particle density [ρ_p]	✓	✓	✓		208±9	319±11

Additionally, Figure 5-6 shows the volume distribution of bulk aggregates. The estimation was done considering the equations illustrated in Table 4-1.

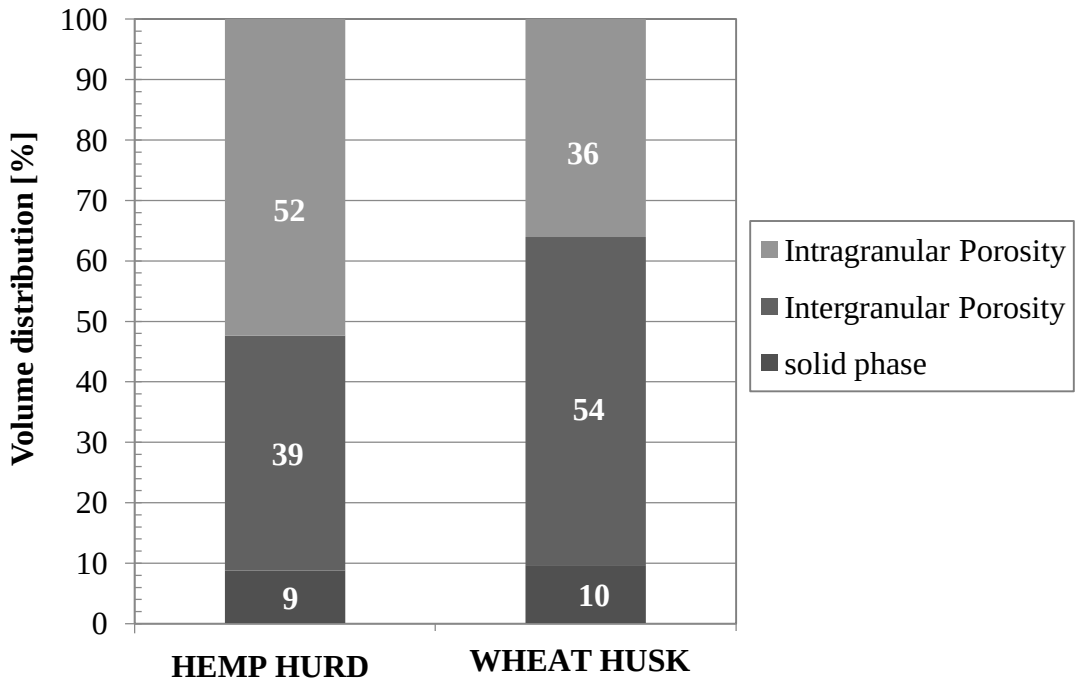

Figure 5-6: Volume distribution in bulk aggregates.

It was observed that the bulk density of wheat husk was higher than hemp hurd. The former aggregate thus requires less storage and transportation space if the same weight is considered, leading to lower handling costs.

The difference in bulk density between the two kinds of aggregate depends upon particle size, shape and absolute density. Different particle size and shape of the two types of aggregates (Figure 5-4) lead to a higher intergranular porosity for wheat husk (Figure 5-6). Nevertheless, the higher absolute density of these particles leads to higher bulk density (see Table 5-5).

The bulk density of hemp hurd is very close to values found in the literature [36]. The bulk density of wheat husk is similar to values given in the literature for rice husk, which ranges from 100-200 kg/m^3 [67]. This finding is surely linked to similarities in size and shape of the two different particles. Indeed, both rice husk and wheat husk have a boat-like shape consisting of interlocking halves with dimensions which are fully dependent on grain size.

It is well known that the porous structure of agro-aggregate are mainly open and characterized by interconnected pores [24] [168]. Indeed, the values obtained for finely grinded lignocellular aggregates and as received lignocellular aggregates are almost identical (1 % discrepancy for hemp hurd, 4 % discrepancy for wheat husk, see Table 5-5). As reported in literature [69] [168], similar values of cell wall density were observed for hemp hurd and some wood species. Stamm [182] measured the cell wall density of 10 wood species using three types of displacement media. The measured density ranged from 1.45 to 1.55 g cm^{-3}, whose findings are consistent with the value (ρ_{ag}) obtained in this study. For wheat husk, the absolute density is similar to the value given for rice husk measured with helium pycnometer [183].

The absolute density of wheat husk being higher than that of hemp hurd can be explained by the different ratio of main components in these two types of aggregate (see Table 5-3). According to the chemical composition, hemp hurd contains less ash (0.6 %) than wheat husk (1.1 %). Overall, ash are rich in inorganic compound with high atomic weight elements (Si, Mg, S, P, K and Ca) [108]. Further detail concerning correlation between chemical and physical properties of vegetal aggregates will be given in section 5.1.4.

It is interesting to observe that the estimated apparent particles density of hemp hurd (reported in Table 5-5) determined with Eq. (4. 1), gives a value which is about 10-15 % lower than literature findings [56]. This discrepancy could be connected to the

applied industrial process and defibering machine used to obtain the shivs. Indeed, the stresses undergone during the decortication process and the stress of confinement during storage in sacks could have created a variability in apparent particles density of hemp hurds coming from different providers.

Compared to a hemp particle, a single wheat husk has a density which is almost 1.5 times higher. This is closely linked to its lower intragranular porosity (36 % with respect to 52 %) as shown in Figure 5-6. These finding are in agreement with SEM micrographs presented in Figure 5-1, where hemp hurd appears to be more porous than wheat husk.

Although the hemp hurds have higher intragranular porosity than wheat husks, the bulk total porosity is similar for both types of aggregates (90 % for wheat husk and 91 % for hemp hurd). This is due to the fact that hemp hurd has a lower inter-granular porosity (39 %) than wheat husk (54 %). The different size distributions and shapes (boat-like for wheat husk and parallelepiped for hemp hurd) of the two types of aggregates surely affect particle packing and thus inter-granular porosity.

5.1.3.3 Water sorption of lignocellular aggregates

Following the recommendation of the RILEM TC 236-BBM [145], the amount of sorbed water as a function of time was fitted with the following equation (Eq.(5. 1));

$$w(t) = IRA + K_1 \cdot \log t \qquad (5.\ 1)$$

in which the Initial Rate of Absorption (*IRA*) defines the first phase (from 0 min to 1min) where water is adsorbed on the particle surface. K_1 is the slope of the curve of water content versus logarithmic time during the second phase (from 1 min to 2880 min) of water absorption involving the internal structure of the particle.

Figure 5-7 shows the sorbed water (wt.%) as function of immersion time (a) and the logarithmic immersion time (b). The fitting curves of the experimental data points (average of three samples) are displayed as discontinuous lines (hemp hurd-black line, wheat husk-grey line).

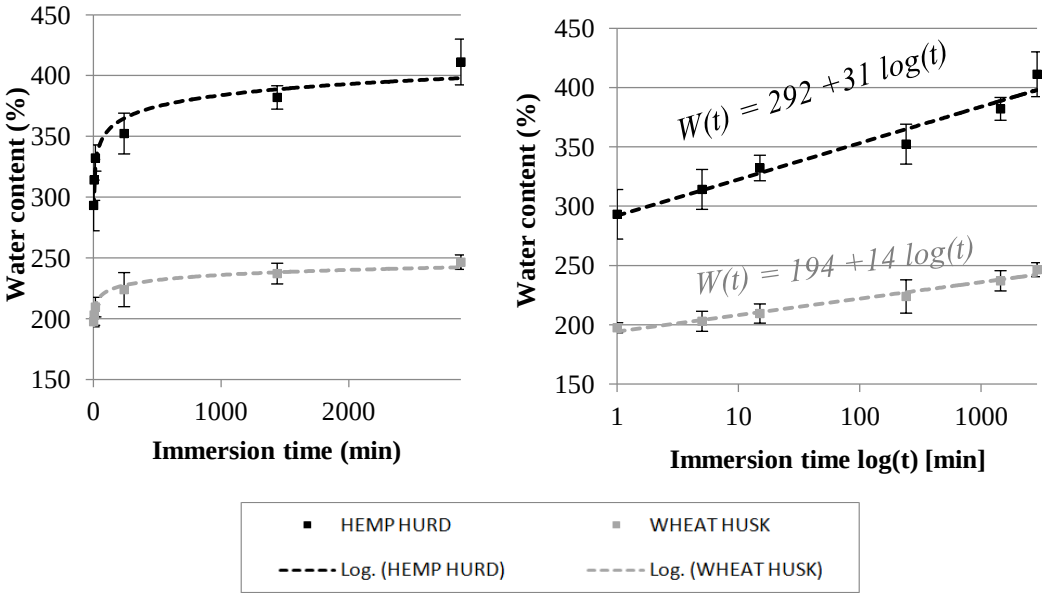

Figure 5-7: Water sorption curves versus time (a) and versus logarithmic time (b) of hemp hurd (black symbols) and wheat husk (grey symbols).

For both types of aggregate, Table 5-6 gives the average values (Av.) and standard deviations (σ) of the fitting curve coefficients (IRA and K_1) and correlation coefficients (R^2), obtained by averaging the fitting curve coefficients of the three samples.

Table 5-6: Average values (Av.) and standard deviations (σ) of fitting curve parameters (IRA, K_1) and correlation coefficients (R^2).

		HEMP HURD	**WHEAT HUSK**
IRA [%]	Av.	292	194
	σ	16	7
	CoV	5 %	4 %
K1 [%/log (min)]	Av.	31	14
	σ	1	2
	CoV	4 %	12 %
R^2	Av.	0.939	0.933
	σ	0.018	0.017

For hemp hurd aggregates, the coefficients of variation of IRA and of K1 are ≤5 % and the correlation coefficient is > 0.93 (see Table 5-6). Hence, a high confidence was obtained for this type of aggregate. For wheat husk particles, a slightly higher

discrepancy was found between experimental and fitted data for K1 (12 %) whereas both IRA and the correlation coefficient were satisfactory.

During the first wetting phase, which may be completed after 1 min of water immersion, the adsorption on the aggregate surface causes an almost instantaneous mass increase. During this phase, the water fills the open particle porosity by xylem sap canal capillarity forces [36]. A significant difference can be observed between wheat husk (IRA = 194 %) and hemp hurd (IRA = 292 %). This behavior can mainly be attributed to the higher intra-granular porosity observed for hemp hurd (Figure 5-6).

The second phase, related to water diffusion through plant cell walls openings like pits (diameter between 20 and 40 nm) [36], takes place after the first minute of immersion up to saturation (48 h). From Figure 5-7, it is evident that this second phase of water absorption follows a logarithmic law (Eq.(5. 1)). As expected, both aggregate show a lower absorption kinetic at this stage. In fact, the slope (K1) of the curve of water content versus logarithmic time is 12 %/log(min) for wheat husk and 31 %/log(min) for hemp hurd (Table 5-6). The difference in the absorption rate between the two aggregates could be justified considering the porous structures. Hemp hurd has a hierarchical pore structure, with connected pores (Figure 5-1e) whereas the pores in wheat husk are mainly observed in the transversal section (Figure 5-1d). A faster water diffusion through cell wall in hemp hurd is thus expected.

As shown in Figure 5-7 and confirmed by other researchers [36], hemp hurd sorbs more than 4 times its dry weight (W_{max}= 411±19 %) whereas the corresponding value for wheat husk is only about 2.5 (W_{max}= 246±6 %).

The fast water sorption of natural aggregates during the first minute of water sorption test is an essential aspect to consider during concrete design. Indeed, it creates a competition for water between binder and lignocellular aggregates and needs to be accounted for to assure availability of water for cement hydration. For this reasons, in this study natural aggregates were wetted prior to adding the binder. In particular, in accordance with IRA values reported in Table 5-6, The weight ratio between the prewetting water (W_p) and lignocellular aggregates was taken as 2 for wheat husk and 3 for hemp hurd.

5.1.3.4 Thermal conductivity

Figure 5-8 shows the thermal conductivity versus loose bulk density (23 °C, dry state) for hemp hurd and wheat husk investigated in the present study. For comparison, literature data for other biomass aggregates are also shown in the Figure [24]. Observing all reported data, thermal conductivity seem to increase linearly with bulk density for all type of biomass considered. Only exception (deviation from this trend) was found for wheat husk aggregates.

The low relative error (< 5 %) of data collected in this thesis work (both dry thermal conductivity and loose bulk density) assures a high confidence of the results.

Despite differences in loose bulk density observed for the two kinds of plant aggregate reported in the present study (127±1 kg/m^3 for hemp hurd and 146±2 kg/m^3 for wheat husk, Table 5-5), similar values of thermal conductivity were observed (Figure 5-8). Indeed, the observations are not statistically different, being about 0.053±0.002 W/(m·K) and 0.0497±0.0017 W/(m·K) for hemp hurd and wheat husk, respectively. These results are not surprising considering that the bulk total porosity of the two types of aggregate are similar (90 ± 1 %, Figure 5-6).

As shown in the literature [24] and outlined in Figure 5-8, thermal conductivity and bulk density of hemp shiv range from 0.053 to 0.0545 W/(m·K) and 88 to 133 kg/m^3, respectively. Hence, the values for hemp shiv found here are in good agreement with bibliography. Compared to other biomass aggregates, wheat husk shows slightly higher loose bulk density whereas the thermal conductivity is quite low, being about 0.05 W/(m·K). Considering the same native plant (wheat), the results observed here for wheat husk deviate from literature values for wheat straw (green symbols in Figure 5-8). Indeed, depending on which part of the plant is considered (husk or stalk), significantly different physical/chemical properties can be obtained.

According to the standard NF P75-101 [184], both wheat husk and hemp hurd can be considered as thermal insulators (λ < 0.065 W/(m·K)).

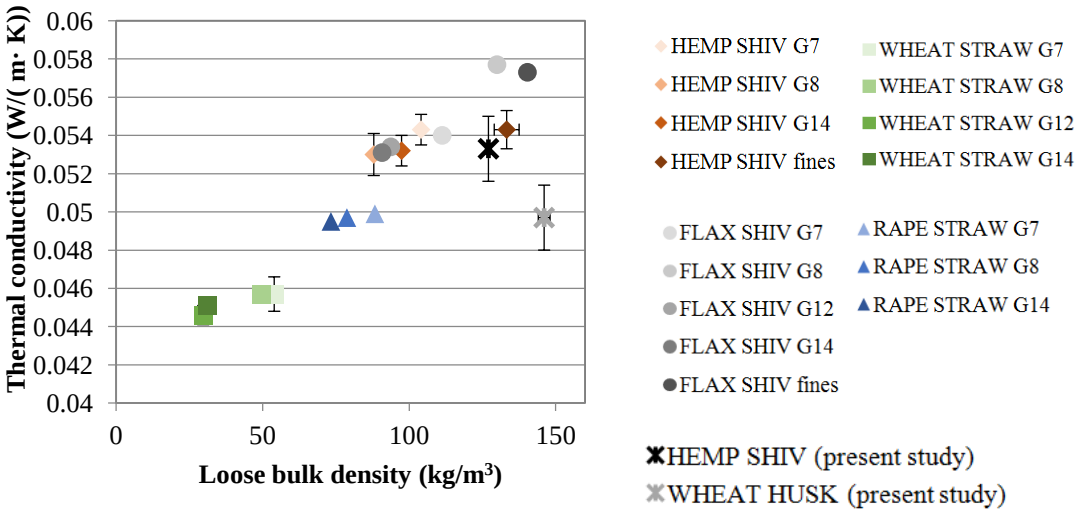

Figure 5-8: Thermal conductivity versus loose bulk density at 23 °C (dry state) for investigated hemp shiv/hurd and wheat husk (star symbols). Data from the literature [24] are also inserted for comparison.

5.1.3.5 Moisture buffer value

Regarding the moisture buffering measurements, similar results were obtained for hemp hurd and wheat husk. Figure 5-9 shows the mass variation of wheat husk together with the variation of relative humidity, while Figure 5-10 reports the moisture buffer value versus cycle number for both type of aggregates tested. The steady state is reached at cycle 2: the change in mass (i.e. Δm) and the moisture buffer value vary less than 5 % within each cycle (see Figure 5-10). Moreover, as shown in Figure 5-10 moisture buffer values in absorption and in desorption are closed.

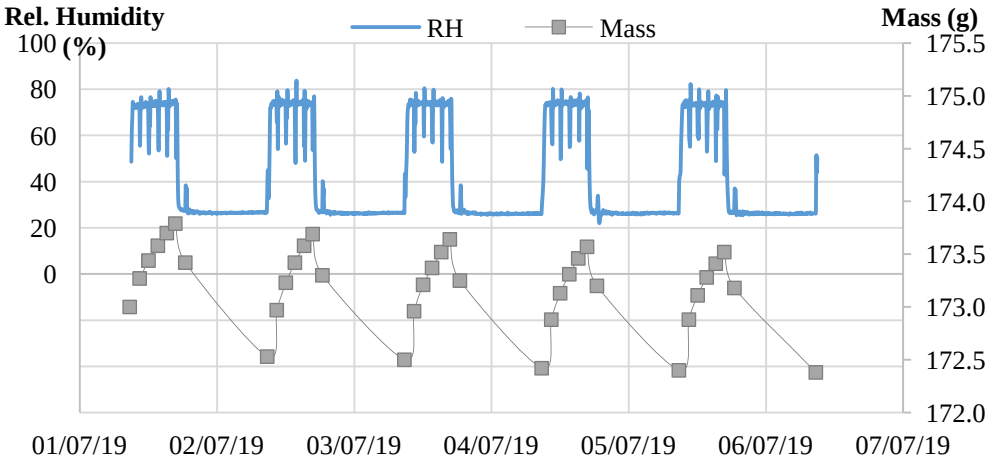

Figure 5-9: Mass of wheat husk aggregate sample and monitored relative humidity.

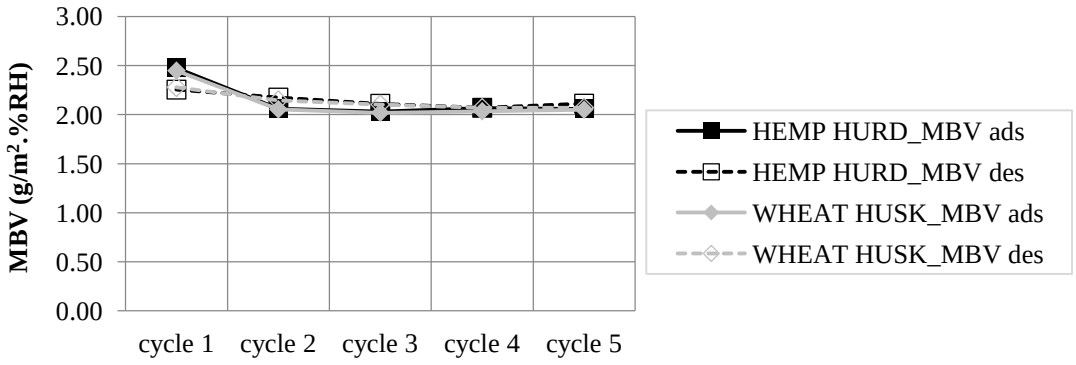

Figure 5-10: Moisture buffer value versus cycle number for hemp hurd and wheat husk aggregate.

Table 5-7 gives the moisture buffer value of hemp hurd and wheat husk as the average value of cycles 3–5 in absorption and in desorption.

Table 5-7: Average values (Av.) and standard deviations (σ) of moisture buffer value in adsorption, desorption and average for hemp hurd and wheat husk aggregates.

Aggregates		**HEMP HURD**	**WHEAT HUSK**
MBV – adsorption [g/(m^2·%RH)]	Av.	2.05	2.03
	σ	0.03	0.18
	CoV	1 %	9 %
MBV – desorption [g/(m^2·%RH)]	Av.	2.10	2.08
	σ	0.02	0.21
	CoV	1 %	10 %
MBV – average [g/(m^2·%RH)]	**Av.**	**2.07**	**2.06**
	σ	**0.02**	**0.20**

The moisture buffer values obtained for the two types of plant aggregate (see Table 5-7) are similar, being about 2.07 g/(m^2·%RH). However, slightly higher discrepancy between the experimental results was observed for wheat husk (CoV = 10 %, Table 5-7).

The moisture buffer values obtained for hemp hurd aggregate are in agreement with the results given by Viel *et al.* [24], whose experimental values were in the range 2.07-2.29 g/(m^2·%RH).

According to the classification of the NORDTEST Project (Figure 4-7), both wheat husk and hemp hurd can be considered as excellent hygric regulators (MBV >2 g/(m^2·%RH)).

5.1.4 Correlation between chemical and physical properties of biomass aggregate and implications on use in lightweight insulating concrete

Chemical composition and physical properties of agro-resources are linked. In particular, the absolute density of wheat husk being higher than that of hemp shiv (see Table 5-5) can be explained by different relative amounts of the three main components (i.e. lignin, hemicellulose and cellulose) evaluated by Van Soest method (see section 5.1.2.2). As reported in the results (Table 5-3) wheat husk contains less lignin (10.9 %) than hemp hurd (21 %) as well as a higher amount of ash (1.1 % in wheat husk vs 0.6 % in hemp hurd). The specific density of these three chemical components is slightly different. Lignin has the lowest specific density (1.26–1.41 g/cm^3) compared to cellulose (1.53–1.57 g/cm^3) and hemicelluloses (1.50–1.54 g/cm^3) [185,186]. Thus, the absolute density of wheat husk (1507 kg/m^3) is slightly higher than that of hemp hurd (1450 kg/m^3).

Another physical property which is linked to the chemical characteristics of the aggregate is the Initial Rate of Absorption (IRA, section 5.1.3.3) [24]. In particular, the amount of cellulose appears to have a positive effect on this parameter. This component provides very good stiffness and strength to plant cell walls due to its molecular arrangement in microfibrils that facilitate the formation of inter- and intra-molecular hydrogen bonds (as shown in Figure 5-11). Besides a strong inter-molecular affinity, cellulose also has a strong affinity toward water. As a consequence, intermolecular hydrogen bonds may be broken to allow new connections between cellulose chains and water molecules, leading to water bond.

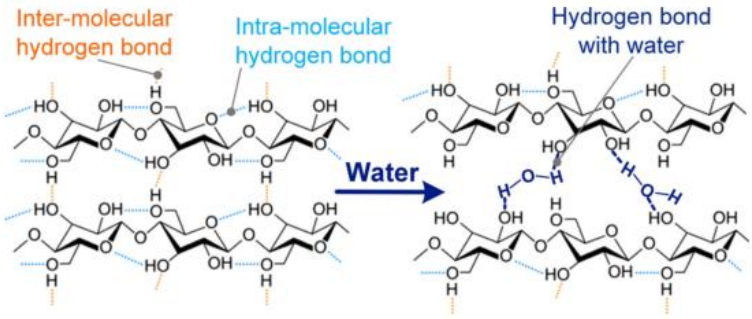

Figure 5-11: Hydrogen bonds in the cellulose with or without the presence of water.

Another important characteristic that is highly affected by the chemical composition of the plant aggregate is the binder-aggregate interaction. This is a particularly studied phenomenon in agro-concretes based on Portland cement and lime-based

binders. At early age, the components which can disturb the setting and hardening mechanisms of mineral binders are of two types: water extractives and products of the alkaline attack, generated by the cement or lime-based matrix on the plant aggregates. Among these latter, hemicellulose is identified as the most sensitive component of biomass particles. Indeed, it is hydrolyzed under slightly alkaline conditions and this reaction leads to the formation of carboxylic acids (e.g. glycolic, pyruvic, malic or o-salicylic acids) that can act as strong retarding agents for cement hydration [187]. In particular, studies concerning interactions between natural particles and lime binder outline different mechanisms;

– Trapping of calcium ions present in the binder solution by plant components. The consequent decrease in the concentration of Ca^{2+} ions induces a delay in the nucleation process of $Ca(OH)_2$ and C–S–H. This phenomenon has been observed in cement and calcium hydroxide solutions mixed with wood [188] and hemp fibers [179]. In these studies, the authors underlined the specific role of pectin which can react with Ca^{2+} ions in an alkaline environment to form a very stable "egg box" structure;

– Formation of a thin layer of adsorbed retardant molecules on the surface of cement grains [101,123,189]. This less permeable coating slows down the hydration process by preventing the migration of water to the anhydrous part of the grain;

– Poisoning of the surface of the growing $Ca(OH)_2$ and C–S–H nuclei [190,191]. During early setting, carbohydrates would increase the dissolution rate of anhydrous cement but eventually adsorb on the surface of the growing nuclei thus inhibiting their growth.

Not all aggregate-binder chemical interactions are considered as negative. For example, partial degradation of natural fibers allows cement hydration product to infiltrate the fiber and strengthen the structure [192] [193]. Indeed, the progressive mineralization of vegetal aggregate inside the concrete may improve the compressive strength of the composite even though the loss of fiber flexibility results in an overall embrittlement [193]. Fiber mineralization was studied in detail by Wei and Meyer (2015) [192] who reported an initial degradation of the amorphous components of the fibers (lignin and hemicellulose) followed by cellulose. As a result, cement hydration products could penetrate the cell walls and give rise to mineralization of the natural fiber. In another study on hemp concrete [193], the mineralization of

hemp aggregates after one year of ageing was evidenced through SEM observations. The author suggested that this phenomenon could be responsible for the continuous enhancement of compressive strength observed between 28 days and 1 year. They claimed that the progressive intrusion of cementitious phases into the hemp shives, initially being very compressible, resulted in stiffer structures.

Figure 5-12 reports the moisture buffer value versus thermal conductivity for hemp hurd and wheat husk. For comparison, the areas in the graph which represent different grades of hygrothermal performances are also shown [152] [184]. As can be observed, wheat husk and hemp hurd have similar thermal conductivity and hygric capacity and can both be classified as having excellent hygrothermal properties (see Figure 5-12). This result is highly significant and supports the possibility of substituting hemp hurd for wheat husk in agro-concrete. Indeed, this biomass residue is not only a good thermal insular [184] but also an excellent hygric regulator [152]. Hence, it could be used to produce thermal insulating products or indoor facing panels (like partition walls or ceiling).

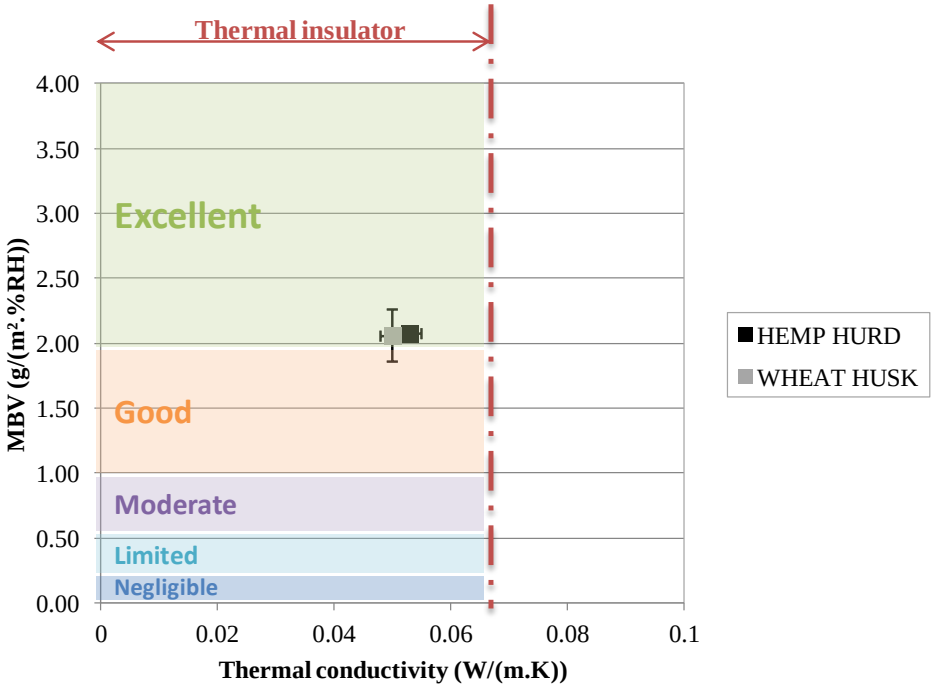

Figure 5-12: Moisture Buffer Value versus thermal conductivity.

5.2 Characterization of powder reagents (raw binding materials)

5.2.1 Commercial lime putty (CL90S PL)

The same batch of the commercial lime putty used in this thesis work was fully characterized in previous studies [153] and some of the results are displayed in Table 5-8. As can be observed from the table, it is highly pure being composed mainly of $Ca(OH)_2$ (both crystalline and amorphous) with a minor amount of $CaCO_3$ (ca. 3 %) [153]. The latter phase is likely present as a result of carbonation due to air exposure during sample handling and preparation. It is interesting to observe that the sum of calculated amount of $Ca(OH)_2$ and $CaCO_3$, based on TG data is close to 100 %, indicating that the decomposition of these two phases were the only reactions contributing to weight loss in the TG curve reported in Figure 5-13.

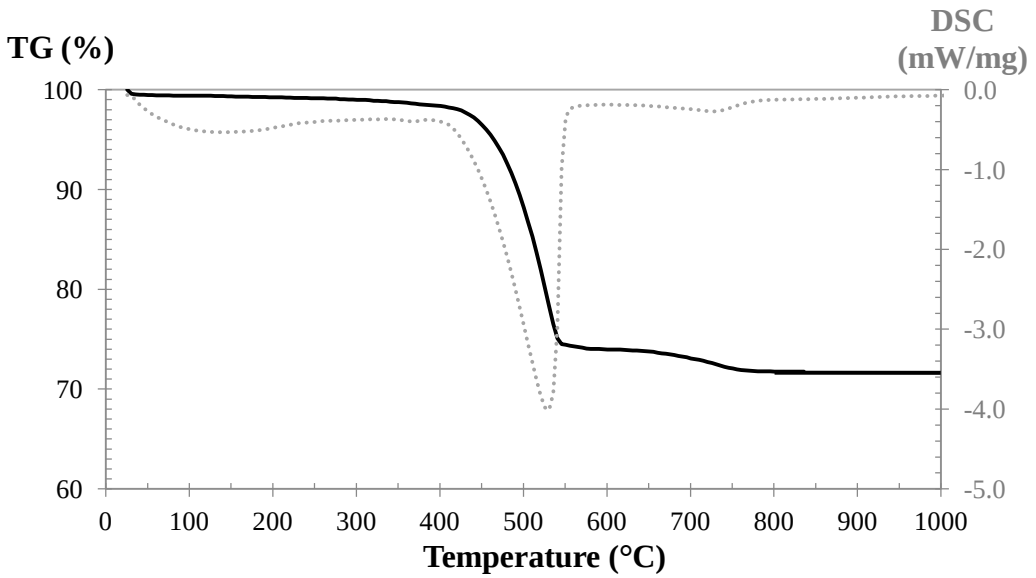

Figure 5-13: Thermal analysis curves (TG/DSC) for commercial lime putty. TG curve in black. $Ca(OH)_2$ and $CaCO_3$ were clearly identified as responsible of the weight loss in the range 400-550 °C and 600-850 °C, respectively.

The commercial putty lime used in this study was of high quality, with a guaranteed storage time of 48 months. It is known since ancient times that aging of lime putty are positive for both workability and carbonation. Indeed, the producers use the time of storage as a sort of a quality indicator. Recently, this empirical knowledge was explained by the microstructure evolution during ageing in terms of crystal size and shape [194,195]. Generally, ageing leads to an increased SSA due to a reduction in overall crystal size and a change of the crystal morphology from prismatic to plate

like [194,195]. The size and shape of the portlandite crystallites, and consequently the specific surface area (SSA) of the hydrated lime, determine the workability of the mortar in the fresh state [196] as well as carbonation and quality of the hardened building material [142]. The BET specific surface area (SSA) of the present lime putty was measured to be 10.0 ± 0.2 m^2/g. Assuming monodispersed particles and using the real density of 2.35 ± 0.01 g/cm^3 for powders obtained by air-drying lime putty at 105 °C, the SSA particle diameter (d_{SSA}) was calculated to be 0.25 µm. This result matches with TEM observations performed in Gualtieri et al.[153], where nano-sized hexagonal portlandite crystals with a platelet morphology were observed.

5.2.2 Natural hydraulic lime (NHL 3.5)

With respect to air limes, also known as fat limes/putty limes/hydrated lime and calcic limes, setting and hardening of hydraulic limes also rely on hydration reactions. The hardening process of this cementitious material involves not only reaction with atmospheric carbon dioxide, which transforms portlandite into calcite, but also with water through the hydration of several hydraulic compounds which form hydrated calcium silicates.

Figure 5-14 shows the cumulative particle-size distribution measured by laser diffraction particle size analyzer. The distribution is bimodal with D(10), D(50) and D(90) of 1.7 µm, 14.6 µm, 59.0 µm, respectively.

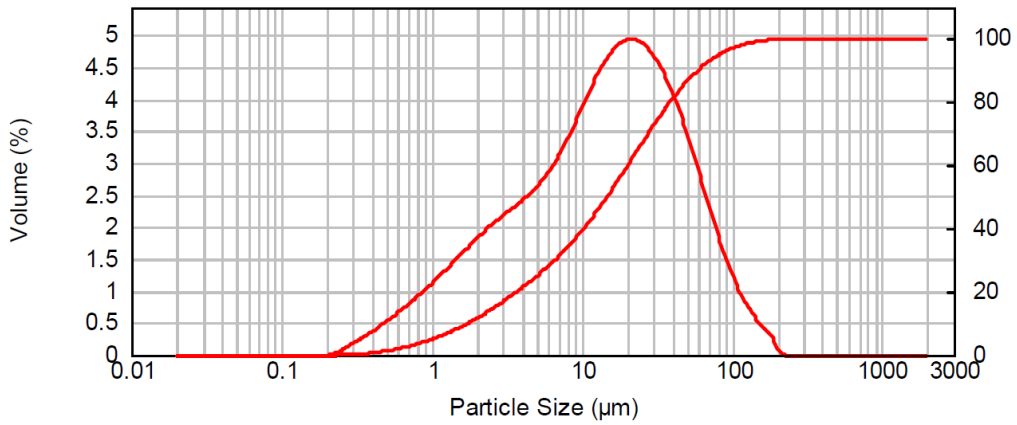

Figure 5-14: Laser diffraction results: particle size distribution of the anhydrous natural hydraulic lime powder.

The BET specific surface area (SSA) was measured to be 3.96 ± 0.04 m^2/g. Assuming monodispersed particles and using the real density of 2.56 ± 0.01 g/cm^3 for NHL powder, the SSA particle diameter (d_{SSA}) was calculated to be 0.59 µm.

Table 5-8 reports the chemical composition of the hydraulic lime used in this study. As pointed out by Boynton [197], many indexes, based on oxides composition of cement materials, have been defined to quantify their hydraulic properties. For hydraulic limes, the cementation index (CI) has been reported as (Eq. (5. 2)):

$$CI = \frac{(2.8\ \%\ SiO_2 + 1.1\ \%\ Al_2O_3 + 0.7\ \%\ Fe_2O_3)}{(\%\ CaO + 1.4\ \%\ MgO)} \qquad (5.\ 2)$$

Limes showing CI within 0.3 and 0.5 were defined weakly hydraulic, for CI values between 0.5 and 0.7 moderately hydraulic, for CI values between 0.7 and 1.1 highly hydraulic. Following these rules, the natural hydraulic lime used in this study is classified as highly hydraulic. This conclusion can is supported by the semi-quantitative phase analysis (SQPA) results reported in Table 5-8, showing a relative high content of calcium silicates (C_2S and C_3S) in addition to some C_3A (1.9 wt.%). Considering the burning temperature (around 1200 °C) for NHL production, dicalcium silicate (C_2S) should be the dominant silicate at phase equilibria (under 1250 °C). The presence of C_3S (6.4 wt.%), is probably a result of locally higher temperatures (so-called hot spots) in the kiln which lead to C_2S conversion. Additionally, as evidenced in the TG curve reported in Figure 5-15, high amount of $Ca(OH)_2$ was observed, together with $CaCO_3$.

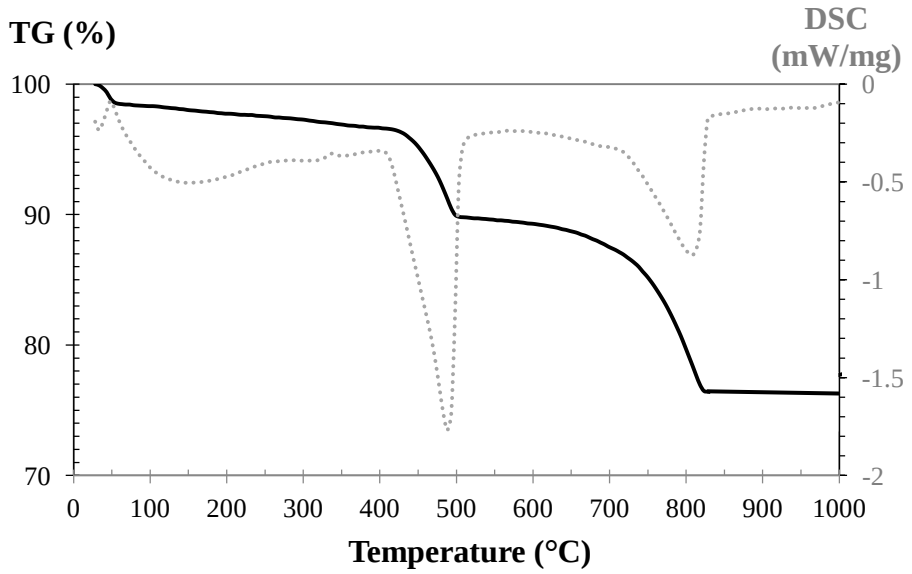

Figure 5-15: Thermal analysis curves (TG/DSC) for Natural hydraulic lime. TG curve in black. $Ca(OH)_2$ and $CaCO_3$ were clearly identified as responsible of the weight loss in the range 400-550 °C and 600-850 °C, respectively.

Data obtained by the semi-quantitative phase analysis (SQPA) in this work are qualitatively in agreement with results found by Gualtieri *et al.* [198], which

performed a full quantitative phase analyses of three commercial samples of hydraulic limes. The authors found a not negligible amount of amorphous phase in these materials (10-21 wt.%). Hence, it is likely that the quantity of each phase reported in Table 5-8 is overestimated.

5.2.3 MgO

Figure 5-16 shows the cumulative grainsize distribution measured by laser diffraction (a) and representative SEM images of the MgO powder (b). The distribution is bimodal with D(10), D(50) and D(90) of 1.3 µm, 12.4 µm, 38.8 µm, respectively (Figure 5-16a). The SEM images reveal the presence of micrometer-sized aggregates composed of nano-meter sized primary particles (Figure 5-16b).

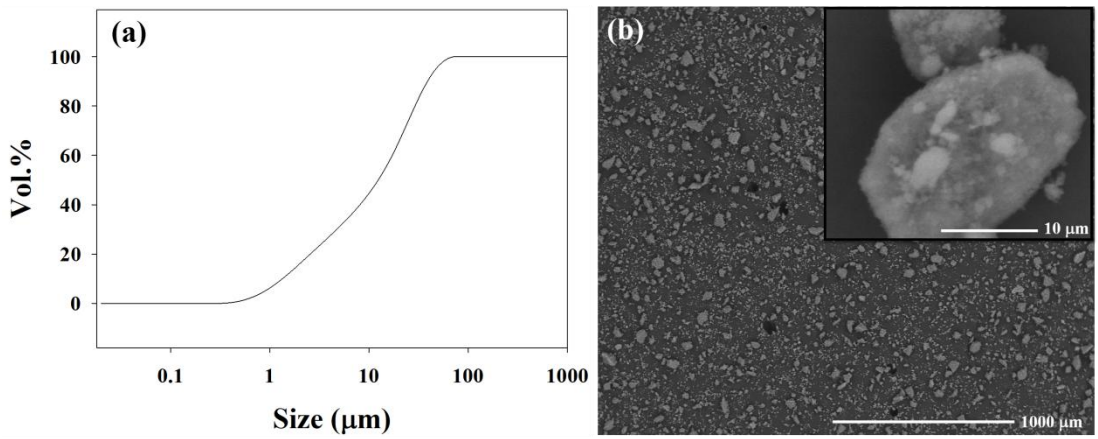

Figure 5-16: Laser diffraction results (a) and representative SEM images (b) of the MgO powder.

The BET specific surface area (SSA) was measured to be 19.8±0.2 m^2/g. Assuming monodispersed particles and using the real density of 3.269±0.002 g/cm^3 for MgO, the SSA particle diameter (d_{SSA}) was calculated to be 93 nm.

Regarding the mineralogical composition determined by XRPD and semi-quantitative analyses by Rietveld refinements (not shown here), the main constituent is MgO (periclase) as expected (92.9 ± 0.1 wt.%) followed some minor amounts of magnesium silicates (4.2±0.6 wt.% Mg_2SiO_4 (forsterite) and 1.2±0.1 $MgSiO_3$ (enstatite)), $Ca(OH)_2$ (portlandite, 1.7±0.2) and some SiO_2 (quartz, <0.5 wt.%). The presence of $Ca(OH)_2$ is due to hydration of CaO during storage. As expected, a slightly overestimation of the mineralogical composition was evidenced by comparing the chemical analyses obtained by X-ray fluorescence (reported in Table

5-8) and chemical analyses inferred from the semi-quantitative XRPD data, using stoichiometric composition of crystalline phases.

Table 5-8: Chemical and mineralogical composition of MgO powder, anhydrous nautural hydraulic lime (NHL3.5) and lime putty (CL90S PL), determinated by X-ray fluorescence (XRF) and Semi-Quantitative Phase Analyses (SQPA) using X-ray powder and the Rietveld method. For comparison, the wt.% calculated using TG data is also shown in brackets for some samples (NHL 3.5 and CL90S PL), see section 4.2 for detailes on temperature ranges for mass loss evaluation. Additionally, specific surface area (SSA) and real density are reported.

	MgO	**NHL 3.5**	**CL90S PL**
Form	Light pink powder	Grey powder	Lime putty (52 wt.% of free water)
Chemical composition (%)			
SiO_2	4.9	21.6	-
Al_2O_3	0.07	1.67	-
Fe_2O_3	0.57	0.49	-
TiO_2	-	0.16	-
CaO	3.63	56.1	73.39
MgO	88.71	0.99	0.92
Na_2O	-	0.06	0.19
K_2O	-	0.16	-
SO_3	0.05	0.45	-
MnO	0.01	0.01	-
P_2O_5	0.06	-	-
L.O.I. (loss of ignition)	2	18	25.5
[a]Phase composition (wt.%)			
C_3S	-	6.4 ± 0.2	-
C_2S	-	18.1 ± 0.3	-
C_3A	-	1.9 ± 0.2	
Calcite	-	26.2 ± 0.1 (27.2)	3.1 ± 0.1 (5.6)
$Ca(OH)_2$	1.7 ± 0.2	44.0 ± 0.1 (30)	88.0 ± 0.8 (93.2)
Quartz	< 0.5	3.4 ± 0.1	-
Brucite		-	-
Forsterite	4.2 ± 0.6	-	-
Enstatite	1.2 ± 0.1	-	-
Amorphous	n.d.[b]	n.d.	8.9 ± 0.8
SSA (m^2/g)	19.8 ± 0.2	3.96 ± 0.04	10.0 ± 0.2
Real density (g/cm^3)	3.269 ± 0.002	2.56 ± 0.01	2.35 ± 0.01

[a]Agreement factors as defined in GSAS [156]: R_{wp}: 7–11; χ^2: 1.5–4.
[b]n.d. = not determined.

5.2.4 Vegetal flour

Figure 5-17 shows a ATR-FT-IR spectrum of the vegetal flour included in composition S1 and S2. The spectrum shows characteristic absorption bands of proteins, lipids and carbohydrates.

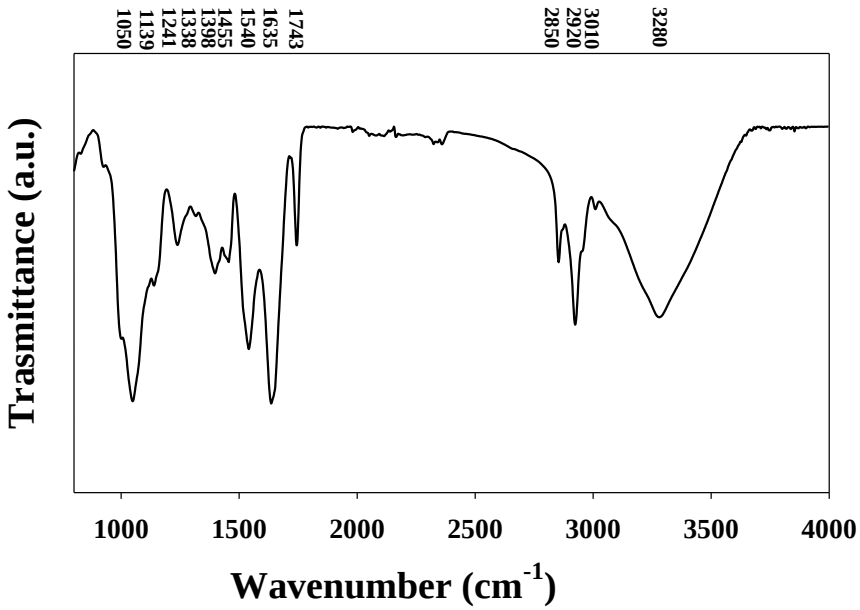

Figure 5-17: ATR-FT-IR spectrum of as-received vegetal flour.

The specific peak positions identified in the spectrum were assigned with the aid of literature data and summarized in Table 5-9 [199,200].

Table 5-9: Assignment of FT-IR absorption bands for the vegetal powder used in this work. The symbols indicate as follows: νas=assymetric stretching; νa=symmetric stretching; δas=asymmetric bending.

Absorption band (cm^{-1})	**Assignment**
3280	ν O-H-O of water ν N-H of amide
3010	ν C-H of C=CH- chains of lipids and carbohydrates
2920 -2850	ν_s CH_2 and ν_{as} CH_2 , ν_s CH_3 and ν_{as} CH_3 of fatty acids
1743	ν C=O ester functional groups from lipids and fatty acids
1635	δ N-H, ν C-N, ν C=O of amides associated with protein (Amide I) δ H-O-H of water
1540	δ N-H, ν C-N, ν C=O of amides associated with protein (Amide II)
1455	δ_{as} CH_2 and δ_{as} CH_3 of lipids, proteins and carbohydrates
1398	ν COO- of carboxylic groups of fatty acids and amino side chains
1282-1241	δ N-H, ν C-N of amides associated with protein (Amide III)
1155, 1054	ν C-O of carbohydrates

As shown in Figure 5-17, the absorption peaks in the range 3600 cm^{-1} and 3000 cm^{-1} are assigned to proteins, as are the bands around 1635 cm^{-1}, 1540 cm^{-1} and 1241 cm^{-1}. Instead, the peaks in the range 3000-1743 cm^{-1} are associated with lipids whereas those found in the range 1190-900 cm^{-1} are attributed to carbohydrates.

Figure 5-18 shows the cumulative particle-size distribution measured by laser scattering particle size analyzer (a) and representative SEM images of the vegetal flour (b,c). The distribution is bimodal with D(10), D(50) and D(90) of 2.0 μm, 37.4 μm and 147 μm, respectively (Figure 5-18a).

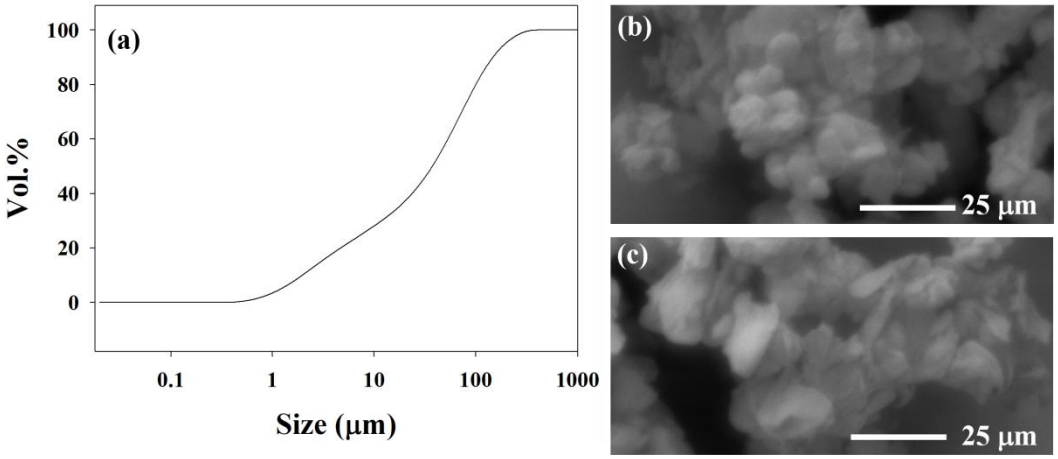

Figure 5-18: Results from physical characterization of as-received vegetal powder: (a) Particle size distribution (cumulative plot); SEM image showing aggregates composed of round-shaped (b) and flat (c) primary particles.

SEM images reveal large aggregates composed of primary particles smaller than 10 μm. Both spherical and platelet-shaped particles are observed (b and c, respectively). The BET specific surface area (SSA) was 0.70 ± 0.01 m^2/g and the real density was 1.2736 ± 0.0004 g/cm^3. From these data, the SSA particle diameter (d_{SSA}) was calculated to be 6.7 μm. Despite the assumption of monomodal distribution (monodispersed particles distribution) in these calculations, the obtained value is in rather good agreement with SEM images showing micrometer-sized primary particles.

Considering that the laser scattering diffraction analysis was made with water as carrier fluid, larger particles are expected with respect to the dry state. In fact, water absorption experiments (see experimental method in section 4.2) showed that the flour absorbs 17.6 wt.% of water and that water saturation is obtained already

following 2 min. Hence, initial particle swelling is surely expected and the laser diffraction results should reflect the size distribution of the particles embedded in the cement matrix.

5.3 Study of the magnesium oxysulfate cement modified by macromolecules

In this chapter, the main results concerning the effect of a vegetal flour (composed of proteins, carbohydrates and lipids) and $MgSO_4$ on the hydration kinetics of MgO are reported together with the microstructural properties following completed reactions. Important knowledge for designing lightweight concrete composition based on so-called basic magnesium sulfate cements (i.e. modified MOS cements) are acquired in order to select suitable processing routes for the manufacturing of insulation boards.

5.3.1 Hydration kinetics

5.3.1.1 Semi-adiabatic tests

Semi-adiabatic hydration experiments were performed in order to simulate the situation of the cement in the centre of a large pour. Considering the highly exothermic nature of the hydration reaction, the heat of hydration may cause exponential temperature rise if the heat exchange process is slow. Figure 5-19 shows the temperature as a function of time of the investigated compositions.

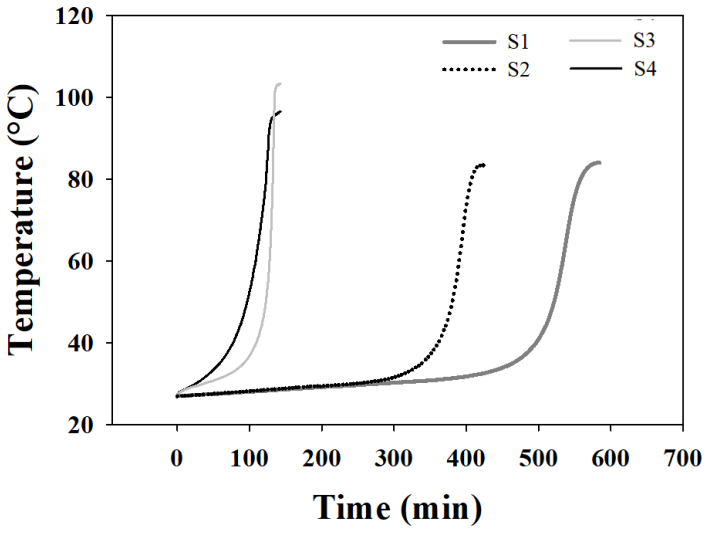

Figure 5-19: Temperature as a function of time starting from the preparation of the fresh paste.

Let us first consider pastes without vegetal flour, with and without the presence of $MgSO_4$ (i.e. S3 and S4, respectively). The start of the acceleration stage and the corresponding temperature (from 1st derivative curves) for composition S4 are 45 ± 5 min and 32.6 ± 0.8 °C, respectively. A considerably longer pre-acceleration period is observed for sample S3 (88 ± 3 min), although the temperature at the start of temperature rise is similar (i.e. 34.3 ± 0.4 min).

Once started, a faster hydration is observed for composition S3 leading to convergence of the two curves following 134 min. It thus appears that $MgSO_4$ acts as retarder of the hydration reaction.

The addition of vegetal flour increases the pre-acceleration period, in particular when added together with $MgSO_4$. In fact, composition S1 which contains both vegetal flour and $MgSO_4$ shows accelerated heating following 440 ± 20 min whereas the corresponding value for composition S2 (only vegetal fluor) is 270 ± 15 min. The temperatures at which accelerated temperature rise is observed is somewhat lower for composition S2 compared to composition S1 (30.5 ± 0.4 vrs. 33.4 ± 0.9 min).

Thus, it can be concluded that both $MgSO_4$ and vegetal flour increases the pre-acceleration period, being longest when both are present. The large differences in relative concentration of MgO between samples prepared with and without vegetal flour (ca 38 and 56 wt.%, respectively) could contribute to slow down the initial temperature rice and thus start of accelerated hydration.

5.3.1.2 Isothermal tests at 35 °C

The semi-adiabatic tests presented in previous section underlined important differences in the duration of the pre-acceleration period when vegetal flour was included in the composition. A small retardant effect was also observed for $MgSO_4$.

In order to better elucidate the role played by $MgSO_4$ and vegetal flour on the initial hydration of MgO, isothermal experiments at 35 °C (slightly higher than that at which accelerated hydration was observed), see Figure 5-19 were performed and the degree of reaction (i.e. conversion factor) was evaluated using XRPD data. The only hydration product identified was $Mg(OH)_2$, as will be further discussed in the next paragraph (5.3.1.3). Figure 5-20 shows the conversion factor (α) for MgO and $Mg(OH)_2$ as a function of time for compositions S3 (a) and S1 (b). For clarity, composition S3 contains only MgO and a $MgSO_4$ solution whereas composition S1 also contains vegetal flour.

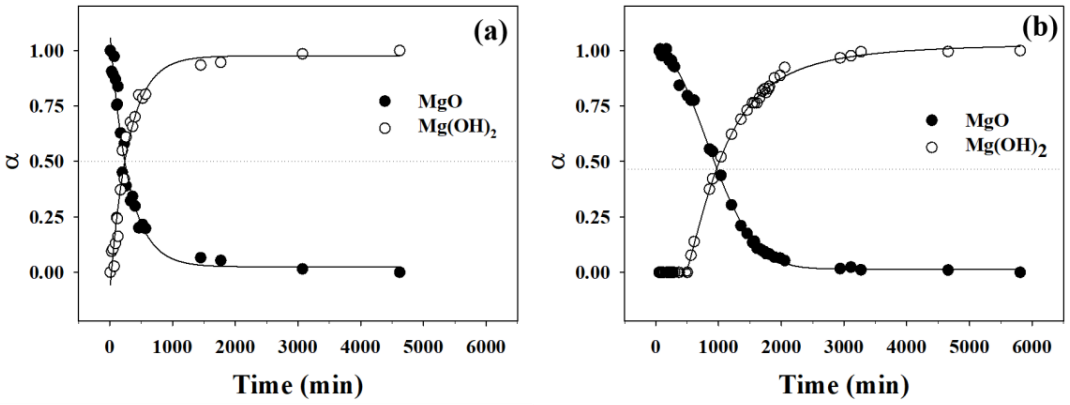

Figure 5-20: Conversion factor for MgO and $Mg(OH)_2$ as a function of curing time under isothermal conditions: (a) Sample S3, with $MgSO_4$ but without vegetal flour; (b) Sample S1, with both $MgSO_4$ and vegetal flour.

In the absence of vegetal flour, the dissolution of MgO and the crystallization of $Mg(OH)_2$ starts immediately and the curves are highly symmetric, indicating a direct correlation between MgO dissolution and $Mg(OH)_2$ crystallization without intermediate phases (see Figure 5-20a). In the presence of vegetal flour, the MgO starts to dissolve following 170 min of curing and the crystallization of $Mg(OH)_2$ is even more delayed (following 500 min). The conversion factor (α) for $Mg(OH)_2$ crystallization is lower than the conversion factor for MgO dissolution up to about a factor of 0.95 reached following 2060 min, indicating an intermediate amorphous phase.

Hence, it can be concluded that the vegetal flour functions as a retarder of both MgO dissolution and subsequent $Mg(OH)_2$ crystallization and that this effect is time dependent. In fact, curing at a temperature above that for which accelerated hydration (i.e. temperature rise) was observed in semi-adiabatic experiments (Figure 5-19) did not eliminate the induction period of the reactions although it became shorter.

5.3.1.3 Isothermal tests at 20 °C

In order to investigate the temperature sensibility of the phase composition, isothermal tests at 20 °C were performed for compositions S1 and S3. XRPD patterns were collected following 7 days of curing and semi-quantitative phase analyses were performed by the Rietveld method. Figure 5-21 shows the outputs of the refinements, whereas Table 5-10 shows the semi-quantitative results.

As can be observed from, the 517 MOS phase is only formed in the composition containing vegetal flour, underlining its importance in the chemical equilibrium of the cement.

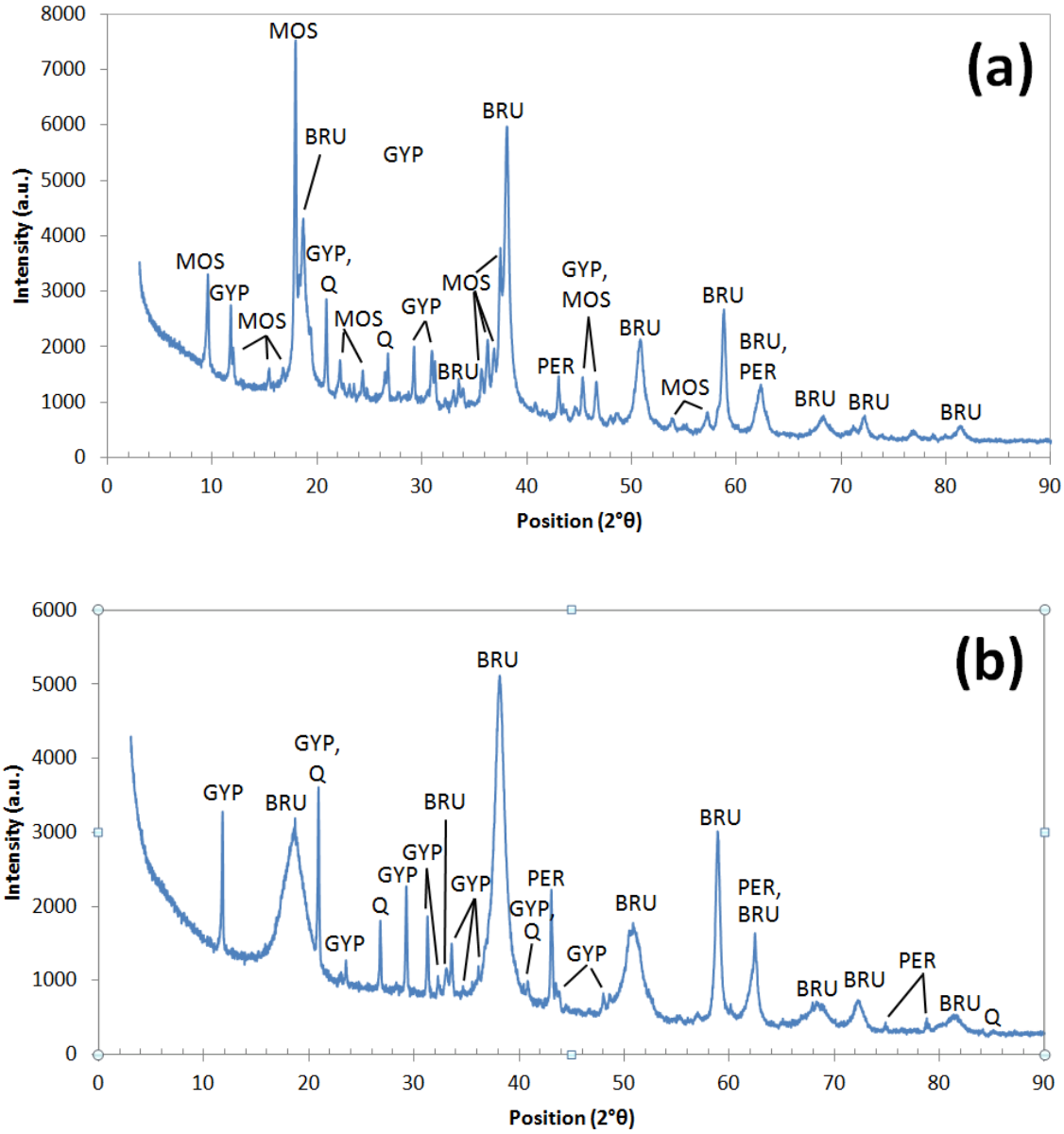

Figure 5-21: The Rietveld refinement output of composition S1 (a) and S3 (b) cured for 7 days under isothermal conditions at 20 °C.
Q= quartz (SiO_2); MOS= Magnesium oxysulfates ($5Mg(OH)_2 \bullet MgSO_4 \bullet 7H_2O$, 517 phase); PER= Periclase (MgO); BRU= Brucite ($Mg(OH)_2$); GYP= Gypsum ($CaSO_4 \cdot 2H_2O$).

The phase development in sample S1 under the first week of curing was followed as a function of time and the XRPD results are shown in Figure 5-22. More specifically, (a) shows the entire collected 2θ range for each curing time (indicated in the figure)

where the highlighted zones correspond to limited 2θ ranges that are shown in (b) and (c). Considering Figure 5-22b, the (200) peak of MOS 517 increases as a function of curing time up to 44 h after which no further changes in intensity are observed. Instead, $Mg(OH)_2$ starts to crystallize after 44 h and continuous up to about 122 h (Figure 5-22b). It can thus conclude that the two crystallization reactions are not occurring simultaneously. In Figure 5-22b, it can be observed the successive reduction of the peak intensity of MgO which is consumed by both reactions.

Table 5-10: Results from semi-quantative phase analyses (XRPD and Rietveld refinements) of composition 1 and 3 cured for 7 days at a constant temperature of 20 °C. As can be observed, MOS is only crystallized in the composition containing vegetal flour (S3).

	$Mg(OH)_2$	**517 MOS**	**MgO**	**$CaSO_4 \cdot 2H_2O$**	**Quartz**
S1 (20°C, 7 days)	57.3 (1)	33.7 (1)	2.5 (1)	4.9 (1)	1.6 (1)
S3 (20°C, 7 days)	88.2 (1)	-	4.3 (1)	6.2 (1)	1.3 (1)

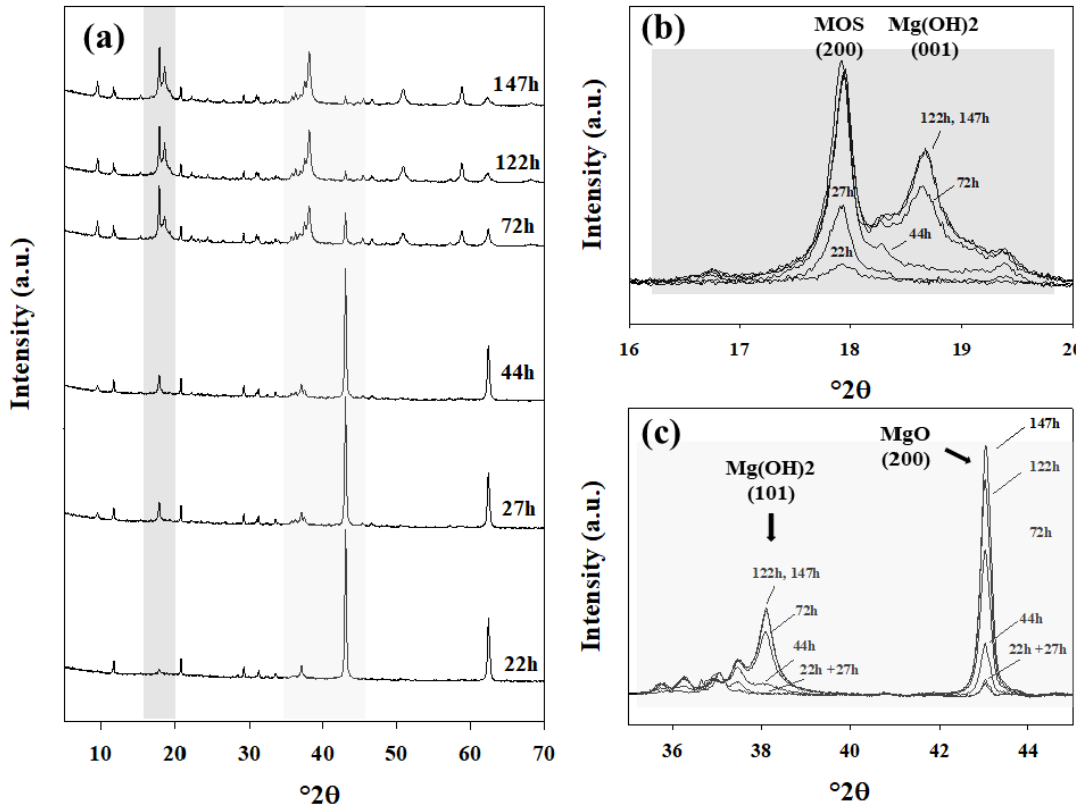

Figure 5-22: XRPD data collected from specimens of sample S1 following different times of curing of the fresh paste is shown in (a). Limited 2θ ranges evidencing the changes in intensity of specific peaks belonging to the various crystalline phases are also shown: (a) MOS 517 (200) and $Mg(OH)_2$ (001); (b) $Mg(OH)_2$ (101) and MgO (200).

5.3.2 ζ-potential of $Mg(OH)_2$

As shown in Figure 5-23, the ζ -potential distribution of $Mg(OH)_2$ equilibrated in distilled water contained one single peak centred at 33.1 mV with a peak width of 5.8 mV. Instead, a bimodal distribution was observed in a dilute $MgSO_4$ solution with the major peak (92.4 area%) at 4.2 (width of 8.9 mV) with a smaller peak (7.6 area%) at -19.5 mV (width of 4.4 mV).

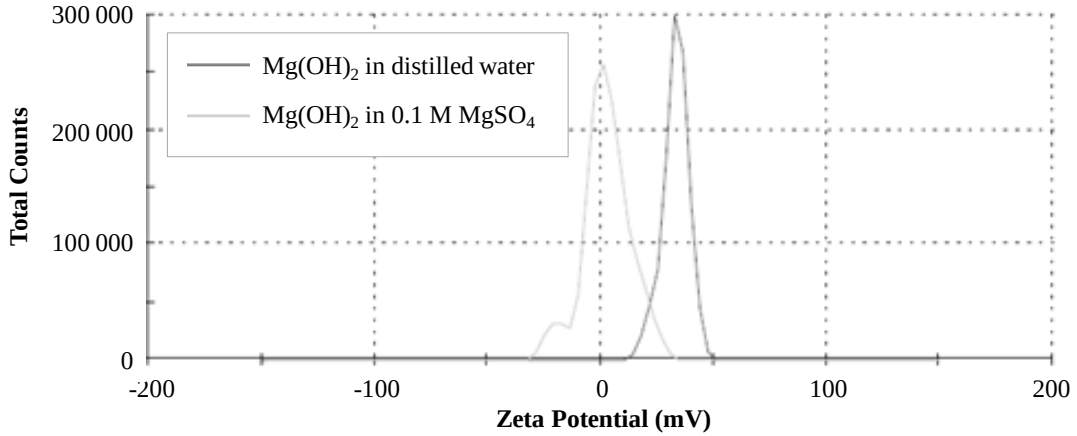

Figure 5-23: ζ -potential distribution of $Mg(OH)_2$ in distilled water (black line) and $Mg(OH)_2$ in a dilute $MgSO_4$ solution (grey line).

5.3.3 Characterizations of hardened binders

5.3.3.1 SEM observations

Figure 5-24 shows SEM images and EDS analyses of sample S1 from various different zones observable in a freshly exposed surface of the bulk. This sample, for which hydration was performed in the presence of both $MgSO_4$ and vegetal flour, shows a porous structure with ca. 80 % of the pores, measurable at a magnification of 100 (>ca. 20 µm), being smaller than 100 µm in diameter (see Figure 5-24a). The pores are spherical and some residual organic matter may be observed (se arrow in Figure 5-24b). The matrix is composed of dense zones with nano-sized granules apparently lined by interlocking platelets (Figure 5-24d and e). Likewise, the pore lining is composed of interlocking platelet crystals, often covered with a transparent film made up of organic matter (Figure 5-24f). The dense zones are probably the result of hydration within porous MgO aggregates where the availability of SO_4^{2-} ions is limited by diffusion, whereas the open network of large platelets is the result of crystallization and growth in the supersaturated solution. In fact, the dense zones

are microstructurally similar to the product of hydration in pure water as will be discussed below (sample S4). The well-defined crystalline films covering the pore walls, suggest heterogeneous crystallization of $Mg(OH)_2$ on the interface between the grain and the matrix, followed by crystal growth and slow dissolution of the organic material.

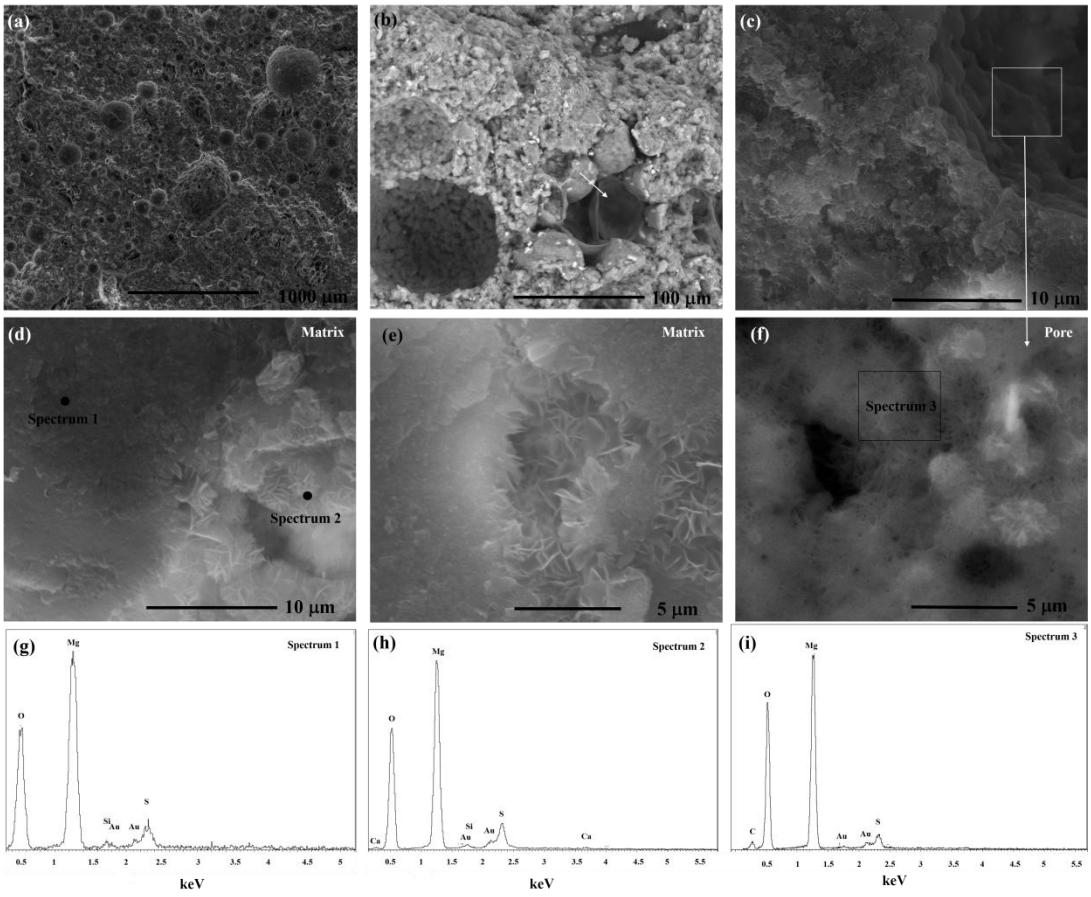

Figure 5-24: SEM-EDS analyses results of sample S1 (hydration in the presence of both $MgSO_4$ and vegetal flour). The images show a porous structure (a,b). The matrix surrounding the pores are composed of dense and granular zones as well as zones with high concentrations of platelet $Mg(OH)_2$ crystals (d, e) Both zones contain sulfur (g, h). The pores are lined with platelet crystals, often covered with a transparent film of organic matter (f, i).

Figure 5-25 shows SEM images of sample S2 (hydration in only water and vegetal flour). The binder is porous (a) and the solid phase is composed of loosely packed nanoparticles (b). The extreme fragility of the sample made it difficult even to prepare specimens for SEM investigations. Opposed to images collected for sample S1 (Figure 5-24), no large platelet crystals were observed.

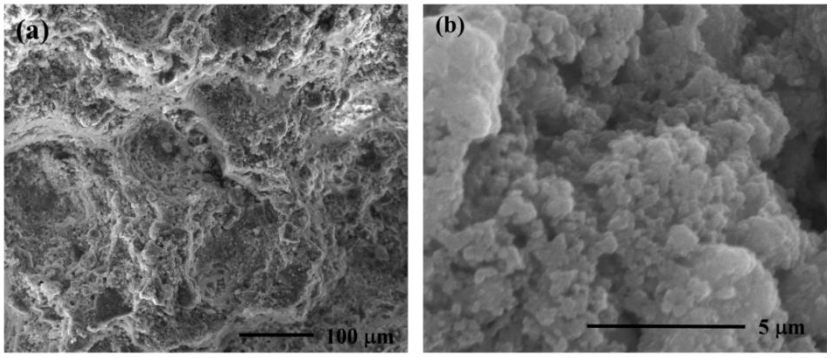

Figure 5-25: SEM images of sample S2 (hydration in the absence of $MgSO_4$ but in the presence of vegetal flour), showing a porous structure (a) composed of a granular nano-phase (b).

Figure 5-26 shows SEM-EDS analyses of sample S3, hydrated in the presence of $MgSO_4$ without addition of vegetal flour. The sample is surely less porous with respect to sample S1 which also contained vegetal flour (compare with Figure 5-24). The solid material is composed of loosely packed interlocking platelet crystals as well as larger dense grains (arrow in Figure 5-26a). These grains are completely covered with a dense film of platelets (Figure 5-26b, c).

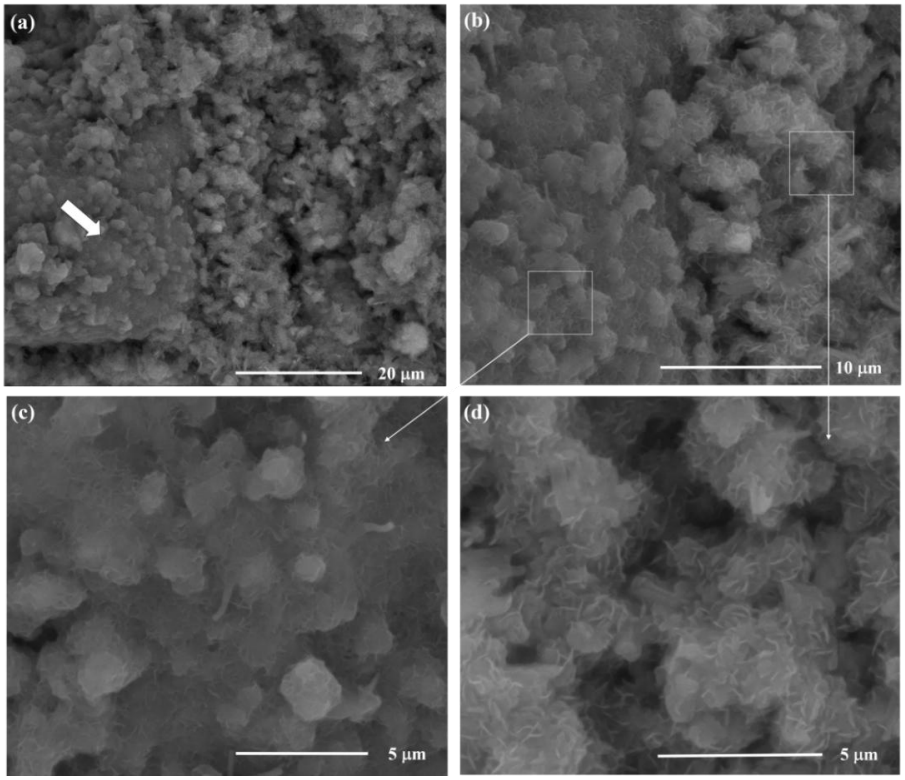

Figure 5-26: SEM analyses results of sample S3 (hydration in the presence $MgSO_4$ withou addition of vegetal flour). The structure is rather dense and apparently composed of large grains (a, b) covered with highly interlocking platelet crystals (c), embedded in a rather open matrix mainly composed of interlocking platelet crystals (d). Zones with particles more spherical in shape were also observed in the matrix (not shown).

Figure 5-27 shows a SEM image of sample S4, obtained by hydration of MgO in pure water. It should be pointed out that this experiment did not result in a consolidated sample but a suspension from which the solid particles were extracted. The morphology is very similar to sample S2, being nanophasic (compare with Figure 5-25).

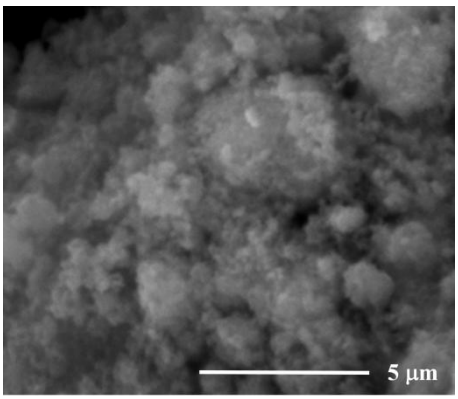

Figure 5-27: SEM image of sample S4, showing a granular material composed of nanoparticles.

Summarizing, hydration in the presence of $MgSO_4$ resulted in a heterogeneous microstructure composed of a rather open network of large platelet crystals surrounding dense grains covered by platelet $Mg(OH)_2$ crystals. The dense zones are probably the result of hydration within porous MgO aggregates, whereas the open network of large platelets is the result of crystallization and growth in the supersaturated solution. The vegetal flour provoked the formation of a porous network, being mechanically resistant only when hydration was performed in the presence of $MgSO_4$. In this case, highly interlocking micrometer-sized platelet crystals were formed not only in the matrix but also around the pores templated by the vegetal flour. In fact, SEM images show well-defined crystal pore linings suggesting heterogeneous crystallization of $Mg(OH)_2$ on the interface between the grain and the matrix, followed by crystal growth and slow dissolution of the organic material.

5.3.4 TEM observations

Figure 5-28 shows bright-field TEM images of sample S3. The $Mg(OH)_2$ crystals are thin platelets, a property clearly evident in (a-b). Darker stripes are visible in (a) and interpreted as particles oriented with the basal plane parallel to the view, and thus represent the thickness of the platelets. Elongated crystal aggregates are also present (b) and assigned to calcium sulfate hydrate with the aid of elemental maps (see Figure 5-29). It is interesting to observe that the $Mg(OH)_2$ platelets are covered with amorphous material, particularly evident in (c) and (d) where the latter evidences the crystal planes partly covered by amorphous material appearing as dark areas.

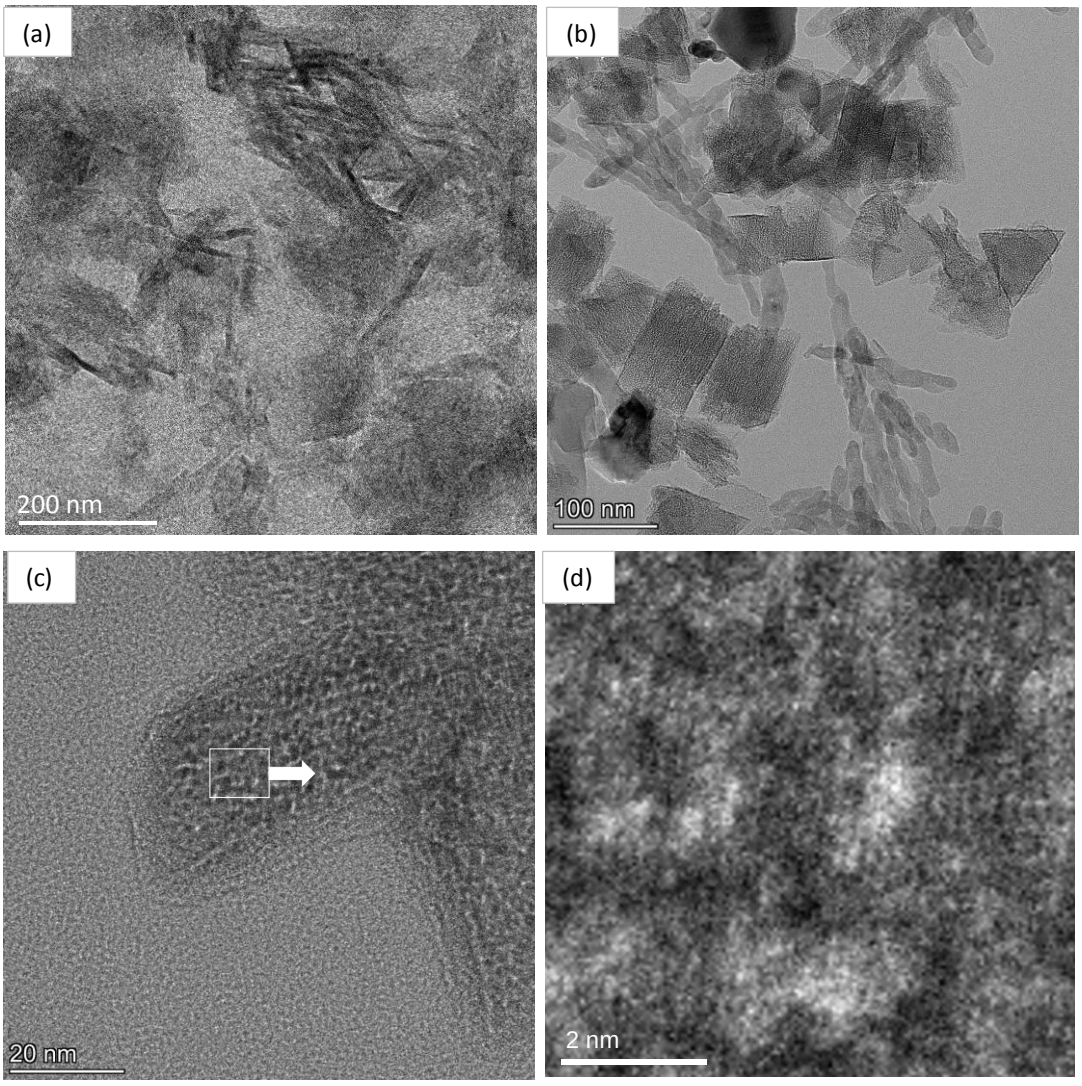

Figure 5-28: Bright-field TEM images of sample S1. The platelet morphology of the hexagona $Mg(OH)_2$ crystals are clearly evident (a, b). The crystals are covered with amorphous material, particularly evident in (c) and (d) where the latter evidences the crystal planes partly covered by amorphous material appearing as dark areas. The presence of elongated aggregates of calcium sulfate hydrate crystals are evident in (b) (see Figure 5-29).

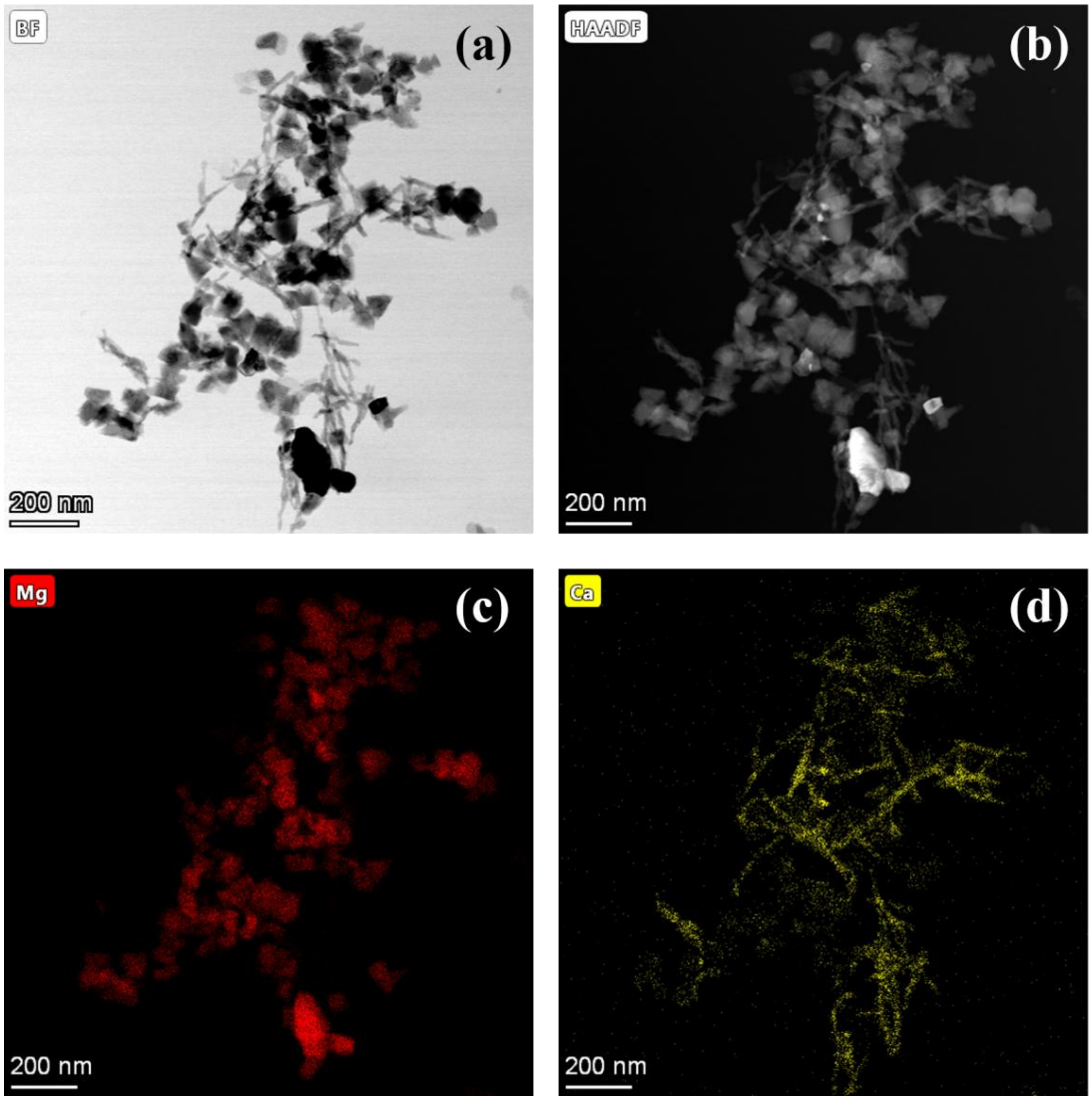

Figure 5-29: Bright-field STEM image (a) and corresponding STEM-HAADF image (giving Z-contrast) as well as elemental maps of Mg (c) and Ca (d) showing that the elongated crystal aggregates are Calcium sulfphate hydrate (as identified by X-ray powder diffraction). In addition, a large grain of residual MgO is also evident (high contrast in STEM-HAADF image in b).

Figure 5-30 shows bright-field TEM images of sample S4. The platelet crystal habit of $Mg(OH)_2$, already observed for sample S3 in Figure 5-24, is confirmed. Darker stripes are visible in the upper part of Figure 5-30 (b), further confirming the anisotropic crystal size. Opposed to sample S3, no clearly visible amorphous layer is present on the crystals.

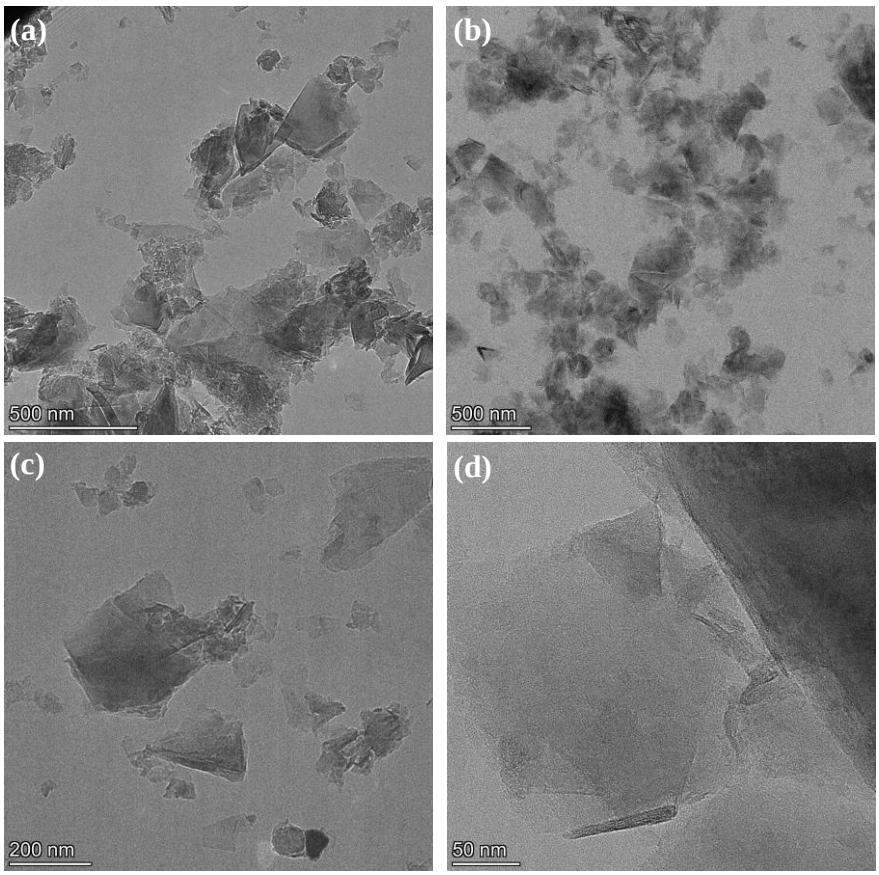

Figure 5-30: Bright-field TEM images of sample 4, showing a platelet crystal habit of $Mg(OH)_2$. The dark stripes observable in (b) as well as in (d) are assigned to crystals oriented with their basal plane parallel to the view (i.e. platelet thickness).

5.3.5 XRPD

Figure 5-31a shows XRPD patterns collected from the cement samples (S1-S4, see section 4.3.1) at ca. 28 days following preparation. The samples contain $Mg(OH)_2$ as major phase in addition to some residual MgO and $CaSO_4 \cdot 2H_2O$, the latter present in samples hydrated in the presence of $MgSO_4$ solution (i.e. S1 and S3). Full quantitative phase analyses were performed for sample S3, and the following composition was obtained: 64.0 (5) wt.% $Mg(OH)_2$; 3.4(1) wt.% MgO; 2.5(1) wt.% Mg_2SiO_4; <1 wt.%; 1.7 (1) $CaSO_4 \cdot 2H_2O$; 27.8 (5) wt.% amorphous material. The rather high amount of amorphous material present in the sample is assigned to SO_4^{2-} not bound in a crystal lattice.

There is an important difference in the peak width of $Mg(OH)_2$ in the absence and presence of $MgSO_4$. Figure 5-31b shows the FWHM of peaks corresponding to specific lattice planes in the brucite-type structure. Data for each sample are reported.

Although no microstructural data can be withdrawn from these analyses as the experimental broadening was not determined, Figure 5-31b clearly evidence an anisotropic broadening of peaks corresponding to the the (001) plane and to the (*h*0*l*) family of planes. Generally speaking, this can be caused by size effects due to different lengths of coherently diffracting domains in different crystallographic directions and/or direction-dependent microstrain such as stacking faults, turbostraticity and interstratification. These types of defects are real possibilities in brucite-type structures [201] [202] [203]. For example, Radha and coworkers performed XRPD analyses on $Mg(OH)_2$ crystals obtained by various chemical and electrochemical precipitation procedures [202]. In particular, the authors described two particular samples (C, D in [202]) that exhibited selective broadening of the (001) and the (*h*0*l*) family of reflections, which is the case for the $Mg(OH)_2$ obtained by hydration of MgO in the presence of $MgSO_4$ (Figure 5-31b). Through simulation studies (DIFFaX code), the authors concluded that the inclusion of interlayer water led to turbostraticity responsible for the observed line broadening [202].

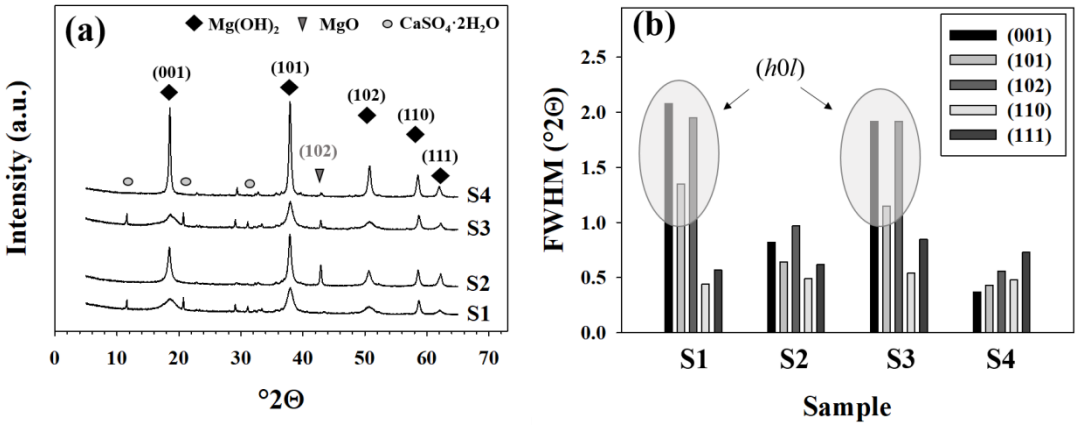

Figure 5-31: XRPD patterns collected from the hydrated cements (ca. 3 months of curing) are shown in (a). The crystallographic planes for $Mg(OH)_2$ and MgO are indicated. The FWHM of the peaks assigned to the brucite-like structure is shown in (b) for each sample. The gray zones highlight anisotropic broadening of the (*h*0*l*) peaks in samples hydrated in the presence of $MgSO_4$. $CaSO_4 \cdot 2H_2O$ is crystallized in the presence of $MgSO_4$ due to $Ca(OH)_2$ impurity in the MgO reagent.

TEM images revealed a platelet (i.e. anisotropic) crystal habit (nanometer thickness) of the hydrated product both in samples with and without $MgSO_4$. Hence, the observed line broadening is thus more likely related to structural defects in $MgSO_4$ containing cements.

5.3.6 Density and porosity

Table 5-11 shows density and porosity of the consolidated samples, i.e. S1 and S3. Samples for which MgO was hydrated in the absence of $MgSO_4$ (i.e. S2 and S4) did not result in a consolidated sample with enough mechanical resistance to be managed without crumbling. High strength of sulphate containing cements was given by highly interlocking micrometer-sized platelet crystals, not only in the matrix but also around the pores templated by the vegetal flour.

Table 5-11: Real density of grinded (ρ_{rp}) and whole (ρ_{rc}) binder, together with the apparent density ρ_{app} and the calculated closed and total porosity (CP and TP, respectively).

	ρ_{rp} (g/cm^3)	ρ_{rc} (g/cm^3)	ρ_{app} (g/cm^3)	CP (%)	TP (%)
S1	2.093 ± 0.001	2.091± 0.002	0.92 ± 0.02	<1	56.0
S3	2.278 ± 0.002	2.229 ± 0.001	1.59 ± 0.02	2.2	30.2

As already observed qualitatively from SEM images presented in the previous section, the sample containing vegetal flower (S1) is more porous (56 %, compared to 30 % for S3). It is interesting to note that the closed porosity is neglectable (Table 5-11). The porous structure was mechanically resistant only when hydration was performed in the presence of $MgSO_4$.

5.3.7 Discussions

5.3.7.1 Hydration kinetics

The MgO powder used as reagent for the preparation of magnesia cement has a large specific surface area (19.8 m^2/g) and is thus highly reactive [204]. The amorphous vegetal flour used as multifunctional admixture is composed of large aggregates (50 vol.% with equivalent diameter <μm) composed of proteins, lipids and carbohydrates, as revealed by FT-IR (Figure 5-17).

Four different aqueous cement compositions were investigated where hydration of MgO was executed in the presence/absence of $MgSO_4$ solution and vegetal flour.

Cements cured at non-ambient temperatures were invariably composed of $Mg(OH)_2$ with only minor amount of residual MgO. A near completion of the hydration reactions was thus obtained. $CaSO_4 \cdot 2H_2O$ (e.g. gypsum) crystallized when hydration

was performed in the presence of $MgSO_4$, the calcium source being a $Ca(OH)_2$ impurity in the MgO reagent. Although it cannot be ruled out that heterogeneous nucleation of hydrated phase on the surface of $CaSO_4 \cdot 2H_2O$ crystals may affect the hydration kinetics, this effect is expected to be negligible considering their low amount (ca. 1.7 wt.% in S3, see section 5.3.5).

No diffraction peaks from magnesium oxysulfate (MOS) cements were observed in neither of the samples, a direct consequence of high-temperature setting favoring fast hydration of MgO, and dry post-hydration storage conditions as will be discussed later.

Hydration of MgO leading to the crystallization of $Mg(OH)_2$ has been extensively investigated in the past by many research groups (e.g. [205] [206] [207] [208]). Based on existing literature and own results, Amaral *et al.* summarized the following reaction sequence in suggested the following hydration model [207];

- reaction between magnesium oxide and water:

$$MgO\ (s) + H_2O\ (l) \rightarrow Mg\ (OH)^+\ (surface) + OH^-$$

- adsorption of hydroxyl ion on the surface:

$$Mg(OH)^+(surface) + OH^-(aq) \rightarrow Mg(OH)^+OH^-(surface)$$

- dissolution:

$$Mg(OH)^+OH^-(surface) \rightarrow Mg^{2+}(aq) + 2OH^-(aq)$$

- crystallization:

$$Mg^{2+}(aq) + 2OH^-(aq) \rightarrow Mg(OH)_2(s)$$

according to which the surface of MgO in contact with water results in a hydroxylated surface in equilibrium with hydroxyl ions in solution. In the next steps, the release of Mg^{2+} and OH^- in solution eventually results in a supersaturated solution leading to nucleation and growth of $Mg(OH)_2$ on the hydrated particles. Important factor governing the kinetics of the reactions are temperature [207–209], and the microstructure of the MgO in terms of porosity and specific surface area [209]. Rocha *et al.* suggested that the dissolution-precipitation process also proceeds in the pores of the MgO particles, leading to a progressive coverage of the surface with newly-formed $Mg(OH)_2$ and a decreased porosity [209]. Hence, the reaction rate decreases and is controlled by diffusion of water in the particle. In a recent work, Xing *et al.* indirectly supported this hypothesis by obtaining an increased hydration

rate through *in situ* ultrasonic action which prevented growth of $Mg(OH)_2$ on the reactive surface [210].

In this work, MgO was hydrated in the presence of $MgSO_4$. According to Amaral and co-workers, the addition of Mg^{2+} ions and SO_4^{2+} ions have two distinct consequences on the hydration process of MgO [207]: i) Common-ion effect that accelerates the precipitation of $Mg(OH)_2$ moving the equilibrium reaction to the right; ii) The electrostatic adsorption of SO_4^{2+} on the hydroxylated MgO surface, leading to the formation of an electrical double layer that repels the negatively charged hydroxyl ions and hence prevent hydration. In addition, the solubility equilibrium of $Mg(OH)_2$ is expected to be affected by the salt concentration as reported in the analogous system $Mg(OH)_2$- $MgCl_2$-H_2O [211].

Considering the results observed in this work for hydration of soft-burned MgO in pure water (sample S4) and in the presence of $MgSO_4$ solution (sample S1, S3): it is observed a delay of accelerated temperature rise in semi-adiabatic tests when hydration was performed in salt solution, indicating the formation of a protective anion layer on the particles. However, this effect was overcome by common-ion effect following longer aging time leading to faster hydration (steeper temperature rise) with respect to samples hydrated in pure water (Figure 5-19).

The effect of the vegetal flour is difficult to individuate due to its very complex chemical nature, including both lipids, proteins and carbohydrates (Figure 5-17). Solubility in the liquid of the various molecules, their charge and state of agglomeration is surely dependent on both temperature, ionic strength, pH etc. Solubility of the proteic part of the vegetal flour in the highly alkaline paste (pH<10) is surely expected [212].

In semi-adiabatic experiments, it is observed a delayed accelerated temperature rise possibly due to an effective screening layer formed by soluble macromolecules with negatively charged functional groups such as carboxylic groups of fatty acids and amino side chains (see FT-IR results). An additional screening effect, prolonging the pre-acceleration period, was observed in the presence of magnesium sulfate.

It is interesting to observe that dissolution and precipitation in the presence of $MgSO_4$ starts immediately and proceeds in a close to linear manner when hydration is performed under isothermal conditions at 35 °C (higher than the temperature at which accelerated rice was observed). Hence, screening of the hydroxylated particle surface by SO_4^{2-} ions does not seem to be effective at this temperature. A part from

temperature dependence on the reactions involved, the faster precipitation of $Mg(OH)_2$ decreases the amount of SO_4^{2-} ions available due to adsorption also on the newly formed crystals. In fact, the ζ-potential measurements performed on the precipitates showed that the addition of SO_4^{2-} ions drastically decreased the ζ-potential from highly positive (33.1 mV) to close to zero (4.2 mV) due to electrostatic interaction between the anions in solution and the positively charged surfaces. Pokrovsky and Schott [213] showed that the $Mg(OH)_2$ particles in aqueous suspensions is dominated by surface $MgOH_2^+$ species and renders the ζ-potential positive (ca. 30 mV in dilute salt solution at pH around 10) with the isoelectric point at very alkaline pH (~11).

The isothermal hydration experiment at 35 °C in the presence of both vegetal flour and $MgSO_4$ (composition S1) shows an induction period for the dissolution of MgO as well as for the crystallization of $Mg(OH)_2$, the former being shorter (170 min and 500 min, respectively). Considering these results and the results observed in semi-adiabatic tests, it appears that not only temperature but also curing time is important factors governing the hydration process in the presence of vegetal flour. In fact, considering that the start of accelerated temperature rise was observed at ca. 33 °C in nonisothermal conditions, a sole effect of temperature would have provoked direct hydration in the isothermal experiments at 35 °C as observed for the samples containing only $MgSO_4$ solution. The time factor indicates a chemical evolution of the vegetal flour which changes its effect on the hydration reactions and eventually weakens the retardant effect.

A striking result was obtained when curing was performed at an isothermal temperature of 20 °C. For sample S1 containing both $MgSO_4$ and vegetal flour, an important amount of 517 phase was crystallized. This phase was absent in the corresponding sample without vegetal flour (sample S3). The phase evolution during curing of sample S1 at 20 °C also showed that the two crystallization reactions did not occur simultaneously (Figure 5-22). In fact, crystallization of MOS 517 started immediately and finished following 44 h of curing, after which $Mg(OH)_2$ started to crystallize and reached near to completion after 7 days (Figure 5-21, Table 5-10). It is well-known that the kinetics of the competitive crystallization of MOS and $Mg(OH)_2$ determines the final phase composition, the former being favored by the addition of MgO hydration retardants such as various acids (see recent review by

Zheng *et al.* [134]). The results presented above thus indicate that a low setting temperature in combination with the used of vegetal flour is needed to favor MOS crystallization, probably through a complex interplay between nucleation/growth kinetics and temperature-dependence of the chemical state of the vegetal flour and its retardant effect on MgO hydration. A major advantage of this new retardant is that the amount of residual MgO is very low in comparison with values reported by others using acids as chemical modifiers (e.g. [34] [138] [139]). This could be related to the time-dependent retardant effect that, on one hand is long enough to promote crystallization of the 517 MOS phase, but on the other hand short enough to allow full hydration of the MgO phase in the later stage of hardening.

5.3.7.2 Cement microstructure and implications on use in insulation boards

The controlled-temperature hydration experiments and subsequent microstructural analyses can be used to explain the absence of MOS in the investigated cement samples. As curing was performed at non-ambient temperature in order to mimic the industrial hot pressing process used by others for this type of material [1], the hydration of MgO to form $Mg(OH)_2$ was kinetically favored despite the retardant effect of the vegetal flour. The non-reacted $MgSO_4$ formed an amorphous fraction mounting to ca. 28 wt.% and situated as a thin film covering the $Mg(OH)_2$ crystals, as observed by TEM analyses.

The results have important implications for concrete preparation and processing methods for the manufacturing of insulation boards using this system as binder. The vegetal flour is a suitable additive to tailor the final phase composition of the cement, promoting the crystallization of $5Mg(OH)_2 \cdot MgSO_4 \cdot 7H_2O$. However, the temperature needs to be carefully controlled. The heat generated by the highly exothermic hydration reactions needs to be dissipated through the use of a filler that increases the heat capacity of the system. Not only the mix proportions become important but also the physical properties of the filler in terms of thermal conductivity and heat capacity. Only cold forming processes are advisable to promote bonding of sulfate in strengthening crystalline phases and avoid loosely held sulfate ions that eventually may lead to post-installation efflorescence of salts. The high amount of $Mg(OH)_2$ that are formed in these systems can eventually react with atmospheric CO_2, forming various magnesium carbonate hydrates with a consequent strength gain.

However, these reactions lead to volume expansion wherefore the cement is best suited as binder in lightweight building materials. The porous structure, also intrinsically present in the binder through pore templating effect of the vegetal flour, not only favor homogenous carbonation (high gas permeability) but also offers buffering space for volume expansion. Controlled curing conditions to favor carbonation and possibly also further bonding of residual $MgSO_4$ salts in MOS phases could be a viable route to obtain a stable material with good technological performance. Although the 517 phase appears to possess good stability towards deterioration by carbonation [135], further work on this issue is needed through controlled experiment evaluated by e.g. full quantitative phase analyses by XRPD and the Rietveld method.

5.4 Development and characterization of bio-based concrete materials

Even the interesting hygrothermal properties of wheat husk (see section 5.1.4), their potential use as lightweight aggregate in bio-based concrete have to be evaluated.

Results reported in this chapter, show properties of bio-based lightweight concretes made with wheat husk as well as hemp hurd taken as reference. Lime based binder and magnesium oxysulfate cement modified by macromolecules (see section 5.3) were investigated in combination with both type of aggregate.

Results show thermal and mechanical properties of bio-based lightweight concretes, together with thorough microstructural investigations of binder hydration by electron microscopy techniques (SEM), as well as X-ray powder diffraction and quantitative phase analyses by Rietveld refinements for magnesia cement and quantitative estimation of the hydrated phases and the carbonates in calcium lime binder from TGA analysis (weight losses determined from the TG curves using stoichiometric formulas). Particular attention was paid toward the impact of aggregates chemical-physical properties on the final concrete performances.

5.4.1 *Design and weight monitoring of concrete specimens: kinetic of hydric stabilization*

The mass loss (Δm) of lime based concrete samples (LWC and LHC) and magnesia based ones (MWC and MHC) during the first 30 days of curing is plotted in Figure 5-32.

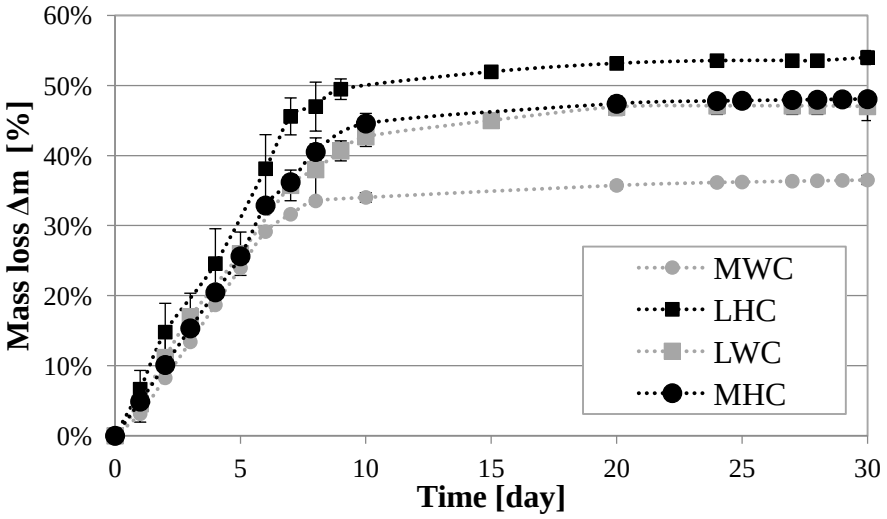

Figure 5-32: Kinetic curves of hydric stabilization for concrete specimens: LHC (black line, square symbol), LWC (grey line, square symbol), MHC (black line, circle symbol), MWC (grey line, circle symbol).

The hydric stabilization time is defined as the point at which the change in concrete density is less than 0.1 % between three consecutive weightings with 24 h time-step. Both types of lime based concretes (i.e. LHC and LWC) reach hydric stabilization after 20 days of hardening (see Figure 5-32), whereas for MHC and MWC specimens this time is slightly longer (i.e. 25 days). The mass loss at hydric stabilization, determined by Eq. (4. 16), was 47 % and 54 % for LWC and LHC, respectively. These values correspond to about 90 wt.% of the initial water introduced in the fresh concrete mixture, in accordance with previous work [69] [149]. The small difference in mass loss between these two types of lime based concretes is due to the different W/B ratios, being higher for LHC. Previous work reported a hydric stabilization time for lime hemp concretes of about 40 days [214] [215]. The large difference between our results and those reported by others is mainly linked to the much smaller sample size used in this work (50 x 50 x 50 mm^3 compared to cylinders with a diameter of 100 mm and a height of 200 mm) which of course accelerates the drying kinetics.

The mass loss of MWC and MHC concretes at hydric stabilization, evaluated using Eq. (4. 16), was 37 % and 48 %, respectively. These values correspond to about 67 wt.% and 79 wt.%, respectively, of the initial water introduced in the fresh concrete mixture. In particular, the lower percentage of evaporated water during the curing time observed for MWC could be correlated to a higher hydration degree of the magnesia binder combined with wheat husk. This result will be fully discussed in section 5.4.6.

The percentages of water loss at hydric stabilization with respect to the initial water content were lower for magnesia based concretes (67 wt.% and 79 wt.% for MWC and MHC respectively) compared to the lime based ones (around 90 wt.% for both LWC and LHC). The main factor determining this difference is surely the type of binder used. Indeed, the setting of the magnesia cement is totally dependent on hydration reactions whereas only C_2S is hydrated in the hydraulic lime at early ages.

5.4.2 Densities and porosities of concrete samples

Table 5-12 summarizes the values of apparent density (ρ_{hs}), dry apparent density (ρ_{dry}), absolute density (ρ_{abs}) and total porosity (η_{tot}) of concrete materials.

Table 5-12: Average densities and porosity of LHC, LWC and MHC, MWC.

Mixture	**Apparent density ρ_{hs} (kg/m^3)**	**Dry apparent density ρ_{dry} (kg/m^3)**	**Absolute density ρ_{abs} (kg/m^3)**	**Total porosity η_{tot} (%)**
LHC	391 ± 12	373 ± 9	2028 ± 20	82 ± 3
LWC	511 ± 12	479 ± 10	2100 ± 25	77 ± 3
MHC	433 ± 10	411 ± 7	1864 ± 5	78 ± 2
MWC	741 ± 13	704 ± 10	1854 ± 5	62 ± 1

The apparent density of LHC and MHC (around 400 kg/m^3), which both contain hemp hurd as aggregate, corresponds to the usual density of Lime Hemp Concrete wall mixture destined for use as an insulting filling material in a wall timber frame. This value is also recommended by the professional rules in hemp construction and similar values were reported in the literature [46] [95]. For example, Collet obtained a total porosity of 84.5 % for molded lime hemp concrete with an apparent density of 381 kg/m^3 [46].

The apparent densities of the lightweight concretes made with wheat husk are considerably higher with respect to ones containing hemp hurd, being about 500 kg/m^3 for LWC and 740 kg/m^3 for MWC (see Table 5-12). Higher densities of these concrete materials were also observed in the fresh state (see Table 4-4). These results may be explained considering the following factors;

- the different density of the two type of aggregates (i.e. hemp hurd and wheat husk). In particular, the apparent particle density (ρ_p) of wheat husk is 35 % higher than that of hemp hurd. This difference is important since it results in a higher volume occupied by hemp hurds compared to that of wheat husks for the same mass;
- different behavior of the fresh concrete mixture under compaction performed during specimens manufacturing. Previous studies showed that the length to width ratio (L/W) of aggregates strongly affects their orientation under compaction and thus the arrangement of the concrete material in the mold leading to higher density for more elongated particles [69] [52] [56]. With this in consideration, the higher L/W ratio observed for wheat husk with respect to hemp hurd (see Table 5-4) could have resulted in a more compact microstructure with the longest particle axis oriented perpendicular to the compaction direction.

The type of aggregate affects the fresh density of concrete, being higher for wheat-based concretes. The difference provoked by the type of aggregate is larger for magnesia-based concrete (41 % compared to 23 % for lime-based ones). A possible explanation could be interactions between wheat husk aggregate and magnesia binder that could affects the packing behavior of the fresh concrete mixture under compaction

It is important to underline that the highest value of ρ_{hs} observed for MWC (see Table 5-12) is a consequence of the highest fresh density of the starting mixture (see Table 4-4) as well as its lowest mass loss during hydric stabilization time (see Figure 5-32).

In contrast to the absolute densities registered for LHC and LWC, whose values differ by 4 %, the ρ_{abs} of the two type of magnesia concrete (MWC and MHC, see Table 5-12) are not statistically different, being about 1859 kg/m^3. Considering the different absolute densities for the two type of aggregates (ρ_{ag}= 1450 kg/m^3 for hemp

hurd and ρ_{ag}= 1507 kg/m^3 for wheat husk, Table 5-5), it is possible to state that the absolute density of the magnesia binder in MWC concrete is necessary lower than the ones in MHC.

Additionally, the difference between the absolute densities of lime based concretes and magnesia based ones, is mainly connected to the binder ρ_{abs} which is lower for the magnesia binder. Hence, this renders it even more interesting as substitute for lime-based binders in lightweight building materials.

The total porosities of LHC, LWC and MHC concretes (see Table 5-12) are not statistically different, being about 80 %. Instead, the value obtained for MWC concrete is significantly lower (62 %) as a consequence of the high dry apparent density.

5.4.3 Dry thermal conductivity of concrete sample

Table 5-13 summarizes the dry thermal conductivity measured for lime based concretes (LHC and LWC) and magnesia based concretes (MHC and MWC).

Table 5-13: Dry thermal conductivity of concrete samples.

Concrete	**Dry thermal conductivity λ_{dry} (W/(m·K))**
LHC	0.089 ± 0.004
LWC	0.092 ± 0.004
MHC	0.119 ± 0.001
MWC	0.168 ± 0.004

Comparing the values obtained for LHC and LWC, it appears that both types of concretes present similar thermal performances even though they have different dry apparent density (Table 5-12). This could be connected to the total porosity, which are similar for both concretes (82 ± 3 for LHC and 77 ± 3 for LWC). However, this is not the case for MHC which presents the same total porosity as the lime based concretes, but has a higher dry thermal conductivity (0.119 W/(m·K) for a dry density of 411 kg/m^3). This could be connected to a higher thermal conductivity of the solid phase in MHC than LWC as will be discussed below. According to the results shown in Table 5-13, the dry thermal conductivity of MWC concrete is much

higher (46 %) with respect to the lime based ones (LHC and LWC). This result is not surprising considering its much lower total porosity (see Table 5-12).

To better understand the impact of the different concrete constituents (kind of aggregate as well as type of binder) on thermal performances of the final material, the thermal conductivity of the solid phase (λ_b) in each concrete (i.e. LHC, LWC, MHC and MWC) was calculated following the method given in section 4.5.3.1. Assuming a value of λ_a (dry air at 20 °C) equal to 0.026 W/(m·K) and the total porosities (*n*) reported in Table 5-12, the thermal conductivity of the solid phase was calculated to be 70.07 mW/(m·K) for LHC, 55.39 mW/(m·K) for LWC, 74.96 mW/(m·K) for MHC and 57.91 mW/(m·K) for MWC. These results show a relevant influence of the aggregate type on λ_b. Indeed, almost independently of the binder considered, the solid phase of concrete made with hemp hurd results 22 % more conductive than the solid phase of concrete made with wheat husk. On the other hand, regarding the binder type, lower discrepancy was observed between λ_b of concrete made with same aggregate but different binder (6.4 % between λ_b of LHC and λ_b of MHC, 4.3 % between λ_b of LWC and λ_b of MWC).

In Figure 5-33, thermal conductivities of the concrete materials developed in the present study are compared with literature data for bio-based lime concretes with B/A mass ratio of 2. Only one study was found in the literature concerning the use of the specific magnesia binder adopted in this thesis work for the development of bio based hemp composite [1]. In addition, those authors used a B/A mass ratio of 1 and a forming method which was quite different from the one used in this work (i.e. hot pressing using two different pressures vrs. cold forming method).

Cerezo *et al.* investigated lime hemp concrete fabricated using different compaction pressures and observed a linear trend between thermal conductivity and density [93]. The result observed here for lime hemp concrete (LHC, see Figure 5-33) slightly deviates (discrepancy ca. 5 %) from values expected from this trend. Higher accordance was found between the results presented here and those reported by Page *et al.* [149] (discrepancy 3 %), possibly because similar casting processes were used. Nguyen *et al.* [52] studied lime hemp concrete and performed thermal conductivity measurements not only perpendicular to the compaction pressure as done in this work but also parallel. The thermal conductivity of the LHC, LWC concretes were lower with respect to the observations of Nguyen *et al.* in perpendicular direction,

but higher than the same measurements done in parallel direction (see Figure 5-33). It is important to underline here that Nguyen *et al.* prepared the concretes using an electromechanical press, which is quite different from the processing route applied in this work. In this context, the anisotropic thermal properties were provoked by alignment of the longitudinal particles with the major axis preferably oriented perpendicular to the compaction axis. The heat flow through the particles is favored along the longitudinal capillaries of the hurds, leading to higher thermal conductivity in the perpendicular direction [52].

It is especially interesting to note that both density and thermal conductivity of LWC are very close to values obtained by Chabannes *et al.* for sunflower concrete specimens (wall mixture) designed with same process [73].

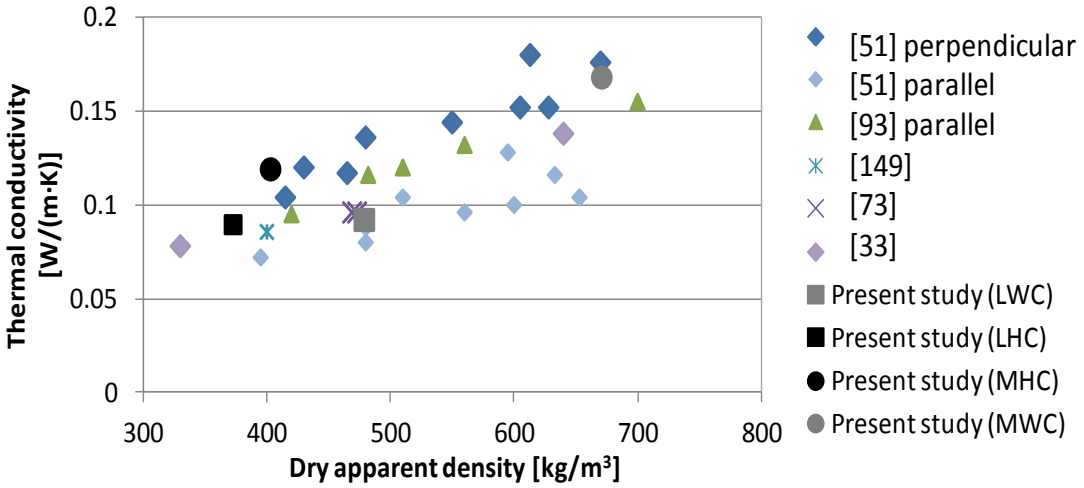

Figure 5-33: Thermal conductivity versus apparent density for dry LHC, MHC (black symbols) and LWC, MWC (gray symbols). Data from the literature is also inserted for comparison.

5.4.4 Thermogravimetric analysis (TGA) of hardened lime binder

The amount of H_2O bound to CSH and residual $Ca(OH)_2$ together with the amount of CO_2 bound to $CaCO_3$ were determined using TGA analyses performed following 10, 30 and 150 days of curing. The content of these phases were then calculated from stoichiometric equations and the results are shown in Table 5-14. Figure 5-34 shows the TG traces of the two types of lime based binder (i.e. binder of LHC and LWC). Only TG traces at 30 and 150 days are shown since TG traces at 10 days are identical to the ones at 30 days.

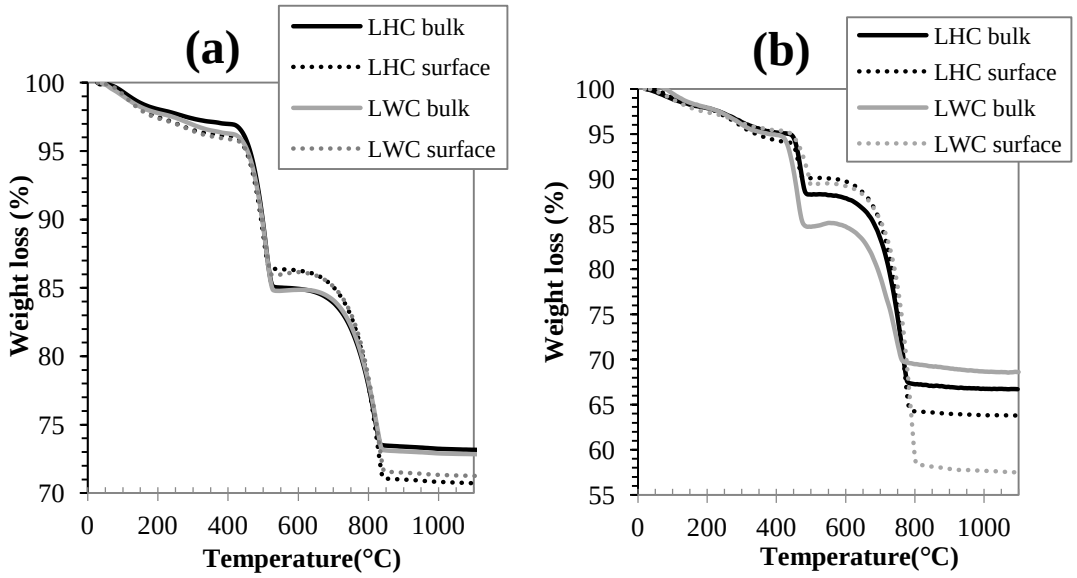

Figure 5-34: TG curves of powdered binder samples collected in the bulk (solid line) and on the surface (dashed line) of lime based concrete samples cured 30 days (a) and 150 days (b).

TG traces are very similar at 30 day of curing (illustrated in Figure 5-34a), near to identical, indicating similar phase compositions. Only minor differences are observed for specimens collected from the bulk and surface of the same concrete sample both regarding carbonated lime as well as hydrated clinker phases. At 150 days (see Figure 5-34b), the binder samples collected on the surface (dashed line) show a substantial increase of $CaCO_3$ for which the thermal decomposition occurs between 600 and 850°C. However, $Ca(OH)_2$ is still present in both lime binders collected on the surface and in the bulk of concrete specimen. This is not surprising as it is well known that the carbonation reactions of lime-based binders are slow.

These visual observations are confirmed by the results shown in Table 5-14. Similar amounts of $CaCO_3$ were detected for both types of concretes at 10 and 30 days of curing.

Due to direct air exposure, binder specimens collected from the surface show a higher content of $CaCO_3$, and consequently a lower content of $Ca(OH)_2$, compared to those collected from the bulk. Carbonation of $Ca(OH)_2$ should be an important hardening mechanism in the concretes studied here, especially considering the high porosity and pore connectivity. Gradual carbonation results in increased weight and decreased porosity which determine a progressive improvement of the mechanical strength up to several months.

Regarding the amount of water involved in the hydration of the two types of cements, nearly identical values are observed since early age for surface samples (about 3.7 % for LHC and 3.5 % for LWC) whereas a minor discrepancies were observed between bulk and surface specimens of the same concrete Figure 5-34, Table 5-14). A higher degree of hydration is observed on the surface with respect to the bulk. Chabannes et al. observed similar trends for rice husk and hemp concrete systems, which were explained by a synergy effect between carbonation and hydration [71]. The authors assumed that water locally provided by the carbonation reaction could benefit C_2S hydration.

Table 5-14: Compositional data for LHC and LWC binder obtained using TG data (Figure 5-34). The amount of H_2O bound to CSH together with the wt.% of residual $Ca(OH)_2$ and $CaCO_3$, the latter two calculated from weight loss in specific ranges in the TG curves (see 4.5.4 for details), are depicted.

Curing time (days)	Binder sample	Water bound to C-S-H (%)	$Ca(OH)_2$ (%)	$CaCO_3$ (%)	Carbonation degree (%)
10	LHC surface	3.7	44.3	32.0	20.1
	LHC bulk	2.7	51.0	24.2	10.7
	LWC surface	3.5	43.9	32.7	20.9
	LWC bulk	2.7	49.2	26.3	13.2
30	LHC surface	3.4	40.1	34.6	26.4
	LHC bulk	2.5	49.2	26.0	16.0
	LWC surface	3.3	40.8	33.2	24.7
	LWC bulk	2.7	47.3	26.7	16.8
150	LHC surface	3.9	17.1	58.2	51.5
	LHC bulk	3.2	28.5	47.3	38.5
	LWC surface	3.6	8.2	70.8	66.7
	LWC bulk	3.0	40.2	35.3	24.0

5.4.5 Microscopy observations of lignocellular aggregates in lime based concretes

Figure 5-35 shows optical and SEM observations of hemp hurd and wheat husk surfaces collected from concretes.

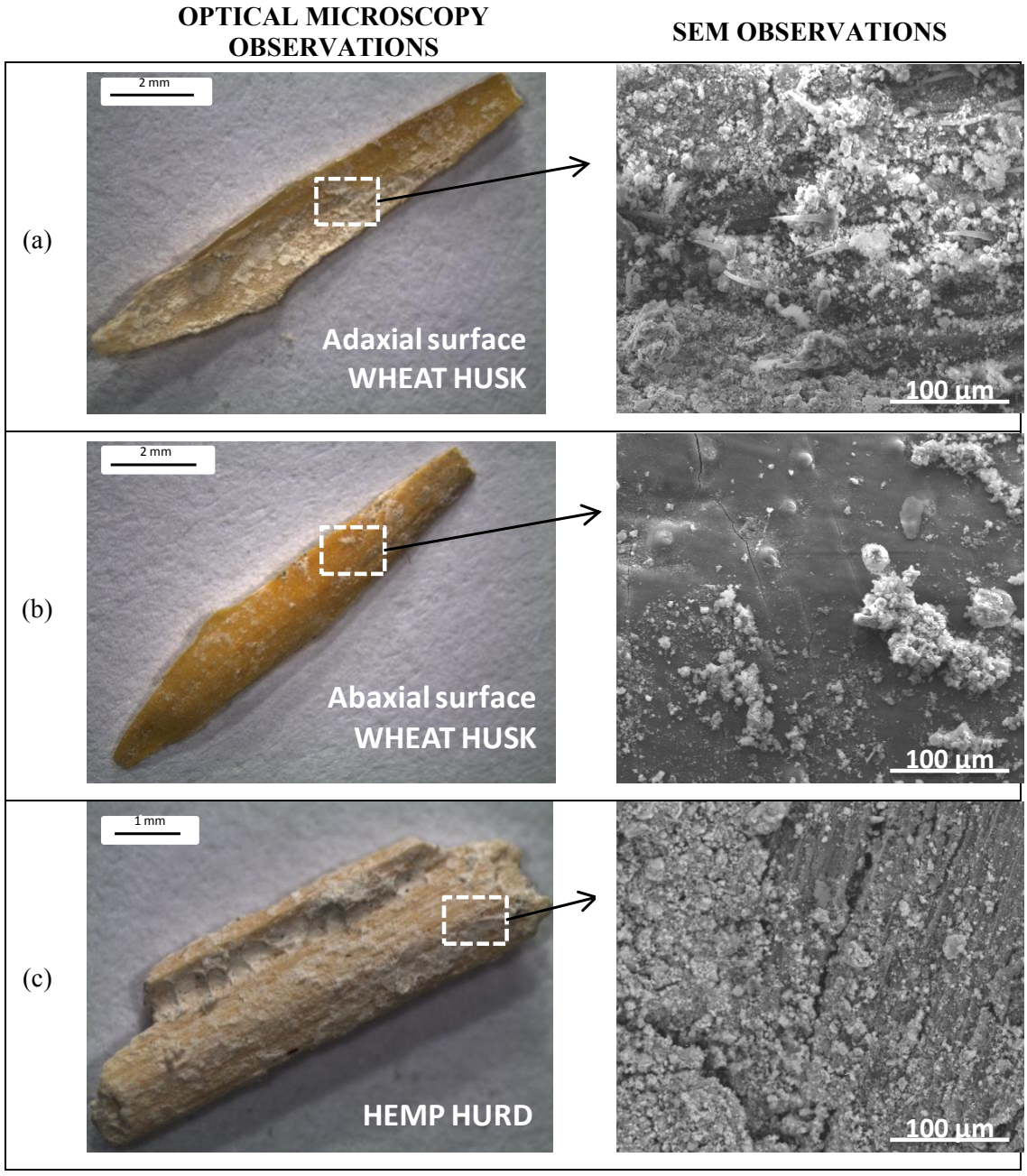

Figure 5-35: Optical microscopy observation (left side) and SEM micrographs (right side) the adaxial surface (a) and abaxial surface (b) of wheat husk in LWC, hemp hurd surface in LHC (c).

Figure 5-35a and Figure 5-35b evidence an inhomogeneous adhesion of lime particles to wheat husk surface. A fairly good surface coverage of cement is observed on the adaxial surface (a) whereas the abaxial surface is rather clean (b). These

differences are explained by the higher roughness of the adaxial surface and the presence of aerial surface hairs which is expected to improve mechanical interlocking with the lime binder.

The surface of hemp hurd seems to be well covered with the lime binder, see Figure 5-35c. The high porosity which characterizes hemp (Figure 5-1a, Figure 5-1c) could have facilitated the penetration of the binder and thus the creation of anchorage points. Additionally, the presence of a higher amount of covalent hydroxyl, phenolic or alcoholic groups of cellulose and lignin in hemp hurd (see section 4.1.2, FT-IR analysis and Van Soest method) could enhance the adhesion of these aggregates with lime binder. Indeed, as shown by Coutts and Kightly [216], hydrogen bonding and/or hydroxyl bridges between the hydroxyl groups of the cement phases and these covalent groups of aggregate could play a major role in the chemical interaction between lignocellular aggregates and lime binder.

5.4.6 X-ray Powder Diffraction on hardened magnesia binder

In order to investigate the curing time sensibility of the magnesia-binder phase composition, XRPD patterns were collected following 10 and 30 days of curing and semi-quantitative phase analyses were performed by the Rietveld method. Figure 5-36 shows the XRPD patterns of the magnesia binder separated from MHC (Figure 5-36a) and MWC (Figure 5-36b), whereas Table 5-15 shows the semi-quantitative results.

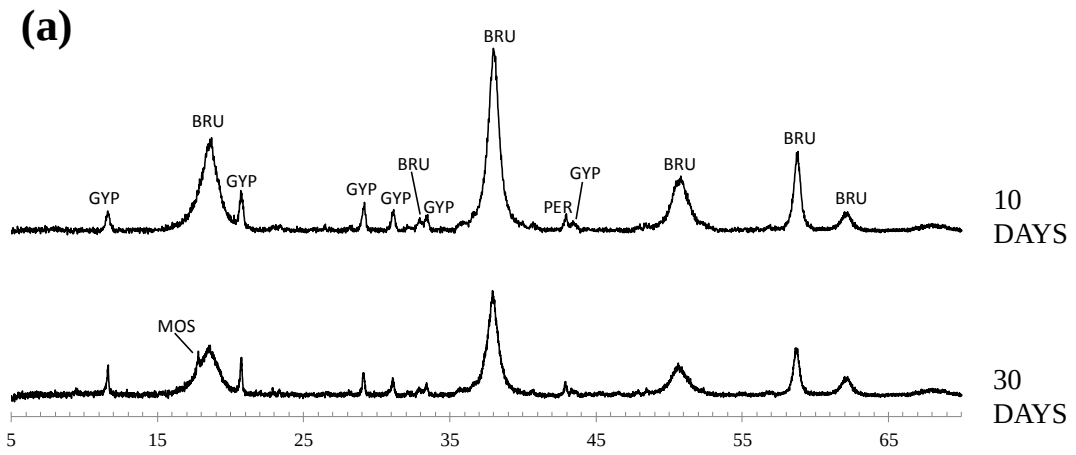

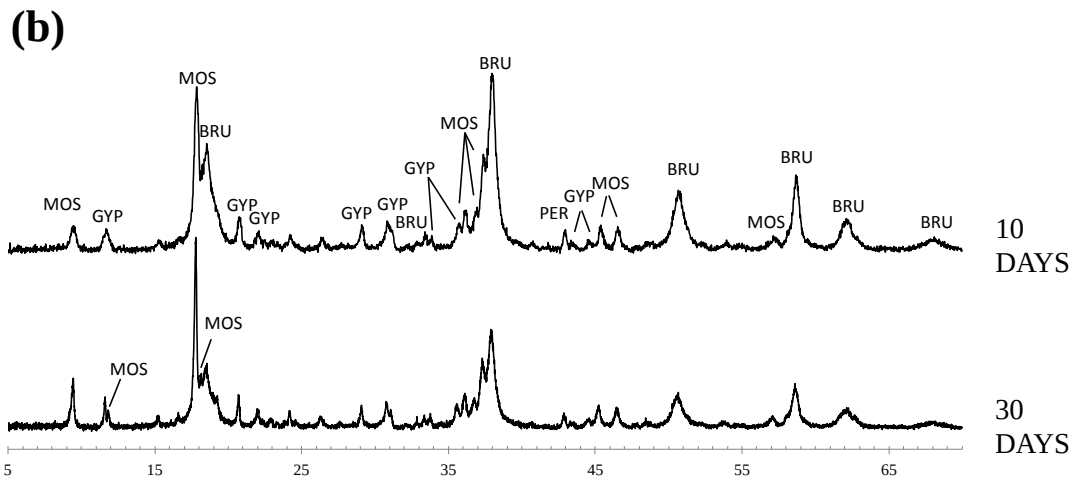

Figure 5-36: X-ray diffraction patterns of magnesia binder based MHC at 10 and 30 days of curing (a) and magnesia binder based MWC at 10 and 30 days of curing (b). MOS= Magnesium oxysulfates ($5Mg(OH)_2 \cdot MgSO_4 \cdot 7H_2O$, 517 phase); GYP= Gypsum ($CaSO_4 \cdot 2H_2O$); BRU= Brucite ($Mg(OH)_2$); PER= Periclase (MgO).

Table 5-15: Results from semi-quantative phase analyses (XRPD and Rietveld refinements) of hardened magnesia binder based MHC and MWC cured 10 and 30 days.

Sample	Curing time (days)	$Mg(OH)_2$ (wt.%)	517 MOS (wt.%)	MgO (wt.%)	$CaSO_4 \cdot 2H_2O$ (wt.%)
Hardened magnesia binder based MHC	10	89.6 (1)	2.4 (5)	1.6 (1)	6.4 (2)
	30	85.6 (1)	5.8 (2)	2.2 (1)	6.4 (1)
Hardened magnesia binder based MWC	10	59.1 (2)	34.0 (3)	1.8 (1)	5.1 (2)
	30	49.9 (1)	44.0 (2)	1.7 (1)	4.4 (1)

The hardened binders are composed of $Mg(OH)_2$, 517 MOS phase ($5Mg(OH)_2 \cdot MgSO_4 \cdot 7H_2O$) and $CaSO_4 \cdot 2H_2O$. The crystallization of this latter is the result of the hydration in the presence of $MgSO_4$ and a calcium source being a calcium hydroxide impurity in the magnesium oxide reagent (see section 5.2.3). As outlined in Table 5-15, only minor amount of residual MgO was found in both magnesia binder samples, therefore a near completion of the hydration reactions was obtained. This is an important result since many studies [34] [136] [217], where phase composition of $MgO\text{-}MgSO_4\text{-}H_2O$ systems were investigated, shown important amount of unreacted MgO particles in the hardened cement. In these works [34][136] [217], citric acid was used to promote the crystallization of magnesium

oxysulfate (517 phase) rather than magnesium hydroxide during the reaction between soft-burned MgO and magnesium sulfate solution. However, the presence of unreacted MgO can have detrimental effects on the mechanical properties of the cement due to post-hardening hydration in contact with water and consequent volume expansion [138].

The presence of 517 MOS phase in MHC and MWC binders is particularly important for improving the early age strength [218], as well as promoting bonding of sulfate in strengthening crystalline phases and avoid loosely held sulfate ions that eventually may lead to post-installation efflorescence of salts. Additionally, the high amount of $Mg(OH)_2$ that invariably are formed in these systems can eventually react with atmospheric CO_2, forming various magnesium carbonate hydrates with a consequent strength gain.

As illustrated in Table 5-15, both magnesia binders are characterized by a reorganization of the solid phases with time, showing a decrease of the $\frac{Mg(OH)_2}{517\ MOS}$ weight ratio from 10 to 30 days of curing. In particular, this weight ratio decreases from 37.3 to 14.8 in case of MHC binder, whereas it appears significantly lower (1.7 and 1.1 at 10 and 30 days, respectively) when MWC binder is considered. Given the binder formulation used in this study (see section 4.4), it is interesting to evaluate its best phase composition linked to the lowest possible $\frac{Mg(OH)_2}{517\ MOS}$ weight ratio. Assuming that: i) all MgO is consumed in hydration reactions (to form $Mg(OH)_2$ or 517 MOS phase); ii) all calcium present as impurity in the MgO reagent (section 5.2.3) reacts with magnesium sulfate solution to form $CaSO_4 \cdot 2H_2O$; iii) all residual $MgSO_4$ is involved in 517 MOS phase crystallization; the $\frac{Mg(OH)_2}{517\ MOS}$ weight ratio calculated using stoichiometric formulas is equal to 0.9. This latter information is particularly interesting considering the value equal to 1.1 observed for MWC. Indeed for MWC binder a nearly complete bonding of residual $MgSO_4$ salts in MOS phases is obtained and thus provide to obtain a stable material with higher mechanical performances and better water resistance [204].

The large difference between the amount of 517 MOS phase crystallized in the two system (MWC binder and MHC binder) could be partially explained considering the heat capacity of the two concrete materials. As explained in section 5.3, where the magnesia cement formulation were investigated in detail (sample S1, see Table 4-2), setting temperature needs to be controlled. In fact, at temperatures higher than 35 °C

no crystallization of 517 MOS phase was observed. In concrete materials developed in this study, the heat generated by the highly exothermic binder hydration reactions is dissipated through the use of vegetal flour and aggregates (wheat husk or hemp hurd) as filler that increases the heat capacity of the system. Considering the higher specific heat capacity of wheat husk (1800-1900 J/(kg·K) [219]) than hemp hurd (around 1272 J/(kg·K) [31]) and the higher void content estimated in fresh MHC concrete, it is possible that higher temperatures are reached during setting of MHC, thus favoring the crystallization of $Mg(OH)_2$ over 517 MOS phase. Moreover, also the higher water to binder ratio used in MHC mixture (Table 4-4) could influence the 517 MOS phase crystallization. Indeed, Wu *et al.* [138] reported that high water/cement ratio in MOS cements results in an increased prevalence of $Mg(OH)_2$ compared to 517 phase. Similar results were obtained for MOC (magnesium oxychloride cements), in which the content of $Mg(OH)_2$ increased and $5Mg(OH)_2 \cdot MgCl_2 \cdot 8H_2O$ phase decreased when the water/cement ratio increased [220] [221]. These observations could be connected to the lower salt ions concentration in MOS cement (characterized by higher water/cement ratio) and consequently lower reaction rate for 517 phase crystallization.

Differences in phase composition between the two binders after 30 days of curing could also explain the lower absolute density of the magnesia binder in MWC concrete (see section 5.4.2). Indeed, in MHC binder the $\frac{Mg(OH)_2}{517\ MOS}$ weight ratio was found to be 14 times higher than MWC ones and considering the different crystal density of these phases ($Mg(OH)_2$= 2.37 g/cm^3 and 517 MOS phase= 1.79 g/cm^3), it is thus motivated the higher binder absolute density of MHC.

5.4.7 Scanning electron microscopy observations of magnesia based concrete samples

Figure 5-37 shows SEM images of magnesia binder from different zones observable in a freshly exposed surface of the bulk of MHC and MWC following 30 days of curing. In both binders, a porous structure was observed with pores smaller than 100 µm in diameter (see Figure 5-37a and Figure 5-37b). Irregularly shaped pores in the range 60-70 µm and 40-50 µm are observed for MWC and MHC, respectively (see Figure 5-37c and 5-37d). The pores are thus slightly smaller in MHC with respect to

MWC. Smaller spherical pores (<20um, see Figure 5-37e and Figure 5-37f) are also observed in both MWC and MHC. Some of them are lined with residual organic matter which indicates that they were templated by the vegetal flour. Entrapped air may also be responsible for these smaller pores.

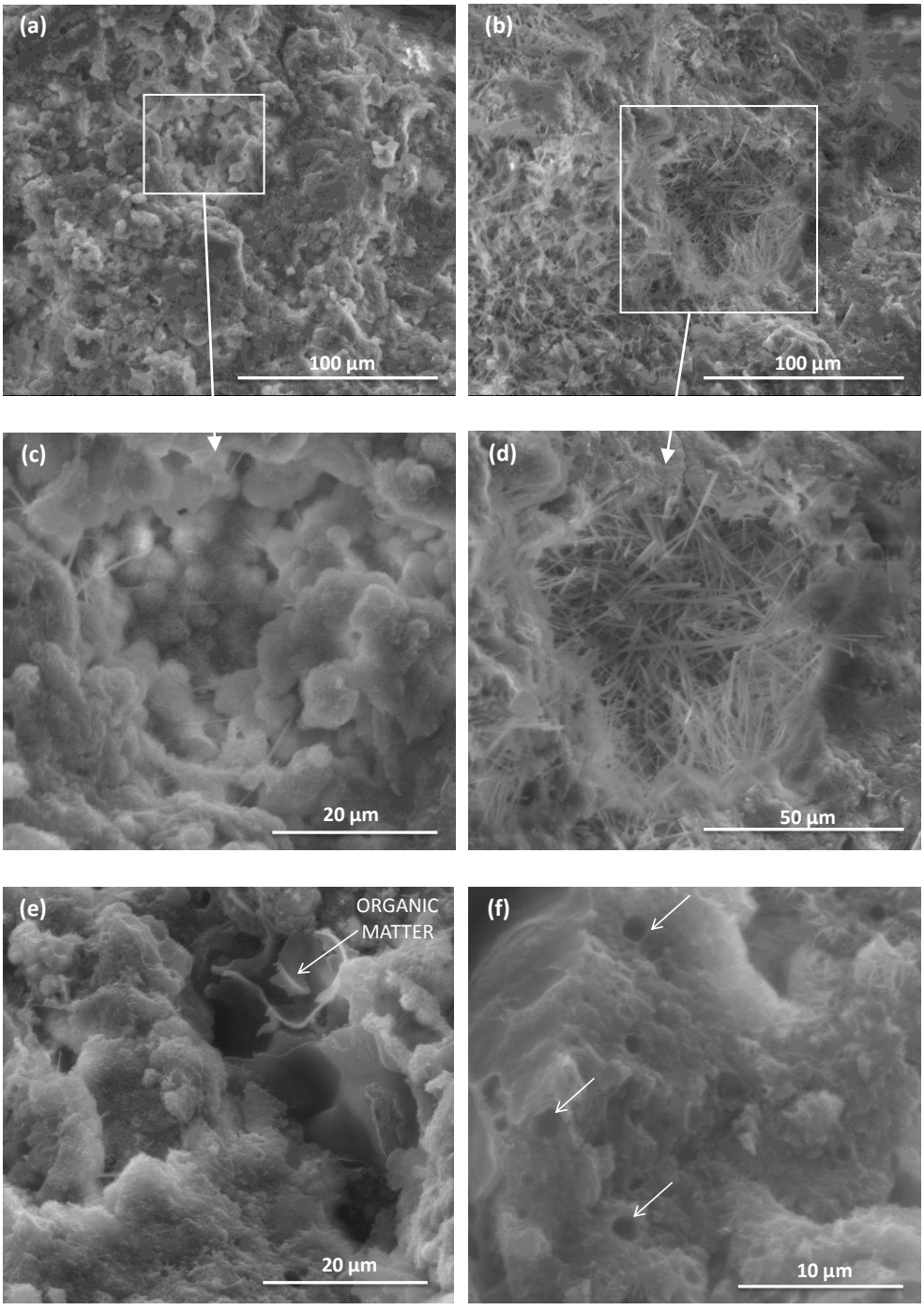

Figure 5-37: SEM micrographs of MHC binder sample (a, c) and MWC binder sample (b, d) following 30 days of curing. The images show a porous structure (a, b) and the irregular shape pores ranging from 40 to 50 µm in MHC binder (c) and 60-70 µm in MWC binder (d). Both binder show spherical pores of 10-15 µm in diameter covered with a transparent film of organic matter (e) and fine porosity of 1-2 µm (f).

The open porous structure (see Figure 5-37), intrinsically present in the binder through pore templating effect of the vegetal flour and water, should render the material highly permeable and thus favor homogeneous carbonation of Mg(OH)2. Indeed, the high amount of $Mg(OH)_2$ that invariably are formed in these systems (Table 5-10) can eventually react with atmospheric CO_2, forming various magnesium carbonate hydrates with a consequent strength gain.

As reported in Figure 5-38a and confirmed by XRD analysis (see section 5.4.6), binder hydration in the presence of hemp hurds (MHC binder) resulted in a heterogeneous microstructure composed of a rather open network of dense zones and interlocking platelets crystals of magnesium hydroxide. As explained in section 5.3.3.1, the dense zones are probably the result of hydration within porous magnesium oxide aggregates where the availability of sulfate ions is limited by diffusion, whereas the open network of large platelets is the result of crystallization and growth in the supersaturated solution. Moreover, small amount of microcrystalline needles, assigned to 517 MOS phase [135], can be seen with an average length of 9–11 µm. The 517 MOS phase appears to crystallize in a preferential manner on the pore walls. This suggests a heterogeneous nucleation and growth on the interface between the vegetal flour and the surrounding matrix.

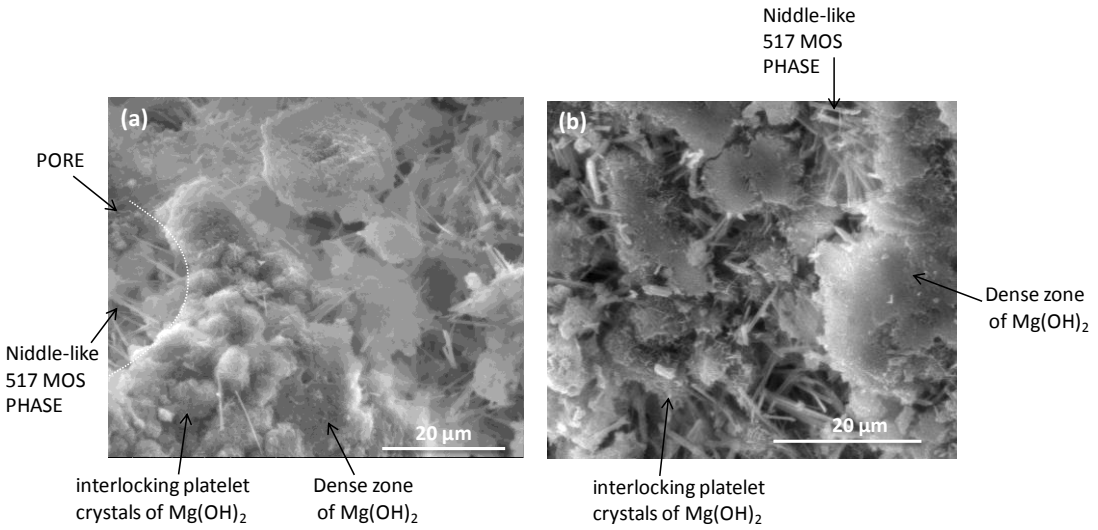

Figure 5-38: SEM micrographs of the MHC binder (a), and the MWC binder (b) following 30 days of curing.

Figure 5-38b shows SEM images of hardened MWC binder. Despite having the same formulation as the MHC binder in the fresh state, the phase composition after 30 days of curing outlines differences (see Table 5-10) evidenced also by microstructure

comparison. In particular, a higher amount of needle-like 517 MOS phase was found in MWC binder (binder hydration in the presence of wheat husks). As evidenced in Figure 5-38b, these crystals are connected together to form a criss-crossing network which is the main strength resource of MOS cement paste [135,204]. Additionally, lower amount of brucite interlocking platelets crystals are evidenced in MWC binder. This result could be a consequence of 517 MOS phase crystallization, a competing phase in this system. Crystallization of $Mg(OH)_2$ appears mainly in porous aggregates of MgO where the availability of SO_4^{2-} is limited, thus forming dense zones (see Figure 5-38b and discussions in 5.3.3.1).

As shown in Figure 5-39a and Figure 5-39b, both types of concretes show a higher amount of 517 MOS phase crystals close to aggregates. This could possibly be explained by a different chemical environment in this zone with respect to the bulk, promoting nucleation and/or crystal growth. However, more experimental work is needed to fully explain this observation.

Moreover, a fairly good coverage of the aggregate surface by the binder is observed (see Figure 5-39a, c, d). The roughness of the aggregate surface should promote mechanical interlocking with the magnesia binder (Figure 5-39c, d). In addition, the open pores of the aggregate probably facilitate the penetration of the binder (see Figure 5-39c, a for wheat husk, Figure 5-39f for hemp hurd) and thus the creation of anchorage points.

It is interesting to observe that 517 MOS crystals are present also inside the wheat husk particle, see Figure 5-39e. The aggregate thus seems to act as “mini-reactor” for nucleation and crystal growth, creating a dense connected network between wheat husk aggregate and surrounding binder. This particular microstructural feature, only observed for wheat husk, could have an important effect on the mechanical properties of the concrete.

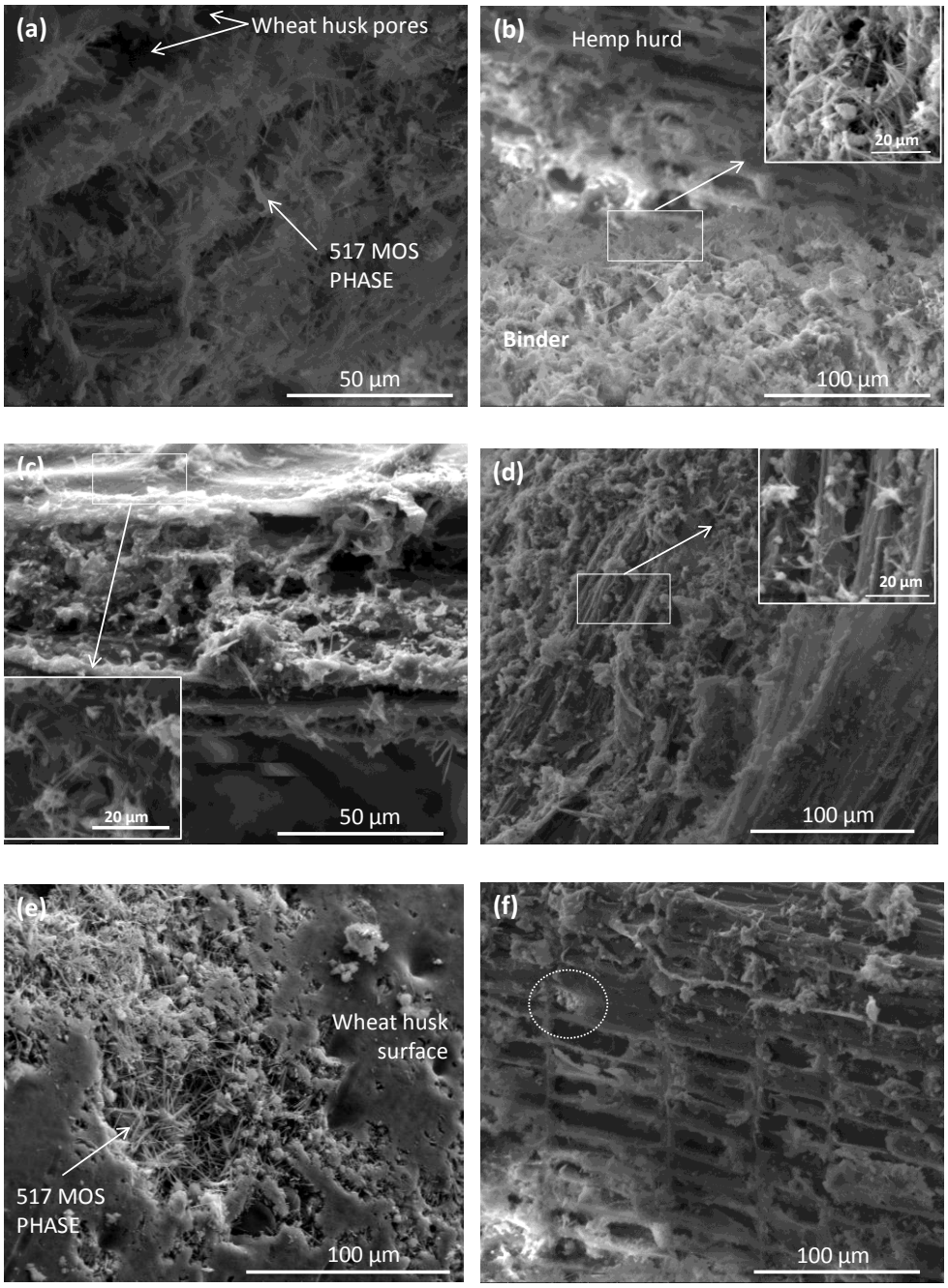

Figure 5-39: SEM micrographs of wheat husk in MWC concrete (a, c, e) and hemp hurd in MHC concrete (b, d, f).

5.4.8 Mechanical properties of bio-based concrete

5.4.8.1 Compressive strength of lime based concrete

The results obtained from the compression tests on lime based concrete (i.e. LHC and LWC) are presented in Figure 5-40. The stress versus strain curves (Figure 5-40a and Figure 5-40b) highlight some differences in mechanical behavior for LWC and LHC. According to other studies [47] [55] [95], the first part of the curves shows linear quasi-elastic behavior where the binder mainly supports the compressive stress. Here, LWC and LHC seem to have same stiffness at early age (i.e. 10 days). However, following longer curing times (30 days and 150 days) LHC became less deformable under stress compared to LWC (see Figure 5-40a and Figure 5-40b). Both concretes change their behavior towards an elastoplastic one in consequence to the progressive cracking of the binder. In the stress versus strain curve, this change is evidenced by a knee point. As shown in Figure 5-40c, it appears that this progressive inflection of the stress/strain curve occurs at lower stress level for LWC. As detailed in literature [67], this could suggest a lower adhesion between binder and wheat husk aggregates and/or a lower intrinsic quality of the lime-based binder. However, considering the TGA analyses presented in previous section 5.4.4 (Table 5-14), the amount of cement phases (i.e. CSH and $CaCO_3$) are similar for both types of concretes at 10 and 30 days of curing. Hence, the most plausible explanation should be a weaker aggregate-binder interface. This hypothesis is supported by the SEM observations (Figure 5-35), where an inhomogeneous adhesion of lime particles to wheat husk surface is evidenced.

From the knee point, the load is progressively transferred to the aggregates since the binder and the interface between aggregates and binder are progressively damaged. In addition, during this phase the aggregate cells begin to collapse due to the compression load which first closes voids between particles and later inside the particles themselves. In concrete made with wheat husk, the compression stress does not lead to a failure point as observed for LHC samples, but induces irreversible compaction to a dense phase in which the pores are almost closed and the sample become more and more rigid.

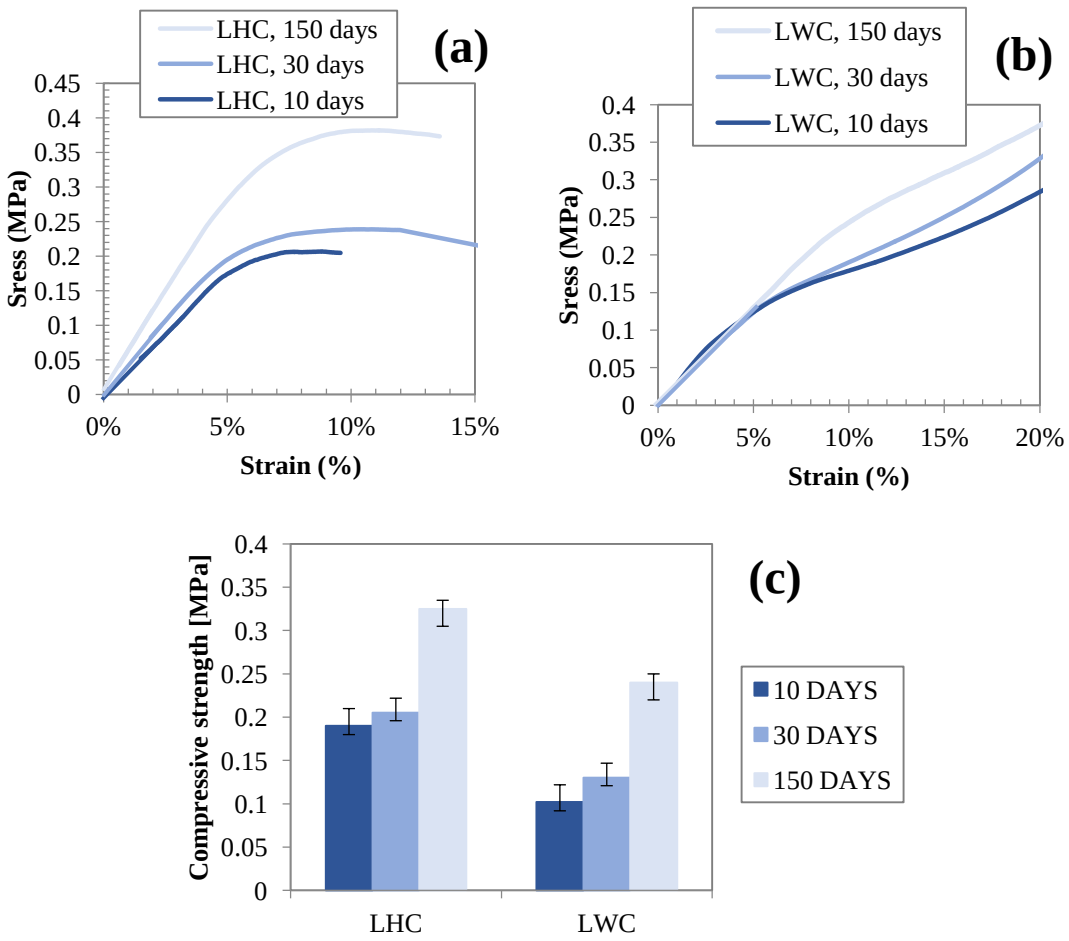

Figure 5-40: Stress-strain curves of LHC concrete specimens (a), stress-strain curves of LWC concrete specimens (b), mean values of compressive strength of LHC and LWC at different age (c).

Despite the higher apparent density of LWC (511 kg/m^3) with respect to LHC (391 kg/m^3), and the nearly identical total porosity of the two concretes (around 80 %, Table 5-12), lower mechanical performances were registered for LWC with respect to LHC, being about 0.130 ± 0.009 MPa and 0.205 ± 0.017 MPa following 30 days of curing, 0.24 ± 0.02 MPa and 0.325 ± 0.01 MPa at 150 days, respectively.

Nevertheless, it should be noted that the result obtained for LWC at 150 days satisfies the minimum threshold value of the French professional rules, which recommend a compressive strength value of 0.2 MPa for wall mixtures (B/A=2) lime hemp concrete. Indeed, thanks to the progressive carbonation of the binder, it is expected that longer maturation results in a higher mechanical performance.

The results obtained for LHC can be compared with those reported by Page *et al.* [149], who tested cubic specimens (50x50x50 mm^3) of hemp concrete manufactured with the same casting procedure used in this work. Following 30 days of curing, Page *et al.* obtained a maximum compressive stress (defined at 5 % strain) of 0.22

MPa and 0.14 MPa for hemp concretes with apparent densities of 380 kg/m^3 (B/A=1.86) and 400 kg/m^3 (B/A=2.11), respectively. In our case (B/A=2), the compressive strength at 5 % strain was found to be 0.19 MPa, which is in good agreement with their results.

5.4.8.2 Compressive strength of magnesia based concrete

The results obtained from the compressive tests of magnesia based concretes, performed at 10 and 30 days of curing, are presented in Figure 5-41. As fully discussed in the literature for other types of lightweight concrete materials (in the literature for hemp concrete) [47][95], curing time strongly affects mechanical behavior. In this study, the compressive strength at 10 and 30 days for MHC was 0.51 MPa and 0.81 MPa, respectively. The corresponding values registered for MWC were 1.10 MPa and 2.35 MPa. These results are not directly comparable in consequence of the higher apparent density of MWC (741 kg/m^3) with respect to MHC (433 kg/m^3). Nevertheless, some interesting considerations can be done.

Firstly, having chosen to consider the concrete ultimate strength as the point at which the mechanical behavior departs from a linear stress/strain curve, our results are inevitably influenced by the concrete behavior in the first part of the stress-strain curve. Here, according to literature data [47] [55] [95], a linear quasi-elastic behavior is observed and the compressive stress is mainly supported by the binder. Both types of magnesia based concrete seem to be more deformable and less resistant at 10 days, in consequence to the incomplete binder hydration at this age. As shown by X-ray powder diffraction performed on hardened binders (section 5.4.6), a reorganization of the solid phase occurs during time, showing a decrease of the $\frac{Mg(OH)_2}{517\ MOS}$ weight ratio from 10 to 30 days of curing (Table 5-15). The increased compressive strength observed from 10 to 30 days (ca. 59 % for MHC and 113 % for MWC) could thus be connected to the progressively higher amount of 517 MOS phase in the concrete binders. These needle-shaped crystals create a dense criss-crossing network in the porous network of the binder (Figure 5-37b, Figure 5-37d), within $Mg(OH)_2$ phases (in the solid matrix) (Figure 5-38) as well as between aggregates and binder (Figure 5-39a, Figure 5-39b), thus enhancing concrete mechanical performances. The $\frac{Mg(OH)_2}{517\ MOS}$ weight ratio in MHC decreased with 60 % from 10 to 30 days of curing (see Table 5-15). At the same time, the compressive strength increased with 60 %. The

positive effect of a decreased $\frac{Mg(OH)_2}{517\ MOS}$ ratio on the compressive strength was more pronounced for MWC. In fact, the decrease of the $\frac{Mg(OH)_2}{517\ MOS}$ weight ratio was only 35 % but the compressive strength increased with 113 %. This result could be connected to the presence of 517 MOS phase also inside wheat husk aggregates (Figure 5-39e) creating not only a dense connected network between wheat husk aggregate and surrounding binder, but also an enhanced skeletal structure for the highly porous aggregate which represent the weakest link in concrete system, in term of mechanical performances.

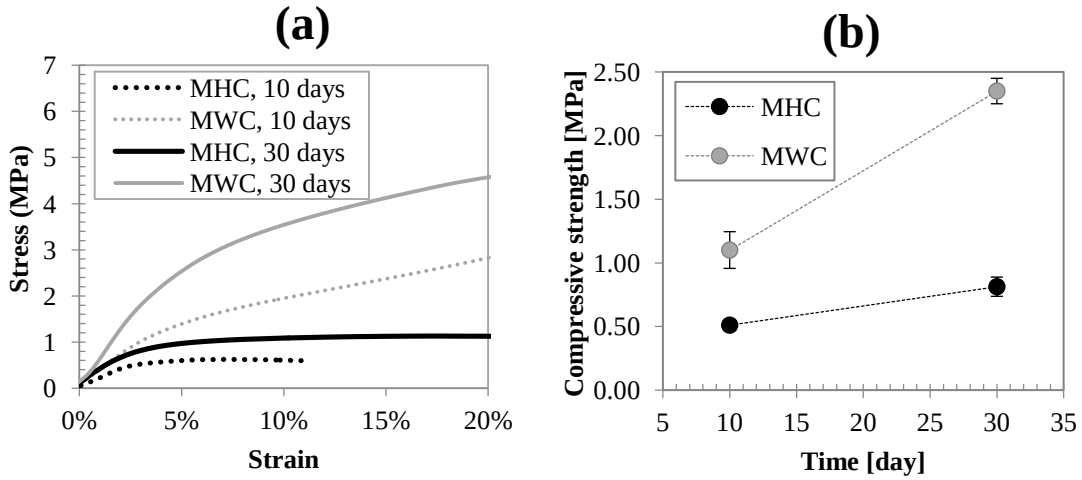

Figure 5-41: Stress-strain curves of concrete specimens (a), mean values of compressive strength of MHC and MWC at 10 and 30 days of curing (b).

6 Conclusions and future developments

For the first time, local wheat husk was used as lightweight aggregate for the development of eco-friendly building materials. Contrary to what is normally done for other investigated wheat husk applications, this residue was valorized without any energy-consuming pre-treatments (e.g. burning, grinding or surface modifications).

With the purpose to evaluate its potential use as lightweight aggregate in agro-concretes, a full chemical-physical characterization of wheat husk was performed. Additionally, comparison was made with hemp hurd, chosen as reference because of its wide use in commercial lightweight building materials.

It was found that the thermal conductivity (0.051 W/(m·K)) and the hygric capacity (MBV of 2.06 g/(m^2·%RH)) were close to identical for the two types of investigated agro-wastes and in high accordance with values reported in the literature for hemp hurd. These result were of mandatory importance for this thesis work as they supported the possibility of substituting hemp hurd for wheat husk in agro-concrete. Analogous to hemp hurd, this biomass residue can be classified as being both a good thermal insular (according to the standard NF P75-101) and an excellent hygric regulator (according to the classification of the NORDTEST Project). Indeed, it could be used to produce thermal insulating products or indoor facing panels (like partition walls or ceiling) potentially having the same advantages as corresponding products based on hemp hurd (i.e. direct and indirect energy savings, maintenance of air quality and hygrothermal comfort).

Results obtained in this work showed that wheat husk had a lower water absorption capacity with respect to hemp hurd (Initial Rate of Absorption from 0 to 1 min, 194 % for wheat husk and 292 % for hemp hurd). This is an important advantage of the former as it could reduce the competition for water between the hydraulic binder and the vegetal aggregates in the fresh concrete mixture and thus ensure water availability for cement hydration. As an adjustment of water content in agro-concrete fresh mixtures is usually done considering the water absorption capacity of the biomass aggregate, it could be possible to design a fresh concrete with a lower water to binder mass ratio when wheat husk is used instead of hemp hurd.

Two different binders were used for the preparation of hemp hurd-concrete and wheat husk-concrete: a traditional lime-based binder generally used in agro-concretes

and a magnesia-based one (so-called magnesium oxysulfate (MOS) cement composed of reactive MgO and $MgSO_4$ aqueous solution) recently proposed by others for the preparation of hemp-based insulation panels. The novelty of the latter binder was the addition of a vegetal protein-rich flour to an ordinary MOS cement, giving improved technological properties of the final composite. However, the authors never reported chemical-physical properties of the modified MOS binder. Hence, this gap was fulfilled in this thesis work through a thorough investigation of cement microstructure and hydration kinetics. In particular, the effect of the vegetal flour (composed of proteins, carbohydrates and lipids) on the hydration kinetics of MgO was investigated together with the microstructural properties following completed reactions. It was found that the vegetal flour had a retardant effect on hydration of MgO, possibly through poisoning of the reactive surface through electrostatic interactions. This effect was found to favor the crystallization of $5Mg(OH)_2 \cdot MgSO_4 \cdot 7H_2O$, a desired needle-shaped MOS cementitious phase when curing was performed at 20 °C. At higher curing temperatures, the hydration of MgO to form $Mg(OH)_2$ was kinetically favored despite the retardant effect of the vegetal flour. Hence, non-reacted $MgSO_4$, forming an amorphous phase situated as a thin film covering the $Mg(OH)_2$ crystals, may give rise to problems with efflorescence. These results put important constrains on the type of forming method suitable for agro-concretes based on the novel MOS binder. In fact, the hot pressing method used by the authors in the pioneering work was exchanged for a low-temperature manufacturing route in order to promote the crystallization of desired MOS phases and avoid non-reacted $MgSO_4$. The possibility of using a traditional cold forming method was a key finding at it allowed to follow existing protocols for the manufacturing of lime hemp concrete, the target substitute product.

The main conclusions that could be drawn from the studies regarding the four types of agro-concretes (i.e. lime hemp, lime wheat husk, magnesia hemp, magnesia wheat husk) were the following:

- The lightweight building materials were highly porous and similar values of total porosity were observed for all types of concretes (i.e. ca. 80 %), the only exception being the magnesia-based concrete prepared with wheat husk which had a slightly lower porosity (ca. 62 %).

- Regarding lime-based concretes, the dry thermal conductivity was similar for both types of aggregate (0.09 W/(m·K)). However, the compressive strength of concretes containing wheat husk (evaluated following 10, 30 and 150 days of curing) remained lower (0.24 MPa instead of 0.325 MPa after 150 days of curing). This difference was mainly attributed to a weaker adhesion between wheat husk and the lime-based binder.

- The dry thermal conductivity measured for magnesia-based concretes was somewhat higher than the values recorded for lime-based ones and a difference between the two types of aggregates was noted (0.119 W/(m·K) for hemp hurd and 0.168 W/(m·K) for wheat husk). Compared to lime based concretes, higher compressive strengths were obtained for magnesia- based ones. This was particularly evident when wheat husks were used. In fact, a compressive strength of 2.35 MPa was obtained for magnesia wheat husk concrete following 30 days of curing, whereas the corresponding value of lime wheat husk concrete was 0.13 MPa. These results were explained by better compatibility between wheat husk aggregate and magnesia-based cement, leading to improved particle-binder adhesion. In particular, crystallization of cementitious phases was observed not only in the cement matrix but also inside wheat husk aggregates. In summary, not only a dense connected network was created between aggregates and the surrounding binder but a reinforcement of the skeletal structure of the highly porous aggregate was obtained which is considered the weakest link in concrete system in term of mechanical performances.

According to functional classification of lightweight concretes made by the RILEM committee, in consequence to the exceptionally high mechanical strength of the magnesia-based wheat husk concrete (2.35 MPa at 30 days), it could be used for structural-insulating blocks (compressive strength >2 MPa, density <1400 kg/m^3, dry thermal conductivity <0.3 W/(m·K).

According to the French professional rules developed for hemp concrete construction, the compressive strength of all agro-concrete are higher than the minimum threshold value for wall mixtures (i.e. 0.2 MPa). However, only the lime-based concretes had a low enough dry thermal conductivity (<0.1 W/(m·K)).

Nevertheless, the high mechanical strength of the magnesia-based ones provides a margin to further improve the thermal performance and eventually reach the requirements of the French Professional rules. Future work should thus be dedicated to optimize thermal and mechanical performances in function of the final application of the concrete material. To this aim, two main parameters should be considered: i) binder/aggregate mass ratio and ii) the compaction pressure used during the forming process.

Another important further development regarding the magnesia-based concretes is optimization of the curing conditions. In fact, the strength of these materials have the potential to be further improved through carbonation of the $Mg(OH)_2$ phase which is an important binder constituent. In particular, this phase can eventually react with atmospheric CO_2, forming various magnesium carbonate hydrates with a consequent strength gain. This step could also be necessary in order to improve the long-term stability of the material.

Considering the results obtained during the course of this work, it can be concluded that wheat husk is promising for use in bio based insulating materials possibly also for structural purposes. The magnesia-based binder was shown to be particularly interesting due to good binder-aggregate compatibility. The results are of high importance from an environmental point of view, not only because a recycling solution is proposed for wheat husk but also because a valid alternative to lime hemp concrete is given. In fact, the high availability of wheat husk should facilitate future developments of bio based alternatives to traditional insulation materials.

References

[1] E. Sassoni, S. Manzi, A. Motori, M. Montecchi, M. Canti, Novel sustainable hemp-based composites for application in the building industry: Physical, thermal and mechanical characterization, Energy Build. 77 (2014) 219–226. doi:10.1016/j.enbuild.2014.03.033.

[2] E. Sassoni, S. Manzi, A. Motori, M. Montecchi, M. Canti, Experimental study on the physical-mechanical durability of innovative hemp-based composites for the building industry, Energy Build. 104 (2015) 316–322. doi:10.1016/j.enbuild.2015.07.022.

[3] Buildings, (n.d.). https://www.iea.org/topics/energyefficiency/buildings/ (accessed November 30, 2019).

[4] N. Lechner, Heating, Cooling, Lighting: Sustainable Design Methods for Architects, n.d. https://books.google.it/books?hl=it&lr=&id=WjetCwAAQBAJ&oi=fnd&pg=PR11&ots=YNObFSPM65&sig=yrWv57SY2rF1SeVF4cIlnA8YER0&redir_esc=y#v=onepage&q&f=false (accessed November 27, 2019).

[5] G. Galli, A. Vallati, C. Recchiuti, R. de Lieto Vollaro, F. Botta, Passive cooling design options to improve thermal comfort in an Urban District of Rome, under hot summer conditions, Int. J. Eng. Technol. 5 (2013) 4495–4500.

[6] A. Madhumathi, M.C. Sundarraja, R. Shanthipriya, A comparative study of the thermal comfort of different building materials in madurai, Int. J. Earth Sci. Eng. 7 (2014) 1004–1018. doi:10.3844/ajeassp.2013.20.24.

[7] N. Khamporn, S. Chaiyapinunt, An investigation on the human thermal comfort from a glass window, Eng. J. 18 (2014) 25–43. doi:10.4186/ej.2014.18.1.25.

[8] B. Rodríguez-Soria, J. Domínguez-Hernández, J.M. Pérez-Bella, J.J. Del Coz-Díaz, Quantitative analysis of the divergence in energy losses allowed through building envelopes, Renew. Sustain. Energy Rev. 49 (2015) 1000–1008. doi:10.1016/j.rser.2015.05.002.

[9] R. De Lieto Vollaro, C. Guattari, L. Evangelisti, G. Battista, E. Carnielo, P. Gori, Building energy performance analysis: A case study, Energy Build. 87 (2015) 87–94. doi:10.1016/j.enbuild.2014.10.080.

[10] Directive 2010/31/EU of the European Parliament and of the Council of 19 May 2010 on the energy performance of building, (n.d.).

[11] Directive 2012/27/EU of the European Parliament and of the Council of 25 October 2012 on energy efficiency, amending Directives 2009/125/EC and 2010/30/EU and repealing Directives 2004/8/EC and 2006/32/EC, (n.d.). doi:10.3000/19770677.L_2012.315.eng.

[12] Building Thermal Insulation Market Analysis & Forecasts 2017-2027, (n.d.). https://www.visiongain.com/building-thermal-insulation-market-will-reach-25-1-billion-in-2017-according-to-brand-new-visiongain-report/ (accessed December 19, 2019).

[13] B.P. Jelle, Traditional, state-of-the-art and future thermal building insulation materials and solutions - Properties, requirements and possibilities, Energy Build. 43 (2011) 2549–2563. doi:10.1016/j.enbuild.2011.05.015.

[14] L.F. Liu, H.Q. Li, A. Lazzaretto, G. Manente, C.Y. Tong, Q. Bin Liu, N.P. Li, The development history and prospects of biomass-based insulation materials for buildings, Renew. Sustain. Energy Rev. 69 (2017) 912–932.

doi:10.1016/J.RSER.2016.11.140.
[15] C.C. Pavel, D.T. Blagoeva, Competitive landscape of the EU ' s insulation materials industry for energy-efficient buildings, Eur. Com. 2018. (2018) 1–14. doi:10.2760/251981.
[16] A.M. Papadopoulos, State of the art in thermal insulation materials and aims for future developments, Energy Build. 37 (2005) 77–86. doi:10.1016/j.enbuild.2004.05.006.
[17] K.H. Mo, U.J. Alengaram, M.Z. Jumaat, S.P. Yap, S.C. Lee, Green concrete partially comprised of farming waste residues: a review, J. Clean. Prod. 117 (2016) 122–138. doi:10.1016/J.JCLEPRO.2016.01.022.
[18] Project - IsoBio Project, (n.d.). http://isobioproject.com/project/ (accessed August 1, 2019).
[19] H. Binici, M. Eken, M. Dolaz, O. Aksogan, M. Kara, An environmentally friendly thermal insulation material from sunflower stalk, textile waste and stubble fibres, Constr. Build. Mater. 51 (2014) 24–33. doi:10.1016/j.conbuildmat.2013.10.038.
[20] J. Pinto, A. Paiva, H. Varum, A. Costa, D. Cruz, S. Pereira, L. Fernandes, P. Tavares, J. Agarwal, Corn ' s cob as a potential ecological thermal insulation material, Energy Build. 43 (2011) 1985–1990. doi:10.1016/j.enbuild.2011.04.004.
[21] K. Wei, C. Lv, M. Chen, X. Zhou, Z. Dai, D. Shen, Development and performance evaluation of a new thermal insulation material from rice straw using high frequency hot-pressing, Energy Build. 87 (2015) 116–122. doi:10.1016/j.enbuild.2014.11.026.
[22] I.C. Valverde, L.H. Castilla, D.F. Nuñez, E. Rodriguez-Senín, R. De La Mano Ferreira, Development of new insulation panels based on textile recycled fibers, Waste and Biomass Valorization. 4 (2013) 139–146. doi:10.1007/s12649-012-9124-8.
[23] A. Paiva, S. Pereira, A. Sá, D. Cruz, H. Varum, J. Pinto, A contribution to the thermal insulation performance characterization of corn cob particleboards, Energy Build. 45 (2012) 274–279. doi:10.1016/j.enbuild.2011.11.019.
[24] M. Viel, F. Collet, C. Lanos, Chemical and multi-physical characterization of agro-resources' by-product as a possible raw building material, Ind. Crops Prod. 120 (2018) 214–237. doi:10.1016/j.indcrop.2018.04.025.
[25] M.M. Gui, L. Tan, W. Ong, S. Chai, A. Silver, CO 2 Photocatalytic Reduction : Photocatalyst Choice and Product Selectivity Carbon monoxide Hydrogen ions, 2015. doi:10.1007/978-3-319-11906-9.
[26] Q. Yuan, J. Pump, R. Conrad, Straw application in paddy soil enhances methane production also from other carbon sources, Biogeosciences. 11 (2014) 237–246. doi:10.5194/bg-11-237-2014.
[27] S. Searle, C. Malins, A.S. Searle, C. Malins, Availability of cellulosic residues and wastes in the EU - International Council on Clean Transportation., Int. Counc. Clean Transp. White Pap. (2013). https://www.theicct.org/publications/availability-cellulosic-residues-and-wastes-eu.
[28] M.I. Tongwane, M.E. Moeletsi, A review of greenhouse gas emissions from the agriculture sector in Africa, Agric. Syst. 166 (2018) 124–134. doi:10.1016/J.AGSY.2018.08.011.
[29] M. Lawrence, A. Heath, P. Walker, Determining moisture levels in straw bale construction, Constr. Build. Mater. 23 (2009) 2763–2768.

doi:10.1016/j.conbuildmat.2009.03.011.
[30] A. Thomson, P. Walker, Durability characteristics of straw bales in building envelopes, Constr. Build. Mater. 68 (2014) 135–141. doi:10.1016/j.conbuildmat.2014.06.041.
[31] A. Bourdot, T. Moussa, A. Gacoin, C. Maalouf, P. Vazquez, C. Thomachot-Schneider, C. Bliard, A. Merabtine, M. Lachi, O. Douzane, H. Karaky, G. Polidori, Characterization of a hemp-based agro-material: Influence of starch ratio and hemp shive size on physical, mechanical, and hygrothermal properties, Energy Build. 153 (2017) 501–512. doi:10.1016/j.enbuild.2017.08.022.
[32] G. Balčiunas, S. Vejelis, S. Vaitkus, A. Kairyte, Physical properties and structure of composite made by using hemp hurds and different binding materials, in: Procedia Eng., Elsevier Ltd, 2013: pp. 159–166. doi:10.1016/j.proeng.2013.04.023.
[33] M. Lagouin, C. Magniont, P. Sénéchal, P. Moonen, J.E. Aubert, A. Laborel-préneron, Influence of types of binder and plant aggregates on hygrothermal and mechanical properties of vegetal concretes, Constr. Build. Mater. 222 (2019) 852–871. doi:10.1016/j.conbuildmat.2019.06.004.
[34] L. Qin, X. Gao, T. Chen, Recycling of raw rice husk to manufacture magnesium oxysulfate cement based lightweight building materials, J. Clean. Prod. 191 (2018) 220–232. doi:10.1016/j.jclepro.2018.04.238.
[35] T. Jami, D. Rawtani, Y.K. Agrawal, Hemp concrete: carbon-negative construction, Emerg. Mater. Res. 5 (2016) 240–247. doi:10.1680/jemmr.16.00122.
[36] S. Amziane, F. Collet, S. Report, R.T. Committee, Bio-aggregates Based Building Materials, 2017. doi:10.1007/978-94-024-1031-0.
[37] S. Amziane, Overview on biobased building material made with plant aggregate, Sustain. Constr. Mater. Technol. 2016–Augus (2016) 31–38. doi:10.21809/rilemtechlett.v1.9.
[38] J. Kline, L. Barcelo, Cement and CO 2, a victim of success!, in: IEEE Cem. Ind. Tech. Conf., 2012. doi:10.1109/CITCON.2012.6215687.
[39] H. Savastano, P.G. Warden, R.S.P. Coutts, Brazilian waste fibres as reinforcement for cement-based composites, Cem. Concr. Compos. 22 (2000) 379–384. doi:10.1016/S0958-9465(00)00034-2.
[40] L. Arnaud, Bio-aggregate-based Building Materials, 2013. doi:10.1002/9781118576809.
[41] A. Al-mohamadawi, K. Benhabib, R. Dheilly, A. Goullieux, Influence of lignocellulosic aggregate coating with paraffin wax on flax shive and cement-shive composite properties, Constr. Build. Mater. 102 (2016) 94–104. doi:10.1016/j.conbuildmat.2015.10.190.
[42] M. Khazma, A. Goullieux, R.M. Dheilly, A. Rougier, M. Quéneudec, Optimization of flax shive-cementitious composites : Impact of different aggregate treatments using linseed oil, Ind. Crop. Prod. 61 (2014) 442–452. doi:10.1016/j.indcrop.2014.07.041.
[43] M. Khazma, N. El Hajj, A. Goullieux, R.M. Dheilly, M. Queneudec, Influence of sucrose addition on the performance of a lignocellulosic composite with a cementious matrix, Compos. Part A Appl. Sci. Manuf. 39 (2008) 1901–1908. doi:10.1016/j.compositesa.2008.09.014.
[44] E. Aamr-Daya, T. Langlet, A. Benazzouk, M. Quéneudec, Feasibility study of lightweight cement composite containing flax by-product particles: Physico-

mechanical properties, Cem. Concr. Compos. 30 (2008) 957–963. doi:10.1016/j.cemconcomp.2008.06.002.
[45] N. Mostefai, R. Hamzaoui, A. Aw, H. Nouri, Microstructure and mechanical performance of modified hemp fibre and shiv mortars : Discovering the optimal formulation, Mater. Des. 84 (2015) 359–371. doi:10.1016/j.matdes.2015.06.102.
[46] F. Collet, S. Pretot, Thermal conductivity of hemp concretes: Variation with formulation, density and water content, Constr. Build. Mater. 65 (2014) 612–619. doi:10.1016/j.conbuildmat.2014.05.039.
[47] R. Walker, S. Pavia, R. Mitchell, Mechanical properties and durability of hemp-lime concretes, Constr. Build. Mater. 61 (2014) 340–348. doi:10.1016/j.conbuildmat.2014.02.065.
[48] A. Arizzi, G. Cultrone, M. Brümmer, H. Viles, A chemical , morphological and mineralogical study on the interaction between hemp hurds and aerial and natural hydraulic lime particles : Implications for mortar manufacturing, Constr. Build. Mater. 75 (2015) 375–384. doi:10.1016/j.conbuildmat.2014.11.026.
[49] P. Tronet, T. Lecompte, V. Picandet, C. Baley, Study of lime hemp concrete (LHC): Mix design , casting process and mechanical behaviour, 67 (2016) 60–72. doi:10.1016/j.cemconcomp.2015.12.004.
[50] S. Benfratello, C. Capitano, G. Peri, G. Rizzo, G. Scaccianoce, G. Sorrentino, Thermal and structural properties of a hemp – lime biocomposite, Constr. Build. Mater. 48 (2013) 745–754. doi:10.1016/j.conbuildmat.2013.07.096.
[51] Y. Diquélou, E. Gourlay, L. Arnaud, B. Kurek, Influence of binder characteristics on the setting and hardening of hemp lightweight concrete, Constr. Build. Mater. 112 (2016) 506–517. doi:10.1016/j.conbuildmat.2016.02.138.
[52] T.T. Nguyen, V. Picandet, P. Carre, T. Lecompte, S. Amziane, C. Baley, Effect of compaction on mechanical and thermal properties of hemp concrete, Eur. J. Environ. Civ. Eng. 14 (2010) 545–560. doi:10.1080/19648189.2010.9693246.
[53] F. Collet, J. Chamoin, S. Pretot, C. Lanos, Comparison of the hygric behaviour of three hemp concretes, Energy Build. 62 (2013) 294–303. doi:10.1016/j.enbuild.2013.03.010.
[54] F. Collet, M. Bart, L. Serres, J. Miriel, Porous structure and water vapour sorption of hemp-based materials, Constr. Build. Mater. 22 (2008) 1271–1280. doi:10.1016/J.CONBUILDMAT.2007.01.018.
[55] S. Elfordy, F. Lucas, F. Tancret, Y. Scudeller, L. Goudet, Mechanical and thermal properties of lime and hemp concrete (“hempcrete”) manufactured by a projection process, Constr. Build. Mater. 22 (2008) 2116–2123. doi:10.1016/j.conbuildmat.2007.07.016.
[56] T.T. Nguyen, V. Picandet, S. Amziane, C. Baley, Influence of compactness and hemp hurd characteristics on the mechanical properties of lime and hemp concrete, Eur. J. Environ. Civ. Eng. 13 (2009) 1039–1050. doi:10.1080/19648189.2009.9693171.
[57] A. Evrard, Transient hygrothermal behaviour of Lime-Hemp Materials, PhD Thesis. (2008). http://edoc.bib.ucl.ac.be:81/ETD-papier/submitted/Evrard_Arnaud.html.
[58] M. Sinka, P. Van den Heede, N. De Belie, D. Bajare, G. Sahmenko, A. Korjakins, Comparative life cycle assessment of magnesium binders as an

alternative for hemp concrete, Resour. Conserv. Recycl. 133 (2018) 288–299. doi:10.1016/j.resconrec.2018.02.024.
[59] R. Fernea, D.L. Manea, D.R. Tămas-Gavrea, I.C. Rosca, Hemp-clay building materials-An investigation on acoustic, thermal and mechanical properties, in: Procedia Manuf., Elsevier B.V., 2019: pp. 216–223. doi:10.1016/j.promfg.2019.02.205.
[60] B. Mazhoud, F. Collet, S. Pretot, C. Lanos, Mechanical properties of hemp-clay and hemp stabilized clay composites, Constr. Build. Mater. 155 (2017) 1126–1137. doi:10.1016/j.conbuildmat.2017.08.121.
[61] M. Degrave-Lemeurs, P. Glé, A. Hellouin de Menibus, Acoustical properties of hemp concretes for buildings thermal insulation: Application to clay and lime binders, Constr. Build. Mater. 160 (2018) 462–474. doi:10.1016/j.conbuildmat.2017.11.064.
[62] M. Brümmer, M.P. Sáez-Pérez, J.D. Suárez, Hemp-Clay Concretes for Environmental Building—Features that Attribute to Drying, Stabilization with Lime, Water Uptake and Mechanical Strength, in: Adv. Nat. Fibre Compos., Springer International Publishing, 2018: pp. 249–265. doi:10.1007/978-3-319-64641-1_21.
[63] R. Busbridge, R. Rhydwen, AN INVESTIGATION OF THE THERMAL PROPERTIES OF HEMP AND CLAY MONOLITHIC WALLS, in: Adv. Comput. Technol. Sch. Comput. Technol. 5th Annu. Conf. Univ. East London, 2010: pp. 163–170.
[64] L. Kidalova, E. Terpakova, N. Stevulova, MgO cement as suitable conventional binders replacement in hemp concrete, Pollack Period. 6 (2011) 115–122. doi:10.1556/Pollack.6.2011.3.11.
[65] R. Del Valle-Zermeño, J.E. Aubert, A. Laborel-Préneron, J. Formosa, J.M. Chimenos, Preliminary study of the mechanical and hygrothermal properties of hemp-magnesium phosphate cements, Constr. Build. Mater. 105 (2016) 62–68. doi:10.1016/j.conbuildmat.2015.12.081.
[66] D. Sinka, M., Sahmenko, G., Korjakins, A., Bajare, LIME-HEMP CONCRETE (LHC) ENHANCEMENT USING MAGNESIUM BASED BINDERS, in: RILEM (Ed.), Proc. 2nd Int. Conf. Bio-Based Build. Mater. ICBBM 2017., Clermont-Ferrand, France, 2017: pp. 238–245.
[67] M. Chabannes, E. Garcia-Diaz, L. Clerc, J. Bénézet, F. Becquart, Lime Hemp and Rice Husk- Based Concretes for Building Envelopes, 2018.
[68] M. Chabannes, F. Becquart, E. Garcia-Diaz, N.E. Abriak, L. Clerc, Experimental investigation of the shear behaviour of hemp and rice husk-based concretes using triaxial compression, Constr. Build. Mater. 143 (2017) 621–632. doi:10.1016/j.conbuildmat.2017.03.148.
[69] M. Chabannes, J.C. Bénézet, L. Clerc, E. Garcia-Diaz, Use of raw rice husk as natural aggregate in a lightweight insulating concrete: An innovative application, Constr. Build. Mater. 70 (2014) 428–438. doi:10.1016/j.conbuildmat.2014.07.025.
[70] M. Chabannes, E. Garcia-Diaz, L. Clerc, J.C. Bénézet, Effect of curing conditions and Ca(OH)2-treated aggregates on mechanical properties of rice husk and hemp concretes using a lime-based binder, Constr. Build. Mater. 102 (2016) 821–833. doi:10.1016/j.conbuildmat.2015.10.206.
[71] M. Chabannes, E. Garcia-Diaz, L. Clerc, J.-C.C. Bénézet, Studying the hardening and mechanical performances of rice husk and hemp-based building materials cured under natural and accelerated carbonation, Constr. Build.

Mater. 94 (2015) 105–115. doi:10.1016/J.CONBUILDMAT.2015.06.032.
[72] C.M. Helepciuc, M. Barbuta, A.A. Serbanoiu, Characterization of a lightweight concrete with sunflower aggregates, in: Procedia Manuf., Elsevier B.V., 2018: pp. 154–159. doi:10.1016/j.promfg.2018.03.024.
[73] M. Chabannes, V. Nozahic, S. Amziane, Design and multi-physical properties of a new insulating concrete using sunflower stem aggregates and eco-friendly binders, Mater. Struct. Constr. 48 (2015) 1815–1829. doi:10.1617/s11527-014-0276-9.
[74] V. Nozahic, S. Amziane, Influence of sunflower aggregates surface treatments on physical properties and adhesion with a mineral binder, Compos. Part A Appl. Sci. Manuf. 43 (2012) 1837–1849. doi:10.1016/j.compositesa.2012.07.011.
[75] V. Nozahic, S. Amziane, G. Torrent, K. Saïdi, H. De Baynast, Design of green concrete made of plant-derived aggregates and a pumice-lime binder, Cem. Concr. Compos. 34 (2012) 231–241. doi:10.1016/j.cemconcomp.2011.09.002.
[76] J. Pinto, B. Vieira, H. Pereira, C. Jacinto, P. Vilela, A. Paiva, S. Pereira, V.M.C.F. Cunha, H. Varum, Corn cob lightweight concrete for non-structural applications, Constr. Build. Mater. 34 (2012) 346–351. doi:10.1016/j.conbuildmat.2012.02.043.
[77] H. Phung, T-A.; Le Guern, M.; Boutouil, M.; Louahlia, ICBBM 2017. Proceedings of the 2nd International Conference on Bio-Based Building Materials, in: Mech. Therm. Perform. COB Mater., 2017: pp. 166–172.
[78] M. Rahim, O. Douzane, A.D. Tran Le, G. Promis, T. Langlet, A.D.T. Le, G. Promis, T. Langlet, A.D. Tran Le, G. Promis, T. Langlet, Characterization and comparison of hygric properties of rape straw concrete and hemp concrete, Constr. Build. Mater. 102 (2016) 679–687. doi:10.1016/j.conbuildmat.2015.11.021.
[79] M. Rahim, O. Douzane, A.D. Tran Le, G. Promis, T. Langlet, A.D.T. Le, G. Promis, T. Langlet, Experimental investigation of hygrothermal behavior of two bio-based building envelopes, Energy Build. 139 (2017) 608–615. doi:10.1016/j.enbuild.2017.01.058.
[80] I.O. Miron, D.L. Manea, D.M. Cantor, C. Aciu, Organic thermal insulation based on wheat straw, Procedia Eng. 181 (2017) 674–681. doi:10.1016/j.proeng.2017.02.449.
[81] L. Liu, S. Zou, H. Li, L. Deng, C. Bai, X. Zhang, S. Wang, N. Li, Experimental physical properties of an eco-friendly bio-insulation material based on wheat straw for buildings, Energy Build. 201 (2019) 19–36. doi:10.1016/j.enbuild.2019.07.037.
[82] T. Ashour, H. Wieland, H. Georg, F.J. Bockisch, W. Wu, The influence of natural reinforcement fibres on insulation values of earth plaster for straw bale buildings, Mater. Des. 31 (2010) 4676–4685. doi:10.1016/j.matdes.2010.05.026.
[83] Construire en chanvre - Règles professionnelles d'exécution, 2012. https://librairie.sebtp.com/construire-en-chanvre-règles-professionnelles-dexécution-edition-2012 (accessed December 11, 2019).
[84] S.A.L. AMZIANE, Les bétons de granulats d'origine végétale, Lavoisier, France, 2013. https://www.lavoisier.fr/livre/genie-civil-BTP/les-betons-de-granulats-d-origine-vegetale/amziane/descriptif-9782746238091 (accessed December 11, 2019).
[85] P. Ronchetti, THE BARRIERS TO THE MAINSTREAMING OF LIME-

HEMP: A SYSTEMIC APPROACH, 2007.
[86] K. Miled, O. Limam, Effective thermal conductivity of foam concretes: Homogenization schemes vs experimental data and FEM simulations, Mech. Res. Commun. 76 (2016) 96–100. doi:10.1016/j.mechrescom.2016.07.004.
[87] M. Pervaiz, M.M. Sain, Carbon storage potential in natural fiber composites, Resour. Conserv. Recycl. 39 (2003) 325–340. doi:10.1016/S0921-3449(02)00173-8.
[88] K. Ip, A. Miller, Life cycle greenhouse gas emissions of hemp-lime wall constructions in the UK, Resour. Conserv. Recycl. 69 (2012) 1–9. doi:10.1016/j.resconrec.2012.09.001.
[89] S. Pretot, F. Collet, C. Garnier, Life cycle assessment of a hemp concrete wall: Impact of thickness and coating, Build. Environ. 72 (2014) 223–231. doi:10.1016/j.buildenv.2013.11.010.
[90] A. Arrigoni, R. Pelosato, P. Melià, G. Ruggieri, S. Sabbadini, G. Dotelli, Life cycle assessment of natural building materials: the role of carbonation, mixture components and transport in the environmental impacts of hempcrete blocks, J. Clean. Prod. 149 (2017) 1051–1061. doi:10.1016/j.jclepro.2017.02.161.
[91] C. Maalouf, A.D.T. Le, S.B. Umurigirwa, M. Lachi, O. Douzane, Study of hygrothermal behaviour of a hemp concrete building envelope under summer conditions in France, Energy Build. 77 (2014) 48–57. doi:10.1016/j.enbuild.2014.03.040.
[92] M. Rahim, O. Douzane, A.D. Tran Le, G. Promis, B. Laidoudi, A. Crigny, B. Dupre, T. Langlet, Characterization of flax lime and hemp lime concretes: Hygric properties and moisture buffer capacity, Energy Build. 88 (2015) 91–99. doi:10.1016/j.enbuild.2014.11.043.
[93] V. Cérézo, Propriétés mécaniques, thermiques et acoustiques d'un matériau à base de particules végétales : approche expérimentale et modélisation théorique, Thèse Dr. (2005) 247. http://theses.insa-lyon.fr/publication/2005isal0037/these.pdf.
[94] O. Kinnane, A. Reilly, J. Grimes, S. Pavia, R. Walker, Acoustic absorption of hemp-lime construction, Constr. Build. Mater. 122 (2016) 674–682. doi:10.1016/j.conbuildmat.2016.06.106.
[95] L. Arnaud, E. Gourlay, Experimental study of parameters influencing mechanical properties of hemp concretes, Constr. Build. Mater. 28 (2012) 50–56. doi:10.1016/j.conbuildmat.2011.07.052.
[96] R. Walker, A Study of the Properties of Lime-Hemp Concrete with Pozzolans, 2013.
[97] P. Glouannec, F. Collet, C. Lanos, P. Mounanga, T. Pierre, P. Poullain, S. Pretot, J. Chamoin, A. Zaknoune, Propriétés physiques de bétons de chanvre, Matériaux Tech. 99 (2011) 657–665. doi:10.1051/mattech/2011047.
[98] P. Monreal, L.B. Mboumba-Mamboundou, R.M. Dheilly, M. Quéneudec, Effects of aggregate coating on the hygral properties of lignocellulosic composites, Cem. Concr. Compos. 33 (2011) 301–308. doi:10.1016/j.cemconcomp.2010.10.017.
[99] E.P. Aigbomian, M. Fan, Development of wood-crete from treated sawdust, Constr. Build. Mater. 52 (2014) 353–360. doi:10.1016/j.conbuildmat.2013.11.025.
[100] M. Le Troëdec, A. Rachini, C. Peyratout, S. Rossignol, E. Max, O. Kaftan, A. Fery, A. Smith, Influence of chemical treatments on adhesion properties of

hemp fibres, J. Colloid Interface Sci. 356 (2011) 303–310. doi:10.1016/j.jcis.2010.12.066.
[101] A. Peschard, A. Govin, P. Grosseau, B. Guilhot, R. Guyonnet, Effect of polysaccharides on the hydration of cement paste at early ages, Cem. Concr. Res. 34 (2004) 2153–2158. doi:10.1016/j.cemconres.2004.04.001.
[102] A. Peschard, A. Govin, J. Pourchez, E. Fredon, L. Bertrand, S. Maximilien, B. Guilhot, Effect of polysaccharides on the hydration of cement suspension, J. Eur. Ceram. Soc. 26 (2006) 1439–1445. doi:10.1016/j.jeurceramsoc.2005.02.005.
[103] Food and Agriculture Organization of the United Nations, GIEWS Crop Prospects and Food Situation, 2018.
[104] D. Kiš, N. Jovičić, A. Matin, S. Kalambura, S. Vila, S. Guberac, Energy value of agricultural spelt residue (Triticum spelta L.) – forgotten cultures, Teh. Vjesn. - Tech. Gaz. 24 (2017) 369–373. doi:10.17559/tv-20170406124003.
[105] T. Brlek, M. Bodroza-Solarov, D. Vukmirovic, R. Colovic, J. Vuckovic, J. Levic, Utilization of spelt wheat hull as a renewable energy source by pelleting, Bulg. J. Agric. Sci. 18 (2012) 752–758.
[106] V. Sharma, P.K. Rathore, A. Sharma, Soil Stabilization by Using Wheat Husk Ash, 5 (2018) 31–35.
[107] J. Cui, H. Sun, Z. Luo, J. Sun, Z. Wen, Preparation of low surface area SiO2 microsphere from wheat husk ash with a facile precipitation process, Mater. Lett. 156 (2015) 42–45. doi:10.1016/J.MATLET.2015.04.134.
[108] P. Terzioglu, S. Yucel, T.M. Rababah, D. Özçimen, Characterization of wheat hull and wheat hull ash as a potential source of sio2, BioResources. 8 (2013) 4406–4420. doi:10.15376/biores.8.3.4406-4420.
[109] A.K. Bledzki, A.A. Mamun, J. Volk, Physical, chemical and surface properties of wheat husk, rye husk and soft wood and their polypropylene composites, Compos. Part A Appl. Sci. Manuf. 41 (2010) 480–488. doi:10.1016/j.compositesa.2009.12.004.
[110] T.P.T. Tran, J.C. Bénézet, A. Bergeret, A.K. Bledzki, A.A. Mamun, J. Volk, Rice and Einkorn wheat husks reinforced poly(lactic acid) (PLA) biocomposites: Effects of alkaline and silane surface treatments of husks, Ind. Crops Prod. 58 (2014) 111–124. doi:10.1016/j.indcrop.2014.04.012.
[111] Time to get acquainted with the industrial hemp revolution in Europe, (n.d.). https://www.healtheuropa.eu/industrial-hemp-revolution/92912/ (accessed February 11, 2020).
[112] "It saved our business": Italy's farmers turn low into high with cannabis | World news | The Guardian, (n.d.). https://www.theguardian.com/world/2018/aug/30/it-saved-our-business-italy-farmers-turn-to-cannabis-hemp (accessed January 21, 2020).
[113] Bjorn Berge, The Ecology of Building Materials, 2009. https://books.google.it/books?hl=fr&lr=&id=LswsBgAAQBAJ&oi=fnd&pg=PR2&ots=ij898cvdyF&sig=h-9IcrszObHKv-9litvHfjSNjIM&redir_esc=y#v=onepage&q&f=false (accessed January 1, 2020).
[114] J. Válek, E. Van Halem, A. Viani, M. Pérez-Estébanez, R. Ševčík, P. Šašek, Determination of optimal burning temperature ranges for production of natural hydraulic limes, Constr. Build. Mater. 66 (2014) 771–780. doi:10.1016/j.conbuildmat.2014.06.015.
[115] Ecobati, Tradical PF70 - liant de chaux aérienne pour dégrossir, (n.d.).

[116] S.A. Walling, J.L. Provis, Magnesia-Based Cements: A Journey of 150 Years, and Cements for the Future?, Chem. Rev. 116 (2016) 4170–4204. doi:10.1021/acs.chemrev.5b00463.
[117] X. Zhou, Z. Li, Light-weight wood-magnesium oxychloride cement composite building products made by extrusion, Constr. Build. Mater. 27 (2012) 382–389. doi:10.1016/j.conbuildmat.2011.07.033.
[118] Ł. Smakosz, J. Tejchman, Evaluation of strength, deformability and failure mode of composite structural insulated panels, Mater. Des. 54 (2014) 1068–1082. doi:10.1016/j.matdes.2013.09.032.
[119] T.A. Plekhanova, J. Keriene, A. Gailius, G.I. Yakovlev, Structural, physical and mechanical properties of modified wood-magnesia composite, Constr. Build. Mater. 21 (2007) 1833–1838. doi:10.1016/j.conbuildmat.2006.06.029.
[120] L. Ning, C. Bing, Experimental investigation concrete using magnesium phosphate cement, fly ash, and rape stalk, J. Mater. Civ. Eng. 28 (2016). doi:10.1061/(ASCE)MT.1943-5533.0001459.
[121] S.O. Amiandamhen, M. Meincken, L. Tyhoda, Magnesium based phosphate cement binder for composite panels: A response surface methodology for optimisation of processing variables in boards produced from agricultural and wood processing industrial residues, Ind. Crops Prod. 94 (2016) 746–754. doi:10.1016/j.indcrop.2016.09.051.
[122] P.K. Donahue, M.D. Aro, Durable phosphate-bonded natural fiber composite products, Constr. Build. Mater. 24 (2010) 215–219. doi:10.1016/j.conbuildmat.2007.05.015.
[123] B. Na, Z. Wang, H. Wang, X. Lu, WOOD-cement compatibility review, Wood Res. 59 (2014) 813–825.
[124] L. Wang, I.K.M. Yu, D.C.W. Tsang, K. Yu, S. Li, C. Sun Poon, J.G. Dai, Upcycling wood waste into fibre-reinforced magnesium phosphate cement particleboards, Constr. Build. Mater. 159 (2018) 54–63. doi:10.1016/j.conbuildmat.2017.10.107.
[125] L. Wang, I.K.M. Yu, D.C.W. Tsang, S. Li, J. shan Li, C.S. Poon, Y.S. Wang, J.G. Dai, Transforming wood waste into water-resistant magnesia-phosphate cement particleboard modified by alumina and red mud, J. Clean. Prod. 168 (2017) 452–462. doi:10.1016/j.jclepro.2017.09.038.
[126] M. Liska, A. Al-Tabbaa, Ultra-green construction: Reactive MgO masonry products, in: Proc. Inst. Civ. Eng. Waste Resour. Manag., 2009: pp. 185–196. doi:10.1680/warm.2009.162.4.185.
[127] Report on Critical Raw Materials for the Eu Critical Raw Materials Profiles, ad-hoc Working group on defining critical raw materials, 2014.
[128] U.S. Geological Survey, Mineral Commodity Summaries 2015 Mineral Commodity Summaries 2015, US Geol. Surv. (2015) 196. doi:10.3133/70140094.
[129] J. Green, Calcination of precipitated Mg(OH)2 to active MgO in the production of refractory and chemical grade MgO, J. Mater. Sci. 18 (1983) 637–651. doi:10.1007/BF00745561.
[130] Y. Kotera, T. Saito, M. Terada, Crystal Growth of Magnesium Oxide Prepared by the Thermal Decomposition of Magnesium Hydroxide, Bull. Chem. Soc. Jpn. 36 (1963) 195–199. doi:10.1246/bcsj.36.195.
[131] C.A. Strydom, E.M. Van Der Merwe, M.E. Aphane, The effect of calcining conditions on the rehydration of dead burnt magnesium oxide using magnesium acetate as a hydrating agent, J. Therm. Anal. Calorim. 80 (2005)

659–662. doi:10.1007/s10973-005-0710-x.
[132] High Purity Light Burned Magnesium Oxide (MgO) Products and Applications | Martin Marietta Magnesia Specialties, LLC, (n.d.). https://magnesiaspecialties.com/light-burned-magnesium-oxide/ (accessed January 1, 2020).
[133] M. Liska, A. Al-Tabbaa, K. Carter, J. Fifield, Scaled-up commercial production of reactive magnesium cement pressed masonry units. Part I: Production, Proc. Inst. Civ. Eng. - Constr. Mater. 165 (2012) 211–223. doi:10.1680/coma.10.00032.
[134] X. Zeng, H. Yu, C. Wu, An Overview of Study on Basic Magnesium Sulfate Cement and Concrete in China (2012–2019), KSCE J. Civ. Eng. 23 (2019) 4445–4453. doi:10.1007/s12205-019-0199-7.
[135] T. Runčevski, C. Wu, H. Yu, B. Yang, R.E. Dinnebier, Structural characterization of a new magnesium oxysulfate hydrate cement phase and its surface reactions with atmospheric carbon dioxide, J. Am. Ceram. Soc. 96 (2013) 3609–3616. doi:10.1111/jace.12556.
[136] N. Wang, H. Yu, W. Bi, Y. Tan, N. Zhang, C. Wu, H. Ma, S. Hua, Effects of sodium citrate and citric acid on the properties of magnesium oxysulfate cement, Constr. Build. Mater. 169 (2018) 697–704. doi:10.1016/j.conbuildmat.2018.02.208.
[137] C. Wu, H. Zhang, W. Zhang, H. Li, S. Xing, W. Chen, Water Resistance of Basic Magnesium Sulfate Cement, MATEC Web Conf. 67 (2016). doi:10.1051/matecconf/20166707008.
[138] C. Wu, H. Zhang, H. Yu, Preparation and properties of modified magnesium oxysulfate cement derived from waste sulfuric acid, Adv. Cem. Res. 28 (2016) 178–188. doi:10.1680/jadcr.15.00011.
[139] C. Wu, W. Chen, H. Zhang, H. Yu, W. Zhang, N. Jiang, L. Liu, The hydration mechanism and performance of Modified magnesium oxysulfate cement by tartaric acid, Constr. Build. Mater. 144 (2017) 516–524. doi:10.1016/j.conbuildmat.2017.03.222.
[140] L. Qin, X. Gao, W. Li, H. Ye, Modification of magnesium oxysulfate cement by incorporating weak acids, J. Mater. Civ. Eng. 30 (2018). doi:10.1061/(ASCE)MT.1943-5533.0002418.
[141] D.T. Beruto, F. Barberis, R. Botter, Calcium carbonate binding mechanisms in the setting of calcium and calcium – magnesium putty-limes, 6 (2005) 253–260. doi:10.1016/j.culher.2005.06.003.
[142] O. Cazalla, R.-N. C, S. E, Cultrone G., C. Rodriguez-Navarro, E. Sebastian, G. Cultrone, M.J. De la Torre, Aging of Lime Putty: Effects on Traditional Lime Mortar Carbonation, J. Am. Ceram. Soc. 76 (2002) 1070–1076. doi:10.1111/j.1151-2916.2000.tb01332.x.
[143] B.A. Silva, A.P. Ferreira Pinto, A. Gomes, Influence of natural hydraulic lime content on the properties of aerial lime-based mortars, Constr. Build. Mater. 72 (2014) 208–218. doi:10.1016/j.conbuildmat.2014.09.010.
[144] M. CANTI, BINDER FOR MANUFACTURING OF CONCRETE OR LAMINATED PRODUCTS, (2013). https://patentscope.wipo.int/search/en/detail.jsf?docId=WO2013061182 (accessed September 17, 2019).
[145] S. Amziane, F. Collet, M. Lawrence, C. Magniont, V. Picandet, M. Sonebi, Recommendation of the RILEM TC 236-BBM: characterisation testing of hemp shiv to determine the initial water content, water absorption, dry density,

particle size distribution and thermal conductivity, Mater. Struct. Constr. 50 (2017) 1–11. doi:10.1617/s11527-017-1029-3.
[146] AFNOR, 2005. Norme XP U 44-163. Amendements organiques et supports de culture – Détermination du potentiel de minéralisation du carbone et de l'azote – Méthode d'incubation en conditions contrôlées. AFNOR, Paris., (n.d.).
[147] R.H. Van Soest, P.J.; Wine, Use of detergents in the analysis of fibrous feeds. IV. Determination of plant cell-wall constituents, J. Assoc. Off. Anal. Chem. (1967) 50–55.
[148] J.L. Linères, M.; Djakovitch, Caractérisation de la stabilité biologique des apports organiques par l'analyse biochimique, J. Decroux, J.C. Ignazi (Eds.), Quatrième Journées Terres Cinquième Forum La Fertil. Raison. GEMAS-COMIFER, Paris. (1993).
[149] J. Page, M. Sonebi, S. Amziane, Design and multi-physical properties of a new hybrid hemp-flax composite material, Constr. Build. Mater. 139 (2017) 502–512. doi:10.1016/j.conbuildmat.2016.12.037.
[150] J.H. Blackwell, RADIAL-AXIAL HEAT FLOW IN REGIONS BOUNDED INTERNALLY BY CIRCULAR CYLINDERS, Can. J. Phys. 31 (1953) 472–479. doi:10.1139/p53-046.
[151] H.S. Carslaw, J.C. Jaeger, Conduction of Heat in Solids, Oxford University Press, 1959.
[152] C. Rode, Moisture Buffering of Building Materials Department of Civil Engineering Technical University of Denmark, 2005.
[153] M. Lassinantti Gualtieri, M. Romagnoli, P. Miselli, M. Cannio, A.F. Gualtieri, M. Lassinantti, M. Romagnoli, P. Miselli, M. Cannio, A.F. Gualtieri, Full quantitative phase analysis of hydrated lime using the Rietveld method, Cem. Concr. Res. 42 (2012) 1273–1279. doi:10.1016/j.cemconres.2012.05.016.
[154] Y. Jang, K. Li, An all-natural for bonding wood, JAOCS, J. Am. Oil Chem. Soc. 92 (2015) 431–438. doi:10.1007/s11746-015-2610-y.
[155] B.H. Toby, EXPGUI, a graphical user interface for GSAS, J. Appl. Crystallogr. 34 (2001) 210–213. doi:10.1107/S0021889801002242.
[156] A. Larson, R.V.D.-L.A.N.L.R. LAUR, Generalized structure analysis system (GSAS), (1994).
[157] N. Ishizawa, T. Miyata, I. Minato, F. Marumo, S. Iwai, A structural investigation of α-Al 2 O 3 at 2170 K , Acta Crystallogr. Sect. B Struct. Crystallogr. Cryst. Chem. 36 (1980) 228–230. doi:10.1107/s0567740880002981.
[158] O. Chaix-Pluchery, J. Pannetier, J. Bouillot, J.C. Niepce, Structural prereactional transformations in Ca(OH)2, J. Solid State Chem. 67 (1987) 225–234. doi:10.1016/0022-4596(87)90358-6.
[159] R.M. Hazen, Effects of temperature and pressure on the cell dimension and X-ray temperature factors of periclase, Am. Mineral. 61 (1976) 266–271. doi:10.1130/micro4-p263.
[160] F. Zigan, R.R. Monatshefte, Neutronenbeugungsmessungen am brucit, Neues Jahrb. Für Mineral. 4 (1967) 137–143.
[161] W.Z. Wooster, U. 1936, On the Crystal Structure of Gypsum, CaSO4· 2H2O, Zeitschrift Fuer Krist. Krist. Krist. Krist. 94 (1936) 375–396. https://www.degruyter.com/view/j/zkri.1936.94.issue-1-6/zkri.1936.94.1.375/zkri.1936.94.1.375.xml (accessed December 10, 2019).
[162] A.F. Gualtieri, Accuracy of XRPD QPA using the combined Rietveld-RIR method, J. Appl. Crystallogr. 33 (2000) 267–278.

doi:10.1107/S002188989901643X.
[163] S.J.L. I.C. Madsen, N.V.Y. Scarlett, Quantitative Phase Analysis, in: R.E. Dinnebier, B. (Eds.), Powder Diffraction, Theory and Practice, Royal Society of Chemistry, Cambridge, UK, 2008. doi:10.1039/9781847558237.
[164] A. Shea, M. Lawrence, P. Walker, Hygrothermal performance of an experimental hemp-lime building, Constr. Build. Mater. 36 (2012) 270–275. doi:10.1016/j.conbuildmat.2012.04.123.
[165] D. Devices, Decagon Devices, KD2 pro Thermal Properties Analyzer. Operator's Manual, (2012) 68.
[166] M. Rahim, O. Douzane, A.D. Tran Le, T. Langlet, Effect of moisture and temperature on thermal properties of three bio-based materials, Constr. Build. Mater. 111 (2016) 119–127. doi:10.1016/j.conbuildmat.2016.02.061.
[167] S. Xu, J. Wang, Y. Sun, Effect of water binder ratio on the early hydration of natural hydraulic lime, Mater. Struct. 48 (2015) 3431–3441. doi:10.1617/s11527-014-0410-8.
[168] Y. Jiang, M. Lawrence, M.P. Ansell, A. Hussain, Cell wall microstructure, pore size distribution and absolute density of hemp shiv, R. Soc. Open Sci. 5 (2018). doi:10.1098/rsos.171945.
[169] Y. Diquélou, E. Gourlay, L. Arnaud, B. Kurek, Impact of hemp shiv on cement setting and hardening: Influence of the extracted components from the aggregates and study of the interfaces with the inorganic matrix, Cem. Concr. Compos. 55 (2015) 112–121. doi:10.1016/j.cemconcomp.2014.09.004.
[170] F. Xu, J. Yu, T. Tesso, F. Dowell, D. Wang, Qualitative and quantitative analysis of lignocellulosic biomass using infrared techniques: A mini-review, Appl. Energy. 104 (2013) 801–809. doi:10.1016/j.apenergy.2012.12.019.
[171] S. Ahmad, Y. Iqbal, R. Muhammad, Effects of coal and wheat husk additives on the physical, thermal and mechanical properties of clay bricks, Bol. La Soc. Esp. Ceram. Y Vidr. 56 (2017) 131–138. doi:10.1016/j.bsecv.2017.02.001.
[172] A.K. Bledzki, P. Franciszczak, A. Mamun, The utilization of biochemically modified microfibers from grain by-products as reinforcement for polypropylene biocomposite, Express Polym. Lett. 8 (2014) 767–778. doi:10.3144/expresspolymlett.2014.79.
[173] E. Escarnot, M. Aguedo, M. Paquot, Characterization of hemicellulosic fractions from spelt hull extracted by different methods, Carbohydr. Polym. 85 (2011) 419–428. doi:10.1016/j.carbpol.2011.03.005.
[174] S. Malherbe, T.E. Cloete, Lignocellulose biodegradation: Fundamentals and applications, Rev. Environ. Sci. Biotechnol. 1 (2002) 105–114. doi:10.1023/A:1020858910646.
[175] P. Kumar, D.M. Barrett, M.J. Delwiche, P. Stroeve, Methods for Pretreatment of Lignocellulosic Biomass for Efficient Hydrolysis and Biofuel Production, Ind. Eng. Chem. Res. 48 (2009) 3713–3729. doi:10.1021/ie801542g.
[176] H.M.N. Iqbal, I. Ahmed, M.A. Zia, M. Irfan, Purification and characterization of the kinetic parameters of cellulase produced from wheat straw by Trichoderma viride under SSF and its detergent compatibility, Adv. Biosci. Biotechnol. 2 (2011) 149–156. doi:10.4236/abb.2011.23024.
[177] S. V. Vassilev, D. Baxter, L.K. Andersen, C.G. Vassileva, T.J. Morgan, An overview of the organic and inorganic phase composition of biomass, Fuel. 94 (2012) 1–33. doi:10.1016/j.fuel.2011.09.030.
[178] L.T.D. Amar K. Mohanty, Manjusri Misra, Natural Fibers, Biopolymers, and Biocomposites, 2005. doi:10.1201/9780203508206.

[179] D. Sedan, C. Pagnoux, T. Chotard, A. Smith, D. Lejolly, V. Gloaguen, P. Krausz, Effect of calcium rich and alkaline solutions on the chemical behaviour of hemp fibres, J. Mater. Sci. 42 (2007) 9336–9342. doi:10.1007/s10853-007-1903-4.
[180] V. Picandet, Characterization of Plant-Based Aggregates, in: Bio-Aggregate-Based Build. Mater., John Wiley & Sons, Inc., Hoboken, NJ 07030 USA, 2013: pp. 27–74. doi:10.1002/9781118576809.ch2.
[181] P. Adapa, L. Tabil, Compression characteristics of selected ground agricultural biomass, Agric. Eng. XI (2009). http://www.cigrjournal.org/index.php/Ejounral/article/view/1347.
[182] A.J. Stamm, Density of Wood Substance, Adsorption by Wood, and Permeability of Wood, J. Phys. Chem. 33 (1928) 398–414. doi:10.1021/j150297a008.
[183] E. Chabi, A. Lecomte, E.C. Adjovi, A. Dieye, A. Merlin, Mix design method for plant aggregates concrete: Example of the rice husk, Constr. Build. Mater. 174 (2018) 233–243. doi:10.1016/j.conbuildmat.2018.04.097.
[184] NF P75-101 - Octobre 1983, (n.d.). https://www.boutique.afnor.org/norme/nf-p75-101/isolants-thermiques-destines-au-batiment-definition/article/692898/fa018774 (accessed December 7, 2019).
[185] M.K. Habibi, L.H. Tam, D. Lau, Y. Lu, Viscoelastic damping behavior of structural bamboo material and its microstructural origins, Mech. Mater. 97 (2016) 184–198. doi:10.1016/j.mechmat.2016.03.002.
[186] L.J. Gibson, The hierarchical structure and mechanics of plant materials, J. R. Soc. Interface. 9 (2012) 2749–2766. doi:10.1098/rsif.2012.0341.
[187] A. Govin, A. Peschard, E. Fredon, R. Guyonnet, New insights into wood and cement interaction, Holzforschung. 59 (2005) 330–335. doi:10.1515/HF.2005.054.
[188] F.C. Jorge, C. Pereira, J.M.F. Ferreira, Wood-cement composites: A review, Holz Als Roh - Und Werkst. 62 (2004) 370–377. doi:10.1007/s00107-004-0501-2.
[189] G. Vaickelionis, R. Vaickelioniene, Cement hydration in the presence of wood extractives and pozzolan mineral additives, Ceram. - Silikaty. 50 (2006) 115–122.
[190] M.C. Garci Juenger, H.M. Jennings, New insights into the effects of sugar on the hydration and microstructure of cement pastes, Cem. Concr. Res. 32 (2002) 393–399. doi:10.1016/S0008-8846(01)00689-5.
[191] N.L. Thomas, J.D. Birchall, The retarding action of sugars on cement hydration, Cem. Concr. Res. 13 (1983) 830–842. doi:10.1016/0008-8846(83)90084-4.
[192] J. Wei, C. Meyer, Degradation mechanisms of natural fiber in the matrix of cement composites, Cem. Concr. Res. 73 (2015) 1–16. doi:10.1016/j.cemconres.2015.02.019.
[193] C. Magniont, G. Escadeillas, M. Coutand, C. Oms-Multon, Use of plant aggregates in building ecomaterials, in: Eur. J. Environ. Civ. Eng., 2012. doi:10.1080/19648189.2012.682452.
[194] M.G. Margalha, A.S. Silva, M.D.R. Veiga, J. De Brito, R.J. Ball, G.C. Allen, Microstructural changes of lime putty during aging, J. Mater. Civ. Eng. 25 (2013) 1524–1532. doi:10.1061/(ASCE)MT.1943-5533.0000687.
[195] G. Mascolo, M.C. Mascolo, A. Vitale, O. Marino, Microstructure evolution of lime putty upon aging, J. Cryst. Growth. 312 (2010) 2363–2368.

doi:10.1016/j.jcrysgro.2010.05.020.
[196] A. Arizzi, R. Hendrickx, G. Cultrone, K. Van Balen, Diferencias en las propiedades reológicas de suspensiones de cal calcítica y dolomítica: Influencia de las características de las partículas e implicaciones prácticas en la fabricación de morteros de cal, Mater. Constr. 62 (2012) 231–250. doi:10.3989/mc.2011.00311.
[197] R.S. Boynton, Chemistry and technology of lime and limestone, Wiley, 1980.
[198] A.F. Gualtieri, A. Viani, C. Montanari, Quantitative phase analysis of hydraulic limes using the Rietveld method, Cem. Concr. Res. 36 (2006) 401–406. doi:10.1016/j.cemconres.2005.02.001.
[199] M. Carbonaro, A. Nucara, Secondary structure of food proteins by Fourier transform spectroscopy in the mid-infrared region, Amino Acids. 38 (2010) 679–690. doi:10.1007/s00726-009-0274-3.
[200] E. Pretsch, P. (Philippe) Bühlmann, M. Badertscher, Structure determination of organic compounds : tables of spectral data., Springer, 2009.
[201] M. Casas-Cabanas, M.R. Palacín, J. Rodríguez-Carvajal, Microstructural analysis of nickel hydroxide: Anisotropic size versus stacking faults, Powder Diffr. 20 (2005) 334–344. doi:10.1154/1.2137340.
[202] A. V. Radha, P.V. Kamath, G.N. Subbanna, Disorder in layered hydroxides: Synthesis and DIFFaX simulation studies of Mg(OH)2, Mater. Res. Bull. 38 (2003) 731–740. doi:10.1016/S0025-5408(03)00070-9.
[203] S. Bette, B. Hinrichsen, D. Pfister, R.E. Dinnebier, A routine for the determination of the microstructure of stacking-faulted nickel cobalt aluminium hydroxide precursors for lithium nickel cobalt aluminium oxide battery materials Microstructure determination for NCA precursors, J. Appl. Crystallogr. 53 (2020) 76–87. doi:10.1107/S1600576719016212.
[204] C. Wu, H. Yu, H. Zhang, J. Dong, J. Wen, Y. Tan, Effects of phosphoric acid and phosphates on magnesium oxysulfate cement, Mater. Struct. Constr. 48 (2015) 907–917. doi:10.1617/s11527-013-0202-6.
[205] O. Fruhwirth, G.W. Herzog, I. Hollerer, A. Rachetti, Dissolution and hydration kinetics of MgO, Surf. Technol. 24 (1985) 301–317. doi:10.1016/0376-4583(85)90080-9.
[206] R.A. Wogelius, K. Refson, D.G. Fraser, G.W. Grime, J.P. Goff, Periclase surface hydroxylation during dissolution, Geochim. Cosmochim. Acta. 59 (1995) 1875–1881. doi:10.1016/0016-7037(95)00070-G.
[207] L.F. Amaral, I.R. Oliveira, R. Salomão, E. Frollini, V.C. Pandolfelli, Temperature and common-ion effect on magnesium oxide (MgO) hydration, Ceram. Int. 36 (2010) 1047–1054. doi:10.1016/j.ceramint.2009.12.009.
[208] K.P. Matabola, E.M. van der Merwe, C.A. Strydom, F.J.W. Labuschagne, The influence of hydrating agents on the hydration of industrial magnesium oxide, J. Chem. Technol. Biotechnol. 85 (2010) 1569–1574. doi:10.1002/jctb.2467.
[209] S.D. Rocha, M.B. Mansur, V.S. Ciminelli, Kinetics and mechanistic analysis of caustic magnesia hydration, J. Chem. Technol. Biotechnol. 79 (2004) 816–821. doi:10.1002/jctb.1038.
[210] Z. Xing, L. Bai, Y. Ma, D. Wang, M. Li, Mechanism of magnesium oxide hydration based on the multi-rate model, Materials (Basel). 11 (2018). doi:10.3390/ma11101835.
[211] M. Pannach, S. Bette, D. Freyer, Solubility Equilibria in the System Mg(OH)2-MgCl2-H2O from 298 to 393 K, J. Chem. Eng. Data. 62 (2017) 1384–1396. doi:10.1021/acs.jced.6b00928.

[212] J. Jiang, J. Chen, Y.L. Xiong, Structural and emulsifying properties of soy protein isolate subjected to acid and alkaline pH-shifting processes, J. Agric. Food Chem. 57 (2009) 7576–7583. doi:10.1021/jf901585n.
[213] O.S. Pokrovsky, J. Schott, Experimental study of brucite dissolution and precipitation in aqueous solutions: Surface speciation and chemical affinity control, Geochim. Cosmochim. Acta. 68 (2004) 31–45. doi:10.1016/S0016-7037(03)00238-2.
[214] R. Walker, S. Pavia, Impact of water retainers in the strength , drying and setting of lime hemp concrete, (2013).
[215] C. Niyigena, S. Amziane, A. Chateauneuf, L. Arnaud, L. Bessette, F. Collet, C. Lanos, G. Escadeillas, M. Lawrence, C. Magniont, S. Marceau, S. Pavia, U. Peter, V. Picandet, M. Sonebi, P. Walker, Variability of the mechanical properties of hemp concrete, Mater. Today Commun. 7 (2016) 122–133. doi:10.1016/j.mtcomm.2016.03.003.
[216] R.S.P. Coutts, P. Kightly, Bonding in wood fibre-cement composites, J. Mater. Sci. 19 (1984) 3355–3359. doi:10.1007/BF00549827.
[217] Z.G. Li, Z.S. Ji, L.L. Jiang, S.W. Yu, Effect of additives on the properties of magnesium oxysulfate cement, J. Intell. Fuzzy Syst. 33 (2017) 3021–3025. doi:10.3233/JIFS-169353.
[218] C. Wu, C. Chen, H. Zhang, Y. Tan, H. Yu, Preparation of magnesium oxysulfate cement using magnesium-rich byproducts from the production of lithium carbonate from salt lakes, Constr. Build. Mater. 172 (2018) 597–607. doi:10.1016/j.conbuildmat.2018.04.005.
[219] M. Pavelek, M. Prajer, K. Trgala, Static and dynamic thermal characterization of timber frame/wheat (Triticum Aestivum) chaffthermal insulation panel for sustainable building construction, Sustain. 10 (2018). doi:10.3390/su10072363.
[220] Z. Li, C.K. Chau, Influence of molar ratios on properties of magnesium oxychloride cement, Cem. Concr. Res. 37 (2007) 866–870. doi:10.1016/j.cemconres.2007.03.015.
[221] D. Deng, The mechanism for soluble phosphates to improve the water resistance of magnesium oxychloride cement, Cem. Concr. Res. 33 (2003) 1311–1317. doi:10.1016/S0008-8846(03)00043-7.

Dissemination activities concerning the PhD research

Publications

Virginia Barbieri, Magdalena Lassinantti Gualtieri, Cristina Siligardi - *"Wheat husk: a renewable resource for bio-based building materials"* under revision to Construction & Building Materials (14/02/2020).

Virginia Barbieri, Magdalena Lassinantti Gualtieri, Tiziano Manfredini, Cristina Siligardi - "*Hydration kinetics and microstructural development of a magnesium oxysulfate cement modified by macromolecules*" in press in Construction & Building Materials.

Virginia Barbieri, Magdalena Lassinantti Gualtieri, Tiziano Manfredini, Cristina Siligardi - "*Development of mechanical strength during time in magnesia light-weight concrete"* (in preparation).

Proceedings

PRO 131: ICBBM 2019 - 3rd International Conference on Bio-Based Building Materials (2019), e-ISBN: 978-2-35158-229-9; Eds. S. Amziane, M. Sonebi

- V. Barbieri, M. Lassinantti Gualtieri, C. Siligardi:
  "Recycling of raw wheat husk to manufacture magnesia cement based lightweight building materials"
- M. Lassinantti Gualtieri, V. Barbieri, C. Siligardi:
  "A lightweight magnesia-based cement by organic templating"

Congress participations

FEMS Junior EUROMAT 2018 Conference, July 08th - 12th 2018 - Budapest, Hungary
Oral Presentation of the following contribution:

- Barbieri Virginia, Cristina Siligardi, Tiziano Manfredini - *"Use of wheat hull (husk) as natural aggregate in lightweight insulating concrete"*

3rd International Conference on Bio-based Building Materials (ICBBM 2019, Belfast, UK), June 26th - 28th 2019
Oral Presentation of the following contributions:

- V. Barbieri, M. Lassinantti Gualtieri, C. Siligardi - *"Recycling of raw wheat husk to manufacture magnesia cement based lightweight building materials".*
- M. Lassinantti Gualtieri, V. Barbieri, C. Siligardi - *"A lightweight magnesia-based cement by organic templating"*

XII Convegno Nazionale INSTM e XV Convegno Nazionale AIMAT (Ischia, Italy), July 21st - 24th 2019
Poster:

- Malchiodi B, Barbieri V, Gualtieri M, Siligardi C, Manfredini T - *"Study of a porous magnesia-based cement"*

Visiting research scholar

In order to give added value to my PhD thesis, I spent 3 months (from April till July 2019) working on thermal and mechanical characterizations of agro-concretes at IUT Rennes (Département Génie Civil - Construction Durable) under the supervision of Professor F. Collet and Professor L. Christophe. This experience was an excellent mean to learn more about bio based building materials thanks to the skills, experiences and theoretical knowledge that this research group have in this field.